VLA OBSERVATIONS OF WIDE-ANGLE TAILED RADIO SOURCES

AILEEN A. O'DONOGHUE

National Radio Astronomy Observatory, and Physics Department and Astrophysics Research Center, New Mexico Institute of Mining and Technology

Frazer N. Owen²

National Radio Astronomy Observatory

AND

JEAN A. EILEK

Physics Department and Astrophysics Research Center, New Mexico Institute of Mining and Technology, and National Radio Astronomy Observatory Received 1989 April 10; accepted 1989 June 12

ABSTRACT

VLA observations of 11 wide-angle tailed radio sources are presented. The total intensity 20 cm image of each source is shown at the highest resolution which does not resolve out the extended structure. Images of radio contours overlaid on the CCD images of the parent galaxies are presented. The sources were also imaged at 6 cm. Spectral index information was obtained and is presented as a function of distance along the tails for each source. The magnetic fields, total energies, and pressures derived from a minimum pressure analysis are also presented as functions of distance along the tails. The polarization of the sources is discussed.

Subject headings: galaxies: structure — interferometry — polarization — radio sources: galaxies

I. INTRODUCTION

The class of wide-angle tailed radio sources (WATs) was first defined by Owen and Rudnick (1976). WATs are radio galaxies of intermediate radio luminosity ($10^{42} < L_{\rm radio} < 10^{43}$ ergs/s⁻¹ for a radio window from 10^7 to 10^{11} Hz) identified with central, dominant galaxies (often cD galaxies) in rich clusters of galaxies. The radio emission is characterized by oppositely directed jets suddenly decollimating into lobes that bend in the same direction, yielding roughly C- or L-shaped sources. No S-shaped sources of the size of the WATs have been observed for this paper. The decollimation is typically accompanied by a hot spot in each tail. Sizes of WATs vary from less than 100 kpc up to megaparsec scales. The outstanding characteristics of WATs are their overall shape, the sideto-side symmetry in the distance from the core at which the jets disrupt, and the dependence of the bending on the disruption. Most often the tails bend at the disruption. Some bend after the disruption. However, no major bends of sources without disruption of the jets are observed.

Interest in WATs first arose because of their intermediate character both in luminosity and morphology. The classical double sources such as Cygnus A (see Perley, Bridle, and Willis 1984) are more luminous, do not bend, and are generally found outside the rich cluster environment. The narrow angle tailed sources (NATs) such as NGC 1265 (see O'Dea and Owen 1986) are less luminous, with both tails bending

Various individual sources have been examined in the literature, including 3C 465 (Eilek et al. 1984; Leahy 1984), 1159 +583 (Burns, Owen, and Rudnick 1979), 1919+479 (Burns 1981; Robertson 1984), 1313+073 (Patnaik, Banhatti, and Subranhmanya 1984; Patnaik, Malkan, and Salter 1986), NGC 2329 (Feretti et al. 1985), 3C 75 (Owen et al. 1985), and 0043+201 and 0110+152 (Giovannini, Feretti, and Gregorini 1987). However, no investigation of WATs as a morphological and physical class has appeared since the initial defining

paper. In this paper, we present the observational results and

a summary of previous work on 11 WATs. The data are

presented in detail, and straightforward quantities ob-

ment with the National Science Foundation. Visiting Astronomer, NOAO, operated by the Association of Universities for Research in Astronomy, Inc., under contract with the National

¹Operated by Associated Universities, Inc., under cooperative agree-

Science Foundation.

back until they are parallel. They are associated with small galaxies in clusters thought to be moving through the intracluster medium (ICM) with velocities sufficient to bend the tails by the ram pressure of the impinging ICM (see O'Dea and Owen 1985). It was first thought that the WATs would be explained in the same manner as the NATs, with the less dramatic bends simply being the result of the slower velocities of the more massive galaxies close to the bottom of the cluster potential well (to which the ICM was assumed "fixed") (Owen and Rudnick 1976). However, studies have revealed that the expected velocities are too small to bend beams with the expected internal velocities. The flow velocities must be high enough either to transport the synchrotron-luminous material to the ends of the tails within the radiative lifetimes or to provide kinetic energy that can be converted to luminosity through reacceleration of relativistic particles (see Eilek et al. 1984; O'Donoghue 1989). Thus explaining the bends has become an interesting problem. Since the radio emission provides a probe of the inner cluster environment, understanding of the radio sources will motivate and lead to further understanding of clusters of galaxies.

76

tained by standard methods are listed. More detailed analyses of the physical consequences of the surface brightness evolution, spectral aging, and bending will be presented in a later paper (O'Donoghue, Eilek, and Owen 1990).

II. SELECTION OF THE SOURCES AND OBSERVATIONS

The sources were selected from a 1400 MHz survey of Abell clusters (Owen 1990), based upon a survey by Owen et al. (1982) with the NRAO 91 m telescope. With a sample of only 11 sources, statistically significant results could not be sought. These observations do, however, extend the data base of well-studied WATs, sampling the properties of WATs both as individual sources and as a class. Thus a variety of source morphologies, sizes, and luminosities were chosen within the rough constraints of being C-shaped (if they bend), close $(z \sim 0.1)$, bright (S \sim a few hundred mJy), and large in angular extent ($\geq 1'$).

The 20 cm images were obtained from data taken in the A-array (3 hr per source) and C-array (1 hr per source) at the standard VLA *L*-band frequencies. Data for the 6 cm images were obtained in the B-array (3 hr per source) and D-array (1 hr per source) at the standard VLA *C*-band frequencies. The observations were made from 1984 August to 1986 August.

The CCD frames were obtained from Owen and White (1990). They were taken at Kitt Peak and were reduced as described in Owen and Laing (1989).

III. THE DATA

Tables 1, 2, and 3 list the sources, along with the optical, radio, and bending data, respectively. Table 1 lists the source

TABLE 2 Radio Data

G	Flux Density at 1400 MHz		Monochromatic Luminosity
Source	(Jy)	Z	$(W Hz^{-1})$
0043+201 ^{a,b}	0.9	0.1063	1.1×10^{25}
$0110+152^{a,b}\dots$	1.0	0.0447	0.4×10^{25}
0836+290 ^{a,b}	0.8	0.0788	1.1×10^{25}
$0908-103^{a,b}$	0.6	0.129	2.1×10^{25}
1159+583 ^{a,b}	1.0	0.1018	2.2×10^{25}
$1231+674^{a,b}$	0.9	0.1062	2.1×10^{25}
$1306+107^{a,b}$	0.1	0.136	0.5×10^{25}
$1433+553^{a,b}$	0.5	0.1396	2.2×10^{25}
1636+379a,b	0.6	0.161	3.6×10^{25}
1826+747 ^{a,b}	0.6	0.121	1.9×10^{25}
2236-176 ^{a,b}	1.7	0.0698	1.7×10^{25}
1919+479 ^{c,d}	0.9	0.104	2.1×10^{25}
3C 465 ^{a,e}	7.7	0.031	1.5×10^{25}
3C 338 ^{a,e}	3.5	0.031	0.7×10^{25}
3C 75 ^{a,b}	5.6	0.027	0.8×10^{25}
1313+073 ^f	2.0	0.0507	1.0×10^{25}

^aFlux density from et al.

positions, redshifts, cluster properties, magnitudes, and offset from cluster center of the parent galaxies. The redshifts and magnitudes were obtained from Owen and White (1990), with

TABLE 1
OPTICAL PROPERTIES

	ABELL	SKY COORDINATES			ABSOLUTE	CLASS		DISTANCE TO
Source	CLUSTER	R.A.	decl.	z	Magnitude	OR	BM	Center ^a
0043+201	98	00 ^h 43 ^m 50 ^s 71	+ 20°11¹41″9	0.1063	- 23.53		II–III ^b	0.08 ^c
0110+152	160	01 10 20.43	+ 15 13 34. 7	0.0447	đ		III^e	0.09^{c}
0836+290	690	08 36 13.55	+ 29 01 14. 8	0.0788	-23.78		$\mathbf{I^f}$	0.02^{c}
0908-103	761	09 08 32.56	- 10 21 35. 1	0.129	-23.75^{g}		d	g
1159+583	1446	11 59 30.41	+ 58 1851.3	0.1018	-23.40	$1^{\rm h}$	$\mathbf{I}^{ ext{i}}$	0.07^{c}
							$II-III^{j}$	
1231+674	1559	12 31 03.88	+ 67 2417.2	0.1062	-24.02	$1^{\rm h}$	$\mathbf{I^i}$	0.07^{c}
1306+107	1648	13 06 34.48	+ 10 45 52. 2	0.136	-24.11^{g}		$\mathbf{H}^{\mathbf{i}}$	0.30^{c}
1433+553	1940	14 33 59.92	+ 55 20 54. 6	0.1396	-23.79	$1^{\rm h}$	$\mathbf{H}^{\mathbf{b},\mathrm{i}}$	0.07 ^h
1636+379	2214	16 36 15.68	+ 37 58 54. 3	0.161	-23.53	$1^{\rm h}$	II^k	0.27^{c}
1826+747	2306	18 26 23.27	+ 74 42 05. 4	0.121	-23.15^{g}	2^{h}	II^k	0.06^{h}
2236-176	2462	22 36 30.14	- 17 36 06. 2	0.0698	-23.54		$\mathbf{H}^{\mathbf{j}}$	0.11^{c}

^aRatio of the galaxy's distance from the center to the corrected Abell radius.

^bRedshift from Owen, White, and Thronson 1988.

^cFlux density from Burns 1981.

d Redshift from Burns, Gregory, and Holman 1981.

^eRedshift from Owen and Rudnick 1976.

^fFlux density and redshift from Patnaik, Malkan, and Salter 1986.

^bBautz 1972.

Owen 1975b.

^d Not available.

Bautz and Morgan 1970.

Roland et al. 1975.

^gBased upon an estimated redshift.

hRudnick and Owen 1977.

McHardy 1974.

Leir and van den Bergh 1977.

^kSimon 1978.

TABLE 3
BENDING DATA

	DISTANCE OF	Bending Angle				
Source	BEND FROM CORE (kpc)	Bend of Each Tail from Initial Jet Direction	for Entire Source			
0110+152N	140	55°	160°a			
0836+290N	133	35	110 ^b			
0836+290S	103	80				
0908-103	c	50	100			
1159+583N	14	35	130^{b}			
1159+583S	25	30				
1231+674N	18	40	155 ^b			
1231+674S	22	15				
1306+107N jet	21	55	120 ^b			
1306+107N tail	161	85				
1306+107S	148	60				
1433+553N	55	70	160 ^b			
1433+553S	36	115				
1636+379N	43	20	135 ^b			
1636+379S	16	120				
1826+747W	29	50	75 ^d			
1826+747E	38	90	•			
2236-176E jet	14	30	110 ^b			
2236-176E tail	35	90				

 $^{^{}a}\chi$ for the bend at the end of the northern tail. However, since this source has no bend at the hot spots, χ may be defined as 180°.

the magnitudes determined as those in Owen and Laing (1989). The offsets are given in terms of the Abell radius of the cluster. This is defined as

$$A_c = \frac{103q_0^2(1+z)^2}{q_0z + \left[(1+2q_0z)^{1/2} - 1 \right] (q_0-1)} \operatorname{arcsec}$$

(see Rudnick and Owen 1977), where q_0 is the deceleration parameter, usually taken as 0.1. Table 2 gives the radio flux

densities and monochromatic luminosities. Table 3 describes the major bends in each source. Table 4 summarizes cluster data, integrated radio luminosities, size scales, and distances for each source. Figure 1 shows contour images of the sources scaled to the same linear size ($H_0 = 75 \text{ km s}^{-1} \text{ Mpc}^{-1} \text{ was}$ assumed). These tables and figures give a sense of how the WATs hold together as a class. The sources are generally in clusters containing a dominant central galaxy, either a cD galaxy or a galaxy intermediate between a giant elliptical and a giant cD (Bautz-Morgan class I or II clusters; see Bautz and Morgan 1970). The sources are all within 30% of the corrected Abell radius (see Rudnick and Owen 1977) of the center of the cluster. Their monochromatic radio luminosities cover a very narrow range (within a factor of 3 of 10^{25} W Hz⁻¹ at 1400 MHz). The sources are bent in "C" shapes, rather than "S" shapes, and only one source has a bending angle less than 100°, as listed in Table 3.

The sources are presented individually, as follows. For each source, the 20 cm total intensity image is shown at the highest resolution which does not resolve away the source. Lower resolution images are shown where useful to bring out low surface brightness structure. The 20 cm radio contours are shown overlaid on the CCD images of the parent galaxies. Intensity images of 6 cm total and polarized emission were also obtained for each source; the 6 cm image adds little information about the source morphology and is shown in only one case.

The first contour plot for each source shows the polarization. The contours are the total intensity contours at 20 cm. The polarization vectors are scaled to the fractional polarization at 6 cm and show the direction of the position angle of the electric field vector at 6 cm. No correction for Faraday rotation has been made. The data at 6 cm are used because the sources are depolarized at the lower frequency. The second contour plot for each source shows the positions of the centers and the numbers of the cross-tail slices from which data were obtained to derive spectral index and minimum-pressure information.

TABLE 4
Source Summary

						Ex	TENT
Source	ALTERNATE Names	ABELL CLUSTER	RICHNESS	$L_{\text{source}} $ $(10^{42} \text{ergs s}^{-1})$	DISTANCE ^a (Mpc)	Ang.	Lin. (kpc)
0043+201	4C 20.04	98	3	2.6	446	2'45"	290
0110+152		160	0	0.54	182	8 50	430
	4C 29.30 B20836+29 OJ 261	690	1	1.4	326	6 12	510
0908-103	03 201	761	1	2.7	546	4 20	540
1159+583	4C 58.23	1446	2	2.8	426	1 40	170
1231+674	4C 67.21	1559	2	1.7	445	3 20	350
1306+107	4C 10.35	1648	1	0.59	577	3 30	460
1433+553	4C 55.29	1940	3	2.7	594	1 50	240
1636+379	4C 37.48 B21636+37	2214	1	3.4	691	3 00	450
1826+747		2306	0	2.4	510	3 45	440
2236-176	PKS 2236-17	2462	0	2.2	288	2 42	200

 $^{^{}a}H_{0} = 75 \text{ km s}^{-1} \text{ Mpc}.$

^bValentijn 1979*a*, *b*.

^cThe tails in this source bend gradually, not at a particular point; thus,

a distance for the bend cannot be defined.

d Smallest χ that can be defined, since here has been taken as the angle between the tails before they flatten out and extend to the east and west.

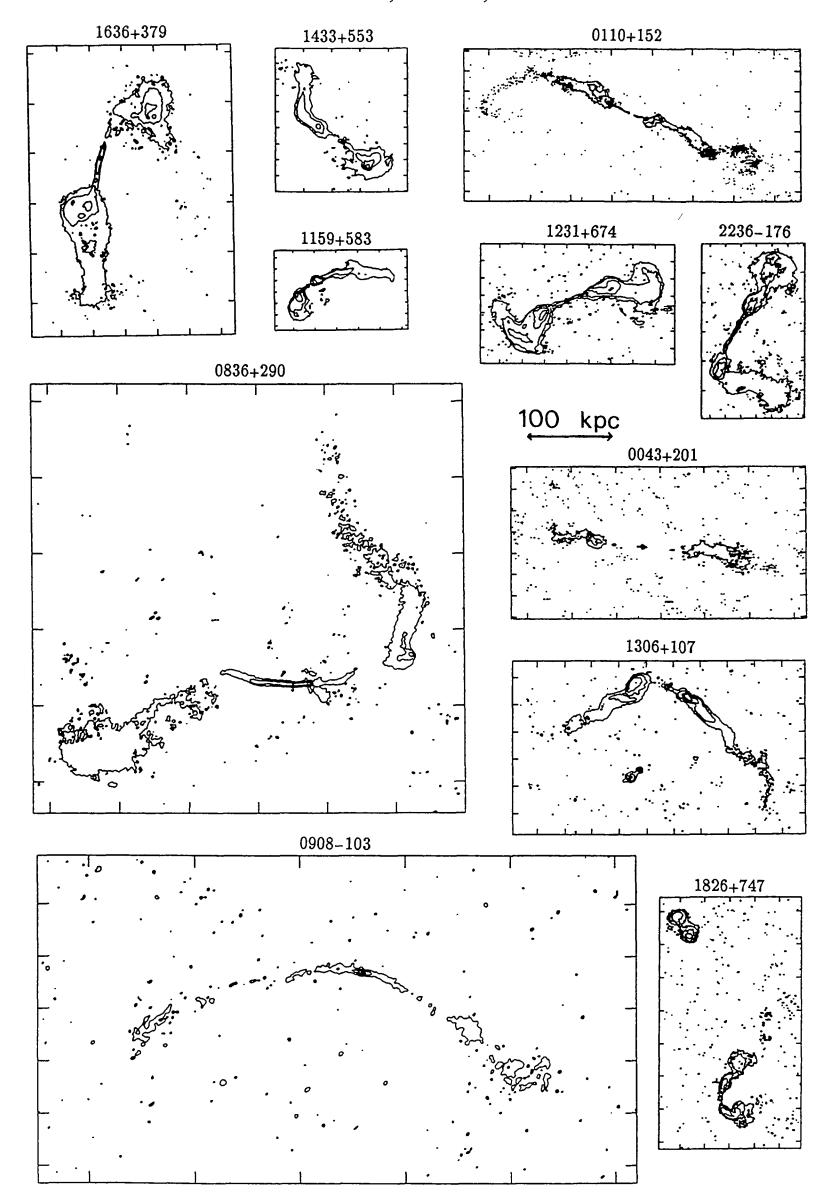


FIG. 1.—All the sources described in this paper are shown to the same linear scale

IV. INDIVIDUAL SOURCES AND THE ANALYSIS

The conditions in the sources were estimated using a minimum pressure analysis. To evaluate the minimum pressure quantities, the luminosity and the emitting volume must be known. Slices taken across the tails on the 20 cm, total intensity images were used to find the luminosities and volumes of cylindrical cross sections of the tails at regular distances from the core. The slices were taken on the highest resolution images at which tail features were not resolved so that the flux density distribution was smooth. Two-dimensional Gaussian functions were then fitted to each slice to

obtain the peak flux density (actually flux density per area in millijanskys per beam) and the Gaussian half-width. The 6 cm peak flux densities and the mean spectral indices were taken directly from the slice plots.

The luminosity of each slice was found by the following method. The slices provided the flux density per beam at each pixel across the tail. The flux density of the entire slice is the flux density per area integrated over the slice. The integral under a Gaussian is 1.133 times the product of the peak and the full width at half-maximum. Therefore, the flux density per unit length was found by multiplication of the peak flux density per beam (converted to flux density per arcsecond) by

the diameter of the tail. The total flux density per slice is this value multiplied by the beam width. The luminosity was found from the flux density by assuming the radio window to extend from 10^7 to 10^{11} Hz.

Determination of the emitting volumes was more complex. After deconvolution of the beam, the widths of the resolved tails were found from the slice half-widths by assuming cylindrical tails sampled by Gaussian beams. The radius of the tail in this case is the second moment of the cylinder scaled by the Gaussian as described by Burns et al. (1979). The length of the slice along the tail is the beam width; thus, the volume of the tail sampled by the slice is

$$V_{\text{slice}} = \pi \left[\left(\frac{1}{2} \right) 0.894 (\text{FWHM}_{\text{slice}}) \right]^2 (\text{FWHM}_{\text{beam}}). \quad (1)$$

The minimum pressure magnetic fields, energies, and pressures for each tail were found using

$$P = \left(\frac{7}{12}\right) \left(\frac{1}{2\pi}\right)^{3/7} \left(\frac{2c_{12}L}{V}\right)^{4/7},\tag{2}$$

$$E = \left(\frac{5}{4}\right) \left(\frac{V}{2\pi}\right)^{3/7} (2c_{12}L)^{4/7},\tag{3}$$

and

$$B = \left(\frac{4\pi c_{12}L}{V}\right)^{2/7} \tag{4}$$

(see O'Donoghue 1989), where L is the luminosity of the slice, V is the volume of the slice found from the analysis above, and c_{12} is determined by the spectral index of the source (taken as the initial spectral index for each source) and the limits of the radio window. Values of c_{12} are tabulated by Pacholczyk (1970).

The spectral index³ and minimum pressure values obtained from the cross-tail slices are shown as functions of distance along the tails. The errors in the spectral index were determined from

$$\Delta \alpha = \left[\left(\frac{\ln \left(S_6 / S_{20} \right)}{\ln \left(\nu_6 / \nu_{20} \right)} \right) \right] \sqrt{\varepsilon_6^2 + \varepsilon_{20}^2},$$

where the fractional error at each wavelength, ε_i , is determined from the image noise at that frequency, n_i , the flux density at that frequency, S_i , and the instrumental calibration error, ε_c (taken as 3% of the flux density for the VLA), according to

$$\varepsilon_i = \frac{\sqrt{\varepsilon_c^2 + n_i^2}}{S_i}.$$

Thus the errors are greater in the low flux density regions of

the sources. In the discussion of each source, the actual values of α obtained from Astronomical Image Processing System (AIPS) are stated without quoting the limits of error. They should be interpreted accordingly. In particular, values of $\alpha > -0.5$ in the tails are probably unrealistic. Systematic errors due to missing spacings may also appear, particularly in the large, poorly sampled sources such as 0836+290. The bias toward steepening or flattening the spectral index is unknown since the combination of arrays (A- and C-arrays at 20 cm and B- and D-arrays at 6 cm) eliminated the coverage differences between the frequencies. The data from the slices are given in tables for each source. In each of these tables, the slice numbers (referring to the appropriate contour plot) are given in the first column; the distances of the slices from the core along the tail are given in the second column. In the third column, the diameter of the tail is listed. For unresolved parts of tails, the diameter was arbitrarily taken as half the beam width. The peak flux density per beam is listed in the fourth column. The volume of each slice is listed in the fifth column. The remaining four columns list the luminosity and minimum pressure quantities.

a) 0043+201

The straightest source in the survey is 0043+201 (shown in Figs. 2 and 3 [Pls. 46 and 47]). It has no dramatic bend at any resolution, although it does have jets that disrupt and decollimate into tails. At high resolution the jets seem slightly misaligned with the tails; thus, bending may occur in the projected dimension. The jets are the longest in the survey, as well as the straightest, with the northern jet spanning almost 30" and the southern spanning 40". These make up a sizable portion of the source's 4'20" expanse (at 12" resolution at 20 cm). This source was selected to include the extremum of straightness in the WAT class since it qualifies as a WAT in every way other than the typical bend.

This source and the cluster A98 have been studied more than any others in the survey. Abell 98 is classified as a Bautz-Morgan type II–III, lacking a single dominant cD galaxy, by Bautz (1972). The velocity dispersion has been investigated by Faber and Dressler (1977), who determine $\sigma_o = 793 \, (+159, -198) \, \mathrm{km \ s^{-1}}$, Yahil and Vidal (1977), who find $\sigma_o = 887 \, \mathrm{km \ s^{-1}}$ after removing the suspected field galaxies, and Danese, De Zotti, and diTullio (1980), who find $\sigma_o = 1383 \, (+491, -302) \, \mathrm{km \ s^{-1}}$. The disagreement between these values is due to differing galaxy velocity samples and methods of analysis.

In concurrent papers, Forman et al. (1981) and Henry et al. (1981) investigate the bimodal X-ray distributions of the cluster. Forman et al. (1981) conclude from statistical studies that the bimodal distributions are physical associations of subclusters, not simply projections. They claim that these represent an intermediate stage in cluster formation which will end in the merger of the subclusters and relaxation into a Coma-type cluster. They also point out that, although the clusters lack single dominant galaxies (they are not BM type I clusters), the subclusters each have dominant galaxies near their centers, indicating galactic cannibalism or a similar process forming the central galaxies. Citing optical work by

³The spectral index is denoted by α where the flux density, S, obeys $S \propto v^{\alpha}$.

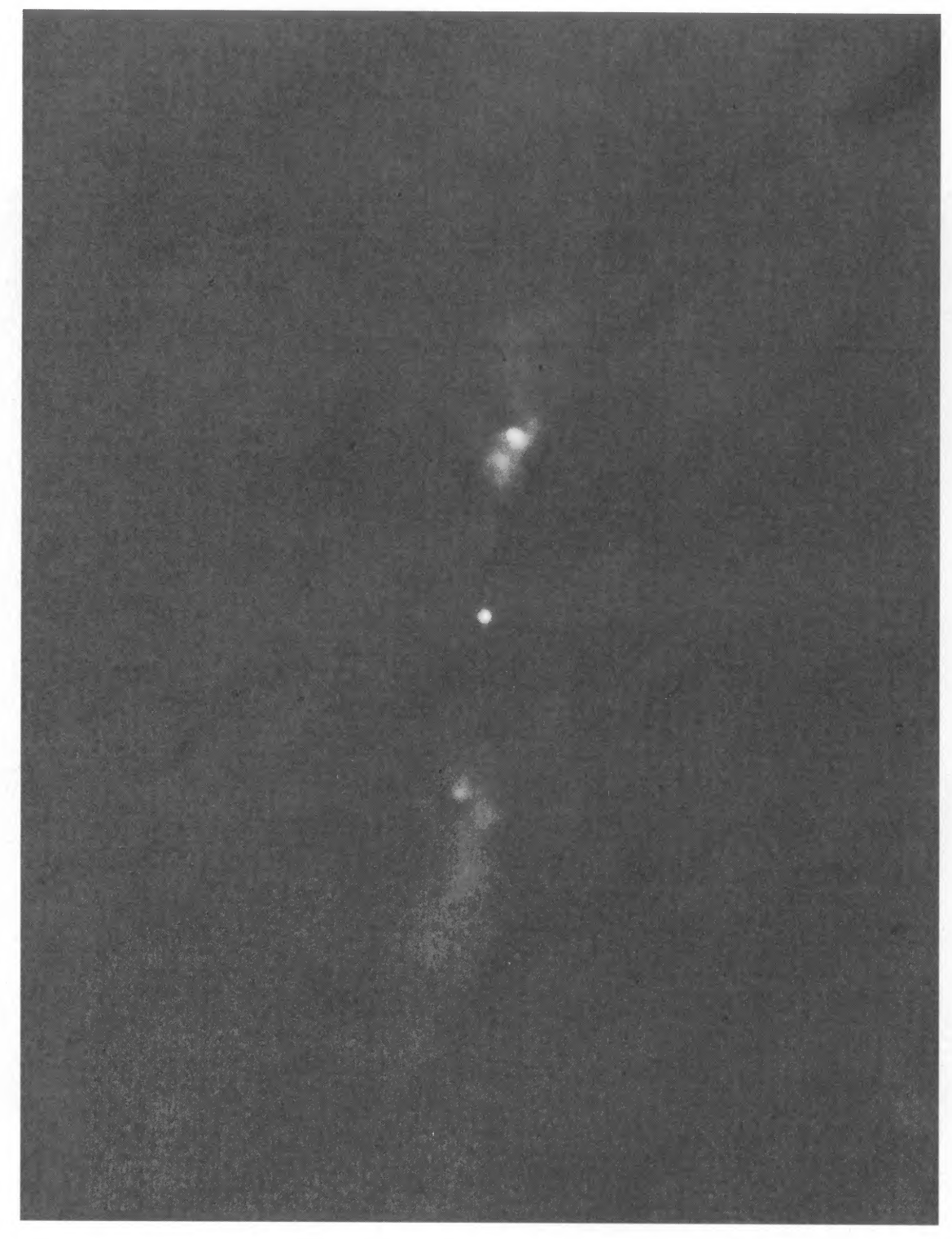


Fig. 2.—High-resolution (1") image of 0043+201 at 20 cm

O'Donoghue, Owen, and Eilek (see 72, 79)

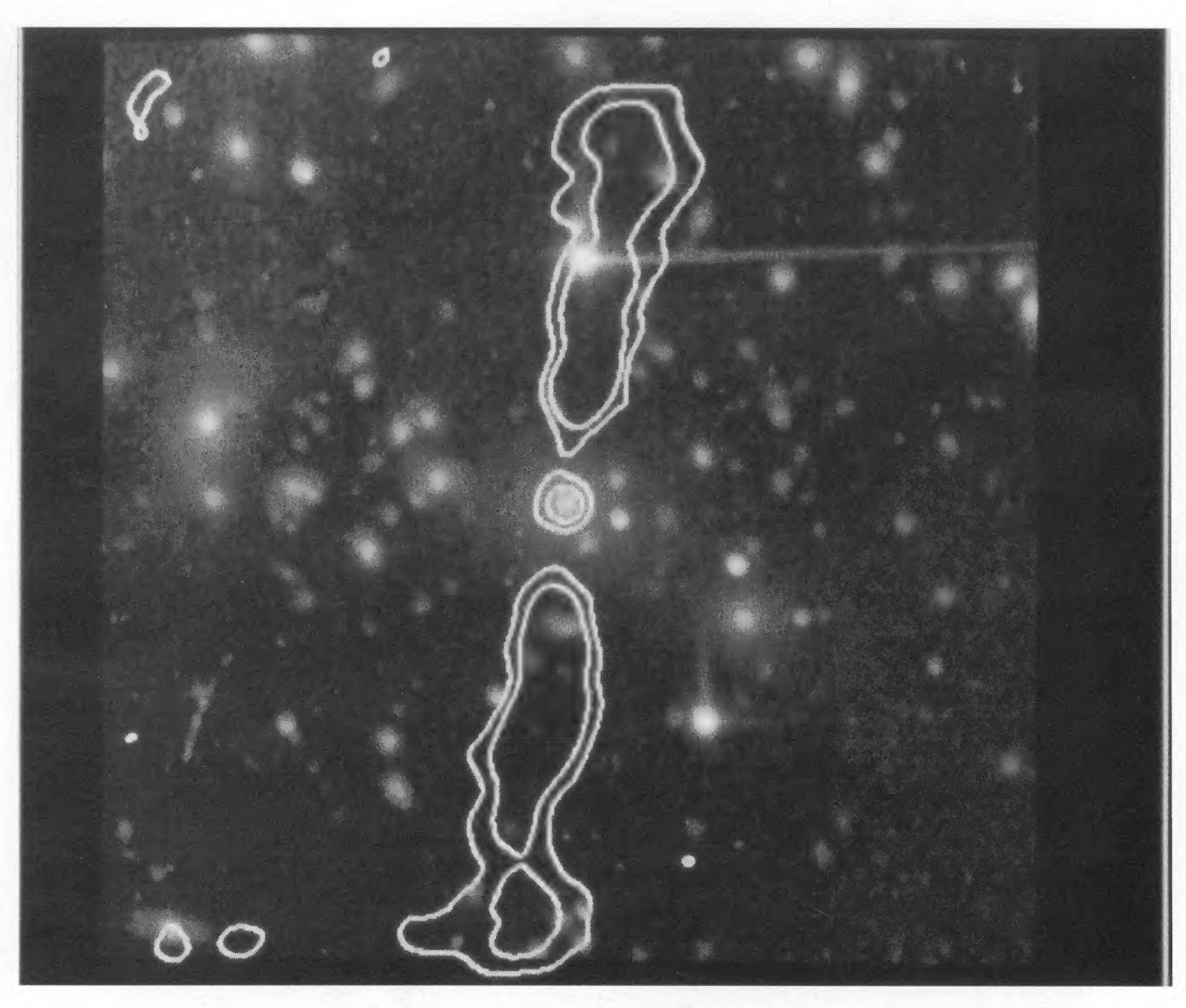


Fig. 3.—20 cm contours of 0043+201 overlaid on the optical galaxy image

O'DONOGHUE, OWEN, AND EILEK (see 72, 79)

Dressler (1976) and Faber and Dressler (1977), Henry et al. (1981) identify the southern subcluster (A98 south) with the cluster center of Abell 98 and the radio source. From Dressler's (1976) optical data, they obtain core radii of 0.54(+0.72,-0.33) and 0.48 ± 0.18 Mpc for the northern and southern subclusters, respectively. They also determine velocity dispersions of 983(+309, -280) km s⁻¹ and 634(+253, -222)km s⁻¹ for A98 N and A98 S by the methods of Danese, De Zotti, and diTullio (1980). Using data from the IPC of the Einstein X-Ray Observatory, they fit the surface brightness produced by thermal bremsstrahlung radiation from a selfgravitating isothermal sphere to determine the X-ray core radii of A98 N and A98 S as 1.03(+0.18, -0.33) Mpc and 0.78(+0.16, -0.09) Mpc. The northern component is not well fitted by this model, but requires an unresolved source at the origin, indicating a massive galaxy. Central number densities of $59 \pm 14 \times 10^{-4}$ cm⁻³ and $8.4 \pm 1.2 \times 10^{-4}$ cm⁻³ are obtained from the core radii and central surface brightnesses. The masses they obtain from these figures indicate that the two subclusters are bound and will merge in $\sim 10^9$ yr.

Beers, Geller, and Huchra (1982) further investigate subclustering with an enlarged redshift data set and model the cluster as a two-body system. They determine that the system is bound, with the two subclusters separated by ~ 3.6 Mpc, moving with a relative velocity of ~ 550 km s⁻¹ and will merge in 3×10^9 yr. These results are consistent with the results of Henry *et al.* (1981).

Radio data have also been presented by many investigators, including Slingo (1974) (408 MHz), McHardy (1974) (750 and 5000 MHz), Owen (1975b) (2695 MHz), who identifies the two radio sources identified with the two subclusters, Riley (1975), (178 MHz), Owen, Rudnick, and Peterson (1977), (2695 MHz), who first classify the source as a WAT, Fomalont and Bridle (1978) (2700 MHz), Valentijn (1979a, b), and Fanti et al. (1983a, b), (1400 MHz). This source, along with 0110+152, was included in a study of first-ranked galaxies in Abell clusters by Giovannini, Feretti, and Gregorini (1987). They present 20 cm images and superpositions of the radio contours on CCD images of the parent galaxies. In their analysis of 0043 + 201, they discuss the X-ray and optical double structures as well as the double-lobe structure of the radio source associated with Abell 98 S (0043+201). They give the relative velocity between the galaxy and the cluster as 604 km s^{-1} , point out that the X-ray studies cited above indicate that the cluster is dynamically young, and argue that these facts are incongruous with a radio structure that is not bent and a cluster X-ray centroid that is not displaced from the galactic nucleus. Thus they argue for both galaxy-X-ray centroid displacement and bending of the radio source parallel to the line of sight.

i) Source Structure

A feature of this source not apparent in the high-resolution images shown is a flaring, or flattening of the tails against some invisible interface, at the ends (about four to five jet lengths from the core). This was noted in the low-resolution snapshot images of the source by which it was selected for the WAT survey from Owen's (unpublished) survey of clusters, and was one of the reasons for its selection. Such "flattening"

of tails is not uncommon in WATs (four other sources in this survey exhibit similar behavior).

ii) Polarization

At 20 cm, there is very little polarized flux density at full resolution. The hot spots, in fact, are the only features obviously above the noise in either tail. The northern hot spot is much more pronounced than the southern. In the fractional polarization, the hot spots also stand out, although less dramatically. The northern hot spot is ~ 40% polarized, whereas the southern is between 20% and 30% polarized. The small arc just west of the primary hot spot in the northern tail is 30% to 40% polarized, and the rest of the main lobe has fractional polarizations of 20% to 30%. The southern lobe lacks features and is less smooth, but tends to polarizations ranging from 20% to 50%, increasing toward the end of the tail.

At 6 cm, the source is similar in its polarized features; however, it differs in the relative values of the fractional polarization. The 6 cm polarization is shown in Figure 4. The

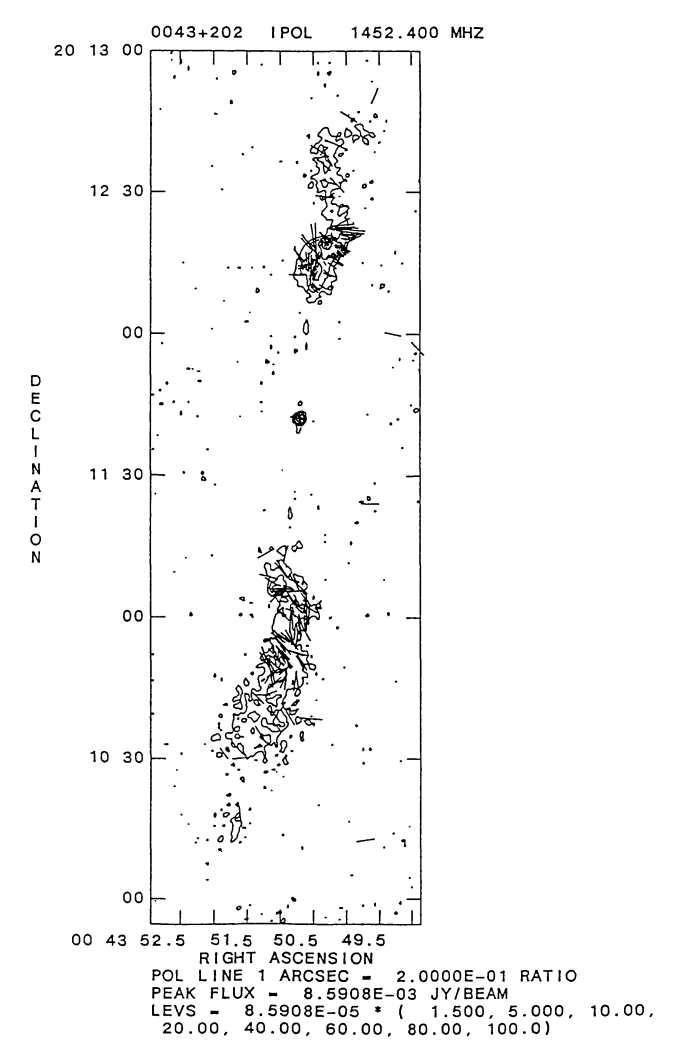


FIG. 4.—Polarization angles (electric vectors) for 0043+201, uncorrected for Faraday rotation. Contours are those of the full resolution 20 cm image, and lengths of the vectors are proportional to the fractional polarization at 6 cm.

northern hot spot is less polarized than the rest of the lobe; 10% to 20% compared to 20% to 30%, respectively. The southern tail has too few pixels above the 3 σ blanking to discuss anything beyond a general trend of increasing fractional polarization toward the end of the tail.

iii) Spectral Index and Minimum Pressure Analysis

At full resolution the spectral index is rather confused, indicating the low surface brightness of the source at 6 cm. No spectral index for the jets can be established since they do not appear on the 6 cm image; however, taking 3 times the rms noise (0.031 mJy per beam) as a limit and the mean jet flux density at 20 cm as 0.157 mJy per beam (about 3 σ), they must have a spectral index steeper than -0.4.

Spectral data were obtained between 6 and 20 cm for the slices indicated in Figure 5; the results are shown in Figure 6. A general steepening along the tails is apparent. Near the core, the spectral index is about -0.5, and it gradually decreases to about -2.0 at both ends. Spurious points of very

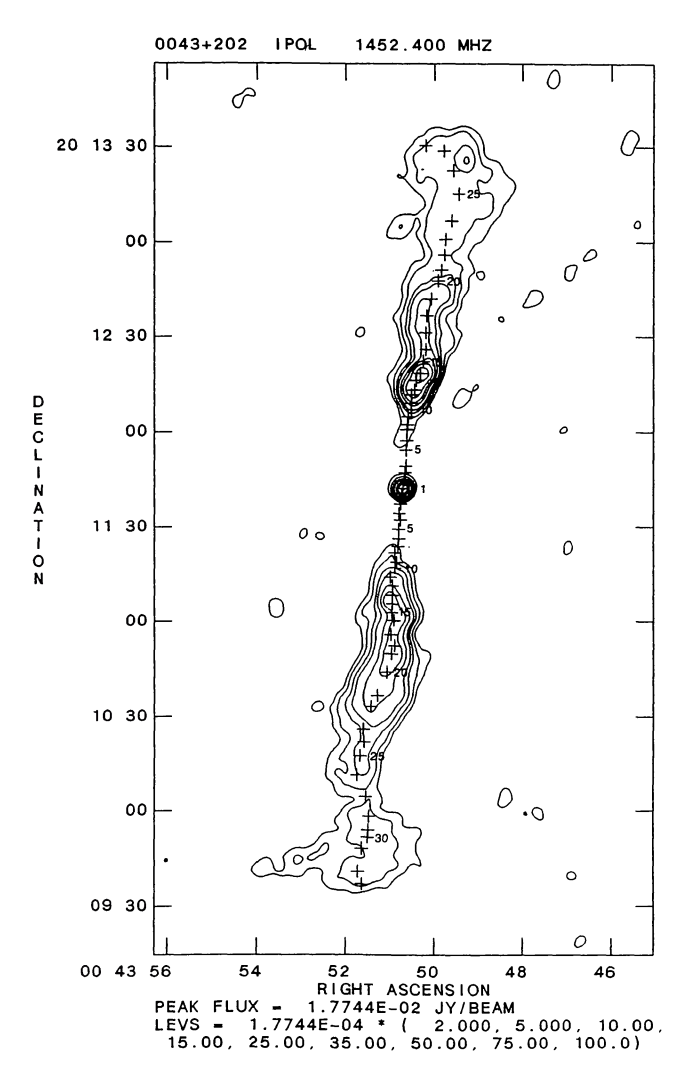


FIG. 5.—Positions of the centers of slices taken perpendicular to the jets and tails of 0043+201, on a low-resolution contour plot. Spectral indices and minimum pressure values for these slices are shown in Figs. 6 and 7.

flat spectral index appear on the edges, but this is due to the low brightness (the total intensity images were blanked at 3 σ before making the spectral index image; thus at the edges, the flux density is just greater than this). No particular features in the spectral index appear in either tail.

The results of a minimum pressure analysis on 0043+201 are shown in Figure 7 and in Tables 5 and 6.

b) 0110+152

Of the sources surveyed, 0110+152 is the largest in angular size, spanning over 10 minutes of arc at low resolution, or 429 kpc at its redshift of 0.0447. It is also the lowest luminosity source. At low resolution (11"), the source is mostly straight, with only a smooth bend at the end of the northern tail and a hook at the end of the southern tail to qualify it as a bent source. (This can be seen in Giovannini, Feretti, and Gregorini 1987). High-resolution images are shown in Figures 8 and 9 (Plates 48 and 49). In these images, the jets are approximately equal in surface brightness (~0.3 mJy arcsec⁻²) and appear quite straight with no gaps. The detail within the tails is quite striking. The jets in this source are shown in detail in Figure 9. They appear to enter the lobes without disruption, although the dynamics become more pronounced once they are in the lobes.

The cluster Abell 160 is classified as a Bautz-Morgan type III by Bautz and Morgan (1970). Optical work on this source includes identification of four nuclei in the parent galaxy by Hoessel and Schneider (1985). Tonry (1985) presents the light profiles, redshifts, and stellar velocity dispersions for all the nuclei and gives the relative velocities between the minor nuclei and the central nucleus as -104, -298, and +577km s^{-1} . He also gives the projected separations from the central nucleus as 4.7, 7.1, and 7.2 kpc ($H_0 = 100$ km s⁻¹ Mpc) for the same respective nuclei. Because of the rather low relative velocities, he claims that there may be interaction between the nuclei and the central nucleus. Radio investigations include Owen (1975b) (2695 MHz) and Fanti et al. (1983a) (1400 MHz). The most extensive investigation has been by Giovannini, Feretti, and Gregorini (1987), who present 1400 and 4900 MHz data from WSRT and the VLA, with radio contours and superposition of the (1400 MHz) contours on the CCD image of the parent galaxy. They claim that the structure of the source is probably due to the interaction of the various nuclei.

i) Polarization

The polarization vectors at 6 cm are shown in Figure 10. In the fractional polarization, the first curve that the jet makes within the northern lobe is brighter than the surrounding lobe, having polarized emission of 20% to 40%, contrasting with 10% to 20% in the surrounding lobe. Overall, the fraction of polarized emission increases toward the ends of the tails. In the southern tail, the most remarkable feature is a sudden brightening in the fractional polarization. The fraction of polarized emission in this feature is 30% to 60%, whereas it is 20% to 30% in the surrounding lobe.

The polarization angles uncorrected for Faraday rotation are generally perpendicular to the tails. If there is no or little Faraday rotation, these results confirm the results of Giovan-

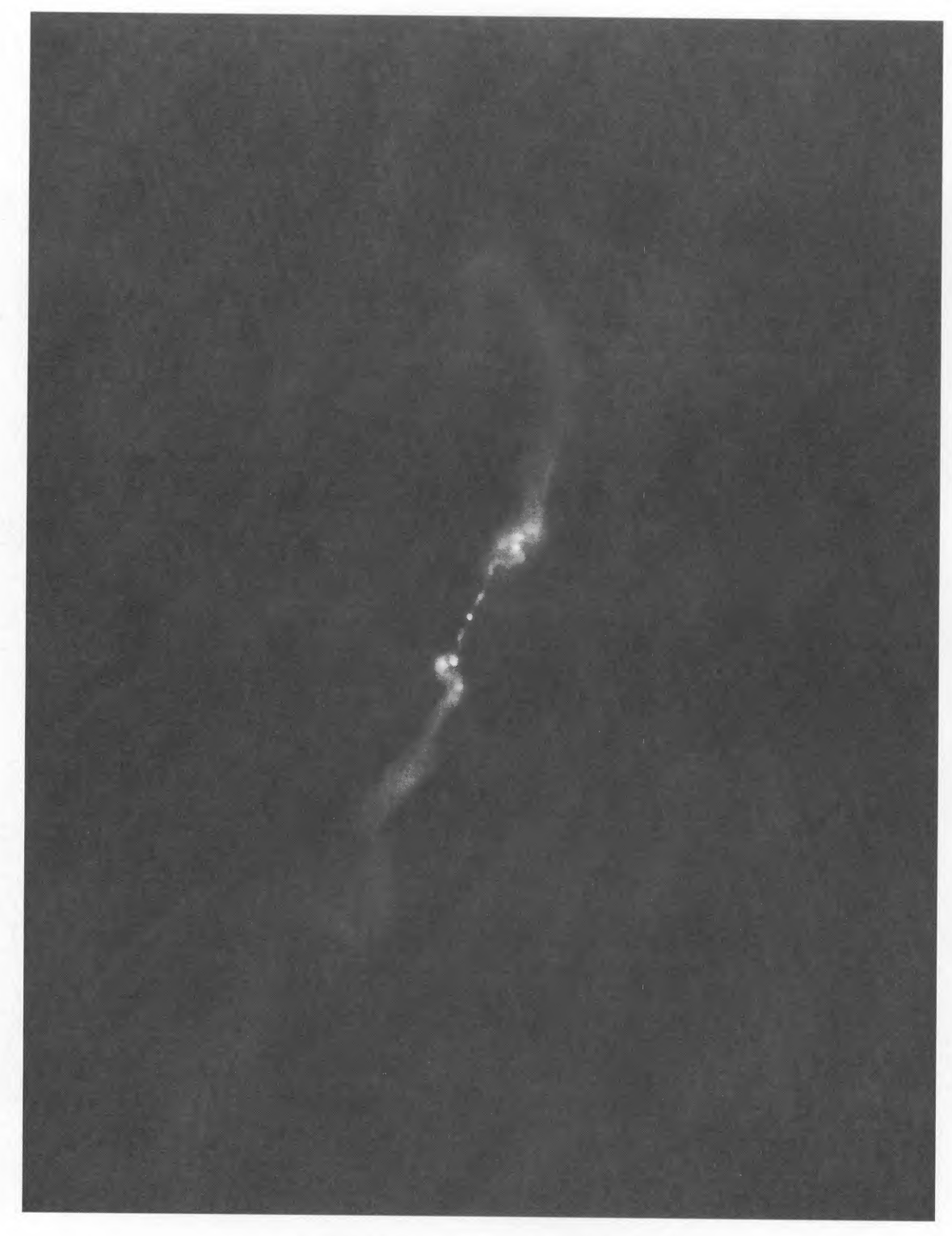


Fig. 8.—High-resolution (1") image of 0110+152 at 20 cm

O'Donoghue, Owen, and Eilek (see 72, 81)

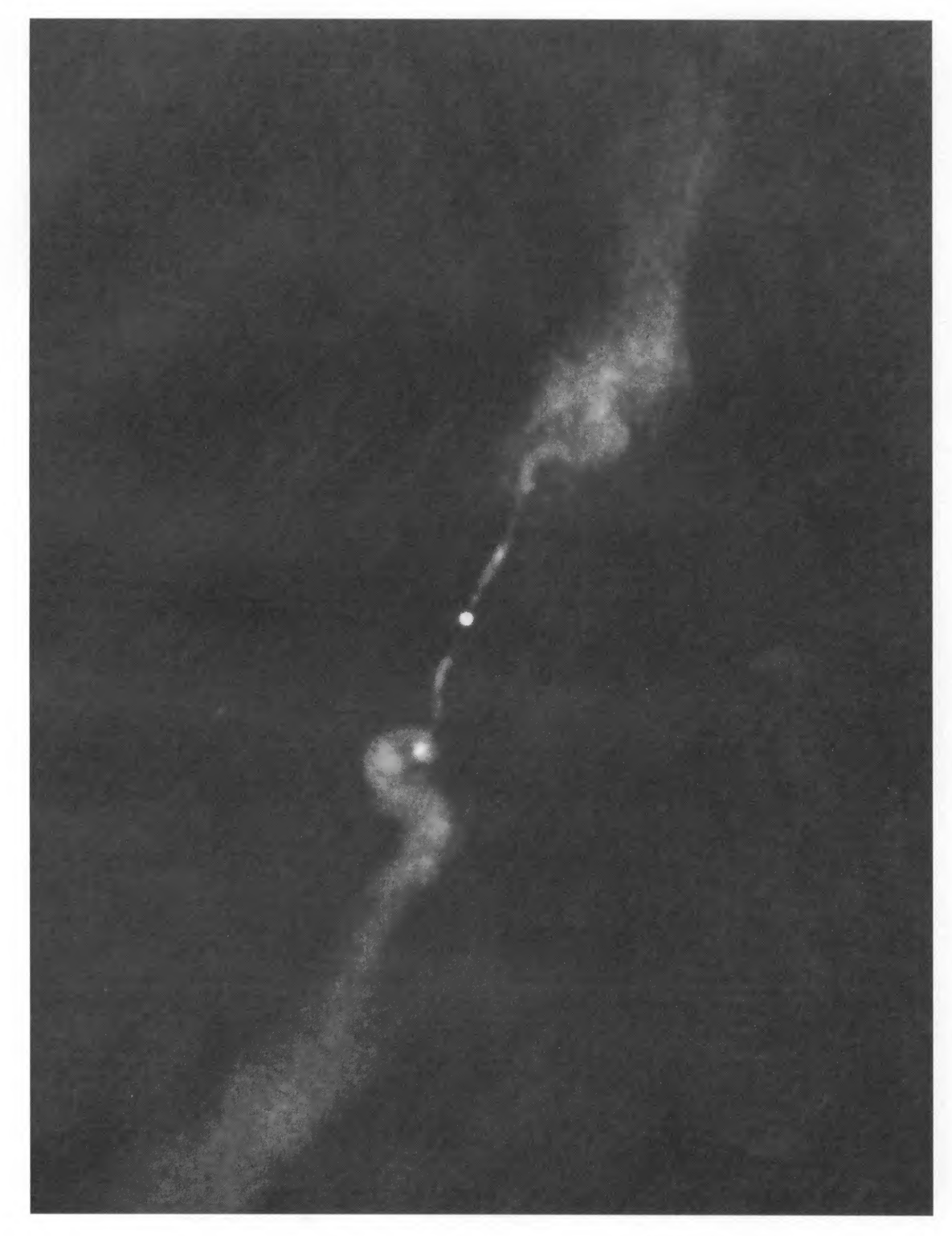
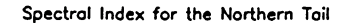
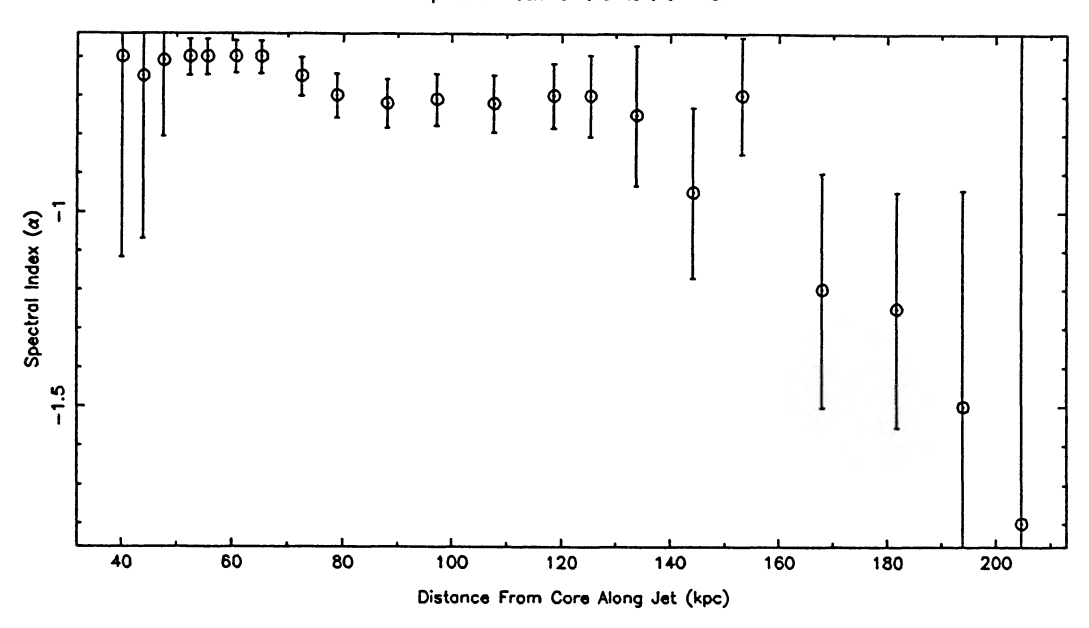


Fig. 9.—High-resolution (1") image of the jets and inner tails of 0110+152 at 20 cm O'Donoghue, Owen, and Eilek (see 72, 81)





Spectral Index for the Southern Tail

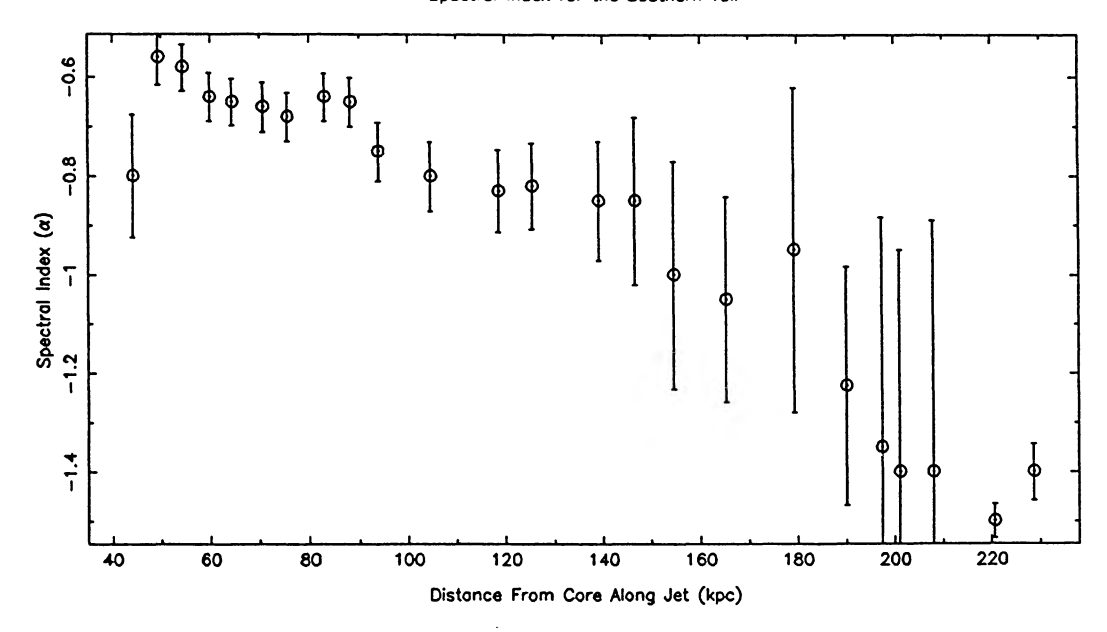


FIG. 6.—Spectral index values between 6 and 20 cm for 0043+201. Values were determined using estimated mean values from slices taken across the total intensity maps, at positions shown in Fig. 5.

nini, Feretti, and Gregorini (1987), who find the electric vectors at 4900 MHz to be everywhere perpendicular to the tails, indicating a magnetic field aligned with the tails.

ii) Spectral Index and Minimum Pressure Analysis

The spectral index was determined from the 6 and 20 cm images at the slices shown in Figure 11; the results are shown in Figure 12. In addition to the general steepening, some

particular features were apparent from inspection of the spectral index images. The wave structures of the northern tail appear as trails of quite flat $(-0.4 \le \alpha \le -0.2)$ spectral index. In the southern tail, two such trails appear to separate and join again in the region of the swing to the west. More generally, the spectral indices measured in the jets increase from about -0.5 to -0.8 and steepen slightly (down to about -0.9) in the lobes. In the tapered image, the core has $\alpha \approx -0.3$, the jets show α steepening from -0.4 (S) or -0.6 (N)

1990ApJS...72...750

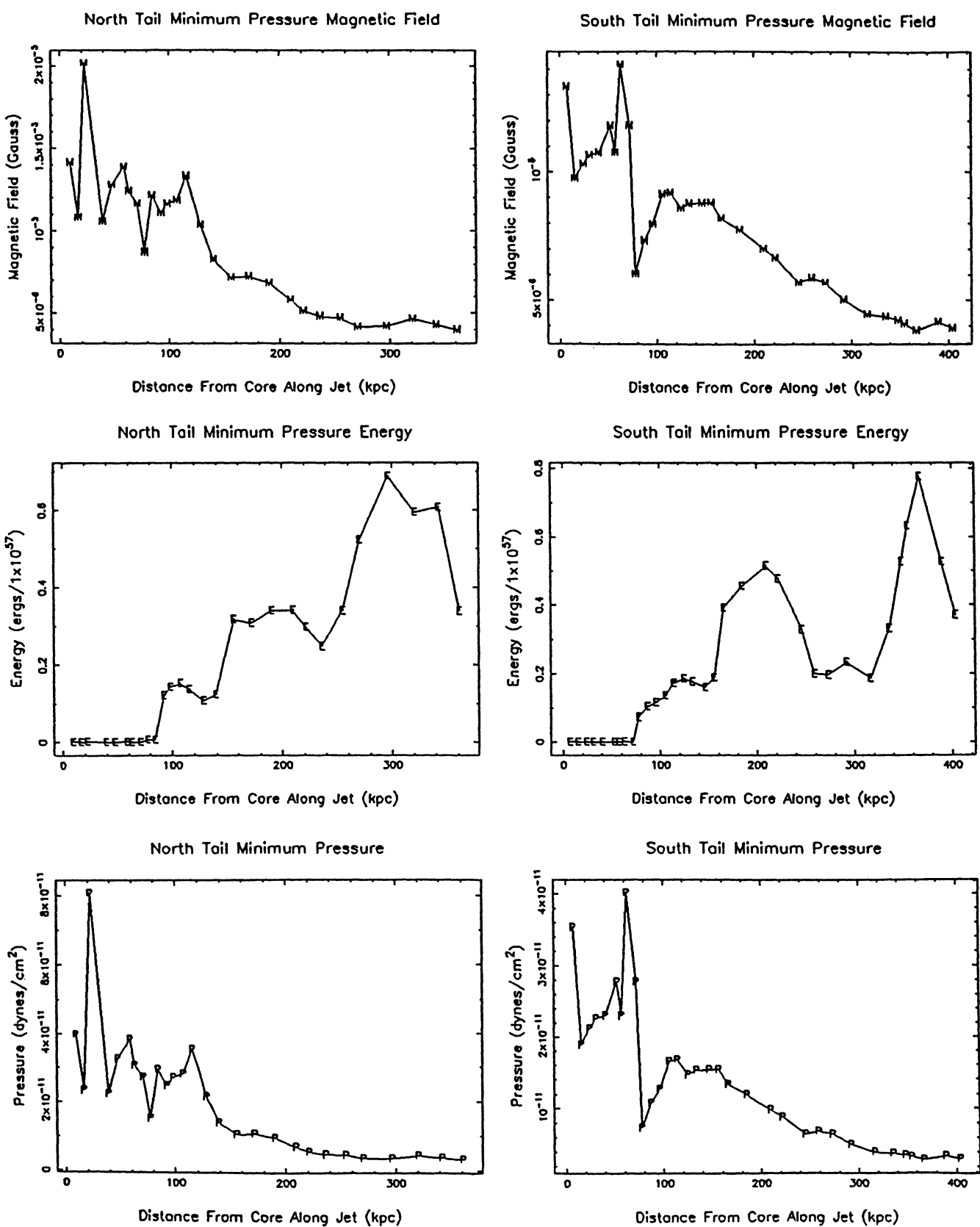


FIG. 7.—Estimates of the magnetic field, total energy (within one slice across the tail), and pressure, derived from minimum pressure arguments, for the north and south tails of 0043 + 201. Values are given for slice positions shown in Fig. 5. Data are given in Tables 5 and 6.

84

TABLE 5 0043+201 Northern Tail Minimum Pressure

Number	Distance (kpc)	Diameter (kpc)	S per Beam (mJy per beam)	Volume (kpc ³)	Luminosity (10 ⁴¹ ergs s ⁻¹)	H _{min} (G)	E_{\min} (10 ⁵⁷ ergs)	P_{\min} (dyne cm ⁻²)
1	5.3	0.88	0.15	6.4×10 ⁻¹	6.1×10^{-3}	1.4×10^{-5}	7.4×10^{-4}	4.0×10 ⁻¹¹
2	9.4	0.88	0.06	6.4×10^{-1}	2.4×10^{-3}	1.1×10^{-5}	4.4×10^{-4}	2.3×10^{-11}
3	12.7	0.88	0.53	6.4×10^{-1}	2.1×10^{-2}	2.0×10^{-5}	1.5×10^{-3}	8.1×10^{-11}
4	22.1	0.88	0.06	6.4×10^{-1}	2.2×10^{-3}	1.1×10^{-5}	4.2×10^{-4}	2.2×10^{-11}
5	26.8	0.88	0.11	6.4×10^{-1}	4.3×10^{-3}	1.3×10^{-5}	6.1×10^{-4}	3.2×10^{-11}
6	33.2	0.88	0.14	6.4×10^{-1}	5.7×10^{-3}	1.4×10^{-5}	7.2×10^{-4}	3.8×10^{-11}
7	35.6	0.88	0.10	6.4×10^{-1}	3.9×10^{-3}	1.2×10^{-5}	5.7×10^{-4}	3.1×10^{-11}
8	40.1	0.88	0.08	6.4×10^{-1}	3.1×10^{-3}	1.2×10^{-5}	5.1×10^{-4}	2.7×10^{-11}
9	43.9	4.13	0.61	$1.4 \times 10^{+1}$	2.5×10^{-2}	8.7×10^{-6}	6.2×10^{-3}	1.5×10^{-11}
10	47.7	2.99	1.02	7.3	4.1×10^{-2}	1.2×10^{-5}	6.3×10^{-3}	2.9×10^{-11}
11	52.4	7.82	17.36	$1.7 \times 10^{+2}$	7.0×10^{-1}	1.1×10^{-5}	1.2×10^{-1}	2.4×10^{-11}
12	55.6	8.08	21.92	$1.8 \times 10^{+2}$	8.8×10^{-1}	1.2×10^{-5}	1.4×10^{-1}	2.7×10^{-11}
13	60.7	8.21	24.04	$1.9 \times 10^{+2}$	9.7×10^{-1}	1.2×10^{-5}	1.5×10^{-1}	2.8×10^{-11}
14	65.3	6.91	25.74	$1.3 \times 10^{+2}$	1.0	1.3×10^{-5}	1.4×10^{-1}	3.5×10^{-11}
15	72.5	7.90	13.98	$1.7 \times 10^{+2}$	5.6×10^{-1}	1.0×10^{-5}	1.1×10^{-1}	2.1×10^{-11}
16	78.9	10.53	11.49	$3.1 \times 10^{+2}$	4.6×10^{-1}	8.3×10^{-6}	1.2×10^{-1}	1.4×10^{-11}
17	88.1	13.74	23.56	$1.0 \times 10^{+3}$	9.5×10^{-1}	7.2×10^{-6}	3.2×10^{-1}	1.0×10^{-11}
18	97.2	13.42	23.21	$1.0 \times 10^{+3}$	9.3×10^{-1}	7.3×10^{-6}	3.1×10^{-1}	1.0×10^{-11}
19	107.7	14.95	23.44	$1.2 \times 10^{+3}$	9.4×10^{-1}	6.8×10^{-6}	3.4×10^{-1}	9.3×10^{-12}
20	118.6	17.61	18.40	$1.7 \times 10^{+3}$	7.4×10^{-1}	5.8×10^{-6}	3.4×10^{-1}	6.7×10^{-12}
21	125.3	18.59	13.41	$1.9 \times 10^{+3}$	5.4×10^{-1}	5.2×10^{-6}	3.0×10^{-1}	5.3×10^{-12}
22	133.8	18.16	10.09	$1.8 \times 10^{+3}$	4.1×10^{-1}	4.8×10^{-6}	2.5×10^{-1}	4.6×10^{-12}
23	144.2	21.71	13.36	$2.6 \times 10^{+3}$	5.4×10^{-1}	4.7×10^{-6}	3.4×10^{-1}	4.4×10^{-12}
24	153.2	30.42	17.25	$5.1 \times 10^{+3}$	6.9×10^{-1}	4.2×10^{-6}	5.2×10^{-1}	3.5×10^{-12}
25	168.0	34.60	22.93	$6.6 \times 10^{+3}$	9.2×10^{-1}	4.2×10^{-6}	6.9×10^{-1}	3.5×10^{-12}
26	181.8	29.19	22.96	$4.7 \times 10^{+3}$	9.2×10^{-1}	4.6×10^{-6}	5.9×10^{-1}	4.3×10^{-12}
27	194.0	31.83	20.90	$5.6 \times 10^{+3}$	8.4×10^{-1}	4.3×10^{-6}	6.1×10^{-1}	3.7×10^{-12}
28	204.7	25.67	10.34	$3.7 \times 10^{+3}$	4.1×10^{-1}	4.0×10^{-6}	3.4×10^{-1}	3.1×10^{-12}

to -0.7, and the lobes, although steepening slightly to -0.8, do not show a strong steepening trend.

The results of a minimum pressure analysis of 0110+152 are given in Figure 13 and Tables 7 and 8.

c) 0836+290

Of the sources surveyed, 0836+290 is the largest in extent, spanning 0.5 Mpc. A total-intensity 20 cm image is shown in Figure 14 (Plate 50), and the radio contours overlaid on the optical field are shown in Figure 15 (Plate 51). Imaging of this source was made difficult by its size and the dominance of the core and southern hot spot. Thus the extended structure does not show great detail. The northern jet, however, is quite bright. Details of this jet are shown in Figure 16 (Plate 52). The most outstanding feature of the source, this jet is very bright for 68 kpc and does not disrupt until it is 122 kpc from the core. As well as length, this jet exhibits a nondisrupting bend untypical of WATs. The southern jet, mostly invisible on the images presented here, disrupts in an extraordinarily bright hot spot, having a peak flux density about one-fourth of the core flux density.

Abell 690 is classified as a Bautz-Morgan type I cluster (Roland et al. 1975) and has been discussed by Owen (1975a),

who investigated the luminosity function for Abell clusters of galaxies, and Morganti et al. (1988), who explored the effects of the environment on low-luminosity radio sources. The later group presents an image of the 1400 MHz radio contours overlaid on the Einstein Observatory IPC image of the cluster gas. They point out that the northern jet appears in a high brightness region of the cluster, while both tails are at the edges of the IPC emission. In comparing the equipartition radio pressures to the thermal pressure derived from the X-ray data, they find that the northern jet is overpressured, that is, the nonthermal pressure is greater than the thermal pressure, implying that it is not thermally confined. The lobes, however, are underpressured and could be confined by the thermal material. 0836+290 has been included in the 4C survey by Pilkington and Scott (1965), the Ohio survey by Dixon and Kraus (1968) (1415 MHz), and the B2 survey by Colla et al. (1972) (408 MHz) and Colla et al. (1975) (408, 1415, and 4995 MHz). Radio data have also been presented by Fanti, Fanti, and Londrillo (1969) (178, 408, and 1420 MHz), Boeschaar and Kraus (1971) (1415 MHz), who identify the radio source with Abell 690, Dickel et al. (1971), (610 MHz), Grueff and Vigotti (1972, 1973) (408 and 5000 MHz), Webber et al. (1972), (750, 1400, and 2700 MHz), Willson (1972) (1407 MHz), Owen (1974a), (1400 MHz), Owen

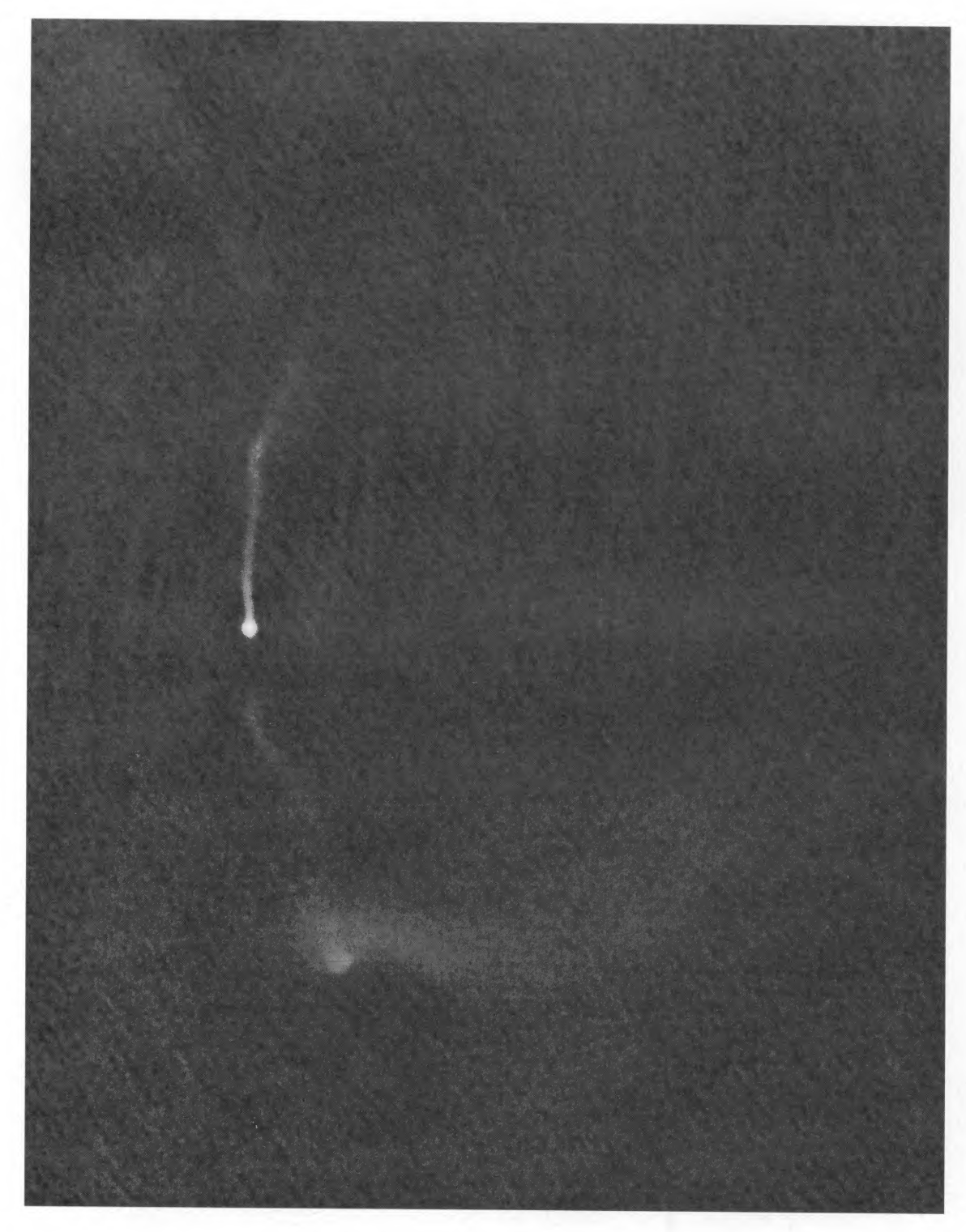


Fig. 14.—High-resolution (1") image of 0836+290 at 20~cm

O'DONOGHUE, OWEN, AND EILEK (see 72, 84)

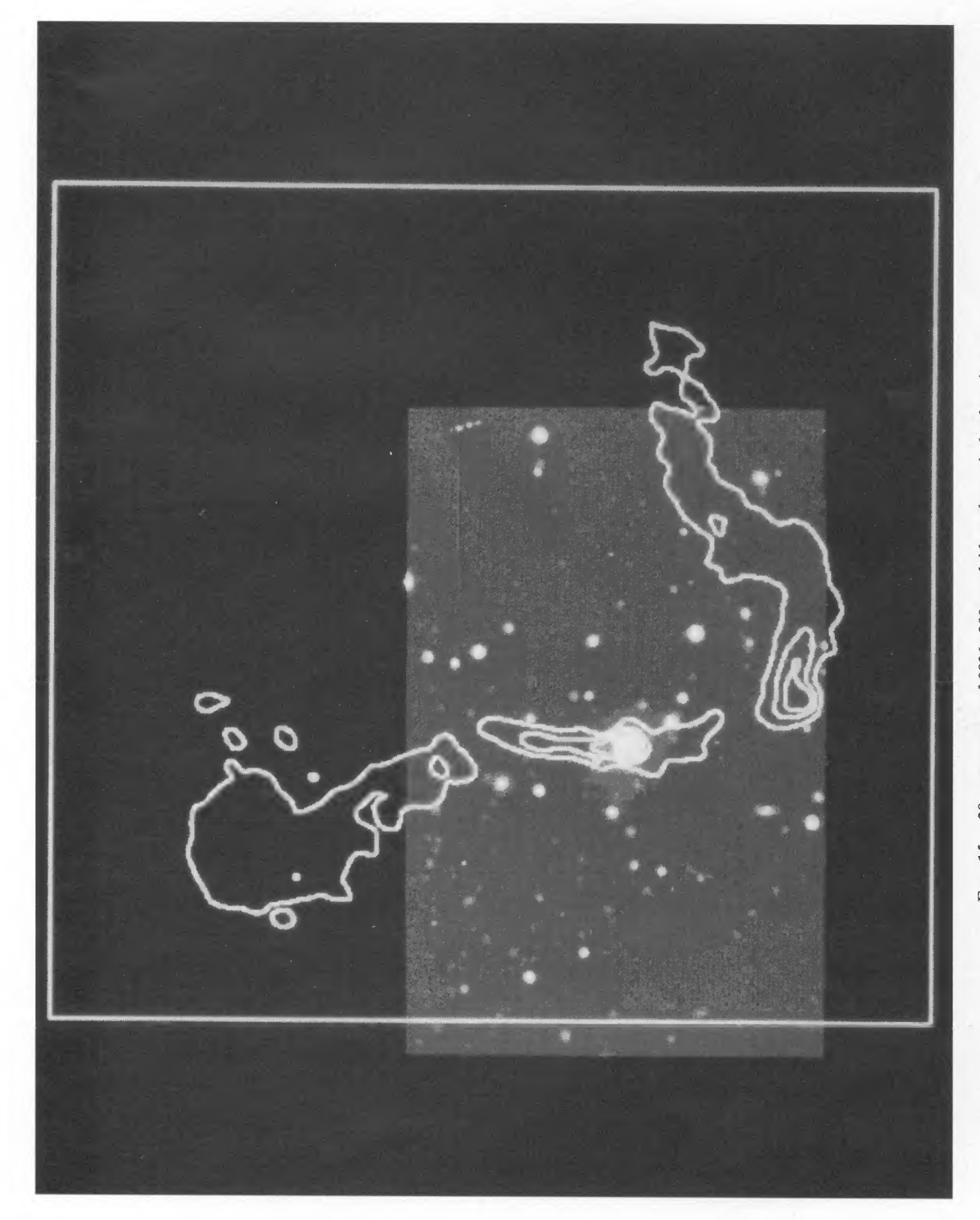


Fig. 15.—20 cm contours of 0836+290 overlaid on the optical galaxy image

O'DONOGHUE, OWEN, AND EILEK (see 72, 84)

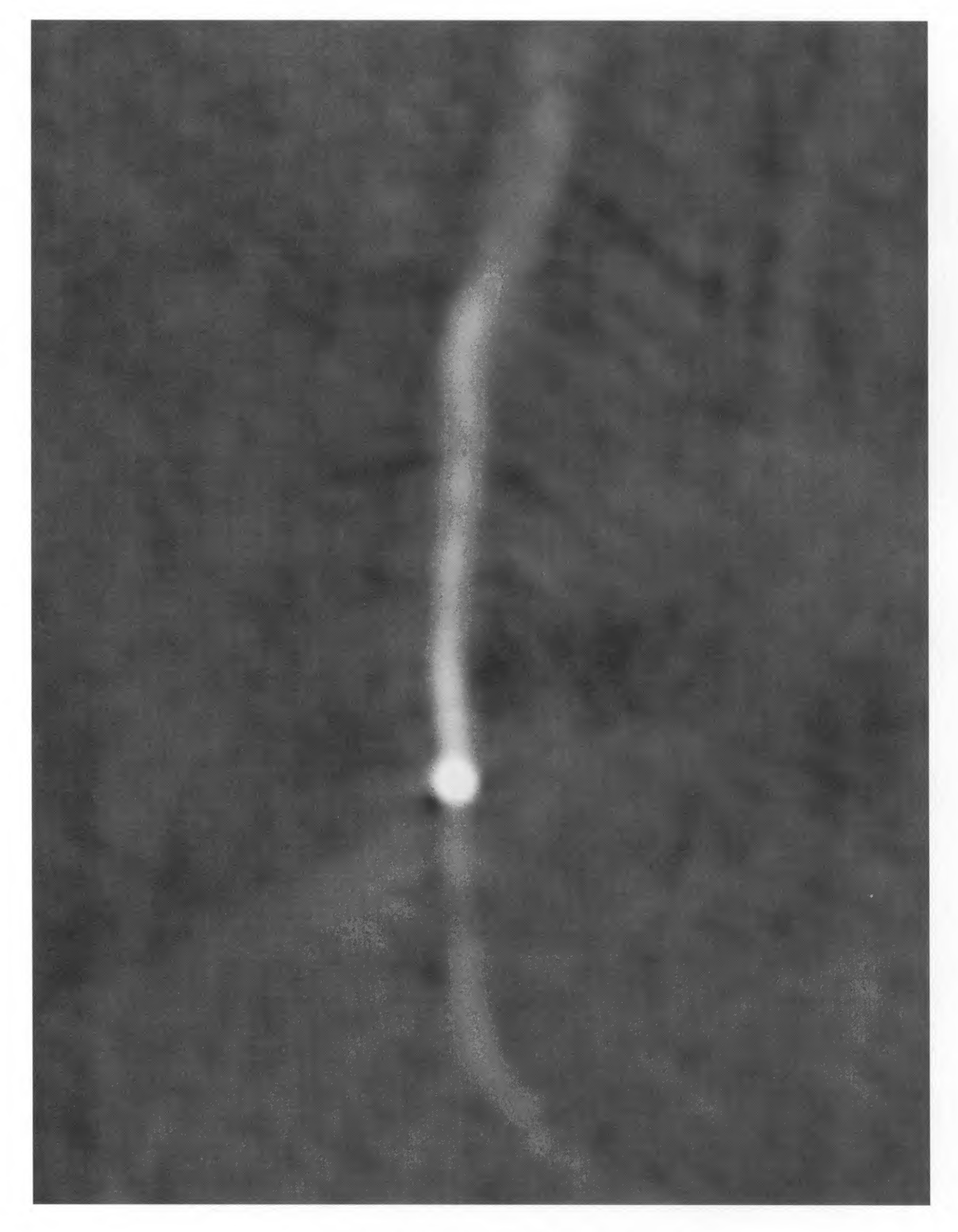


Fig. 16.—Details of the northern jet of 0836+290 at 2" resolution

O'Donoghue, Owen, and Eilek (see 72, 84)

No. 1, 1990

TABLE 6 0043+201 Southern Tail Minimum Pressure

Number	Distance (kpc)	Diameter (kpc)	S per Beam (mJy per beam)	Volume (kpc³)	Luminosity (10 ⁴¹ ergs s ⁻¹)	H _{min} (G)	E_{\min} (10 ⁵⁷ ergs)	P_{\min} (dyne cm ⁻²)
1	3.9	0.88	0.13	6.4×10^{-1}	5.2×10 ⁻³	1.3×10 ⁻⁵	6.6×10 ⁻⁴	3.5×10^{-11}
2	8.6	0.88	0.04	6.4×10^{-1}	1.7×10^{-3}	9.7×10^{-6}	3.5×10^{-4}	1.9×10^{-11}
3	13.6	0.88	0.05	6.4×10^{-1}	2.1×10^{-3}	1.0×10^{-5}	4.0×10^{-4}	2.1×10^{-11}
4	17.3	0.88	0.06	6.4×10^{-1}	2.4×10^{-3}	1.1×10^{-5}	4.2×10^{-4}	2.3×10^{-11}
5	22.8	0.88	0.06	6.4×10^{-1}	2.4×10^{-3}	1.1×10^{-5}	4.3×10^{-4}	2.3×10^{-11}
6	29.6	0.88	0.08	6.4×10^{-1}	3.4×10^{-3}	1.2×10^{-5}	5.2×10^{-4}	2.8×10^{-11}
7	32.3	0.88	0.06	6.4×10^{-1}	2.4×10^{-3}	1.1×10^{-5}	4.3×10^{-4}	2.3×10^{-11}
8	35.6	0.88	0.16	6.4×10^{-1}	6.4×10^{-3}	1.4×10^{-5}	7.5×10^{-4}	4.0×10^{-11}
9	40.8	0.88	0.08	6.4×10^{-1}	3.4×10^{-3}	1.2×10^{-5}	5.2×10^{-4}	2.8×10^{-11}
10	44.1	11.11	4.26	$3.4 \times 10^{+2}$	1.7×10^{-1}	6.0×10^{-6}	7.3×10^{-2}	7.3×10^{-12}
11	49.4	10.91	8.12	$3.3 \times 10^{+2}$	3.3×10^{-1}	7.3×10^{-6}	1.0×10^{-1}	1.1×10^{-11}
12	54.4	10.61	10.28	$3.1 \times 10^{+2}$	4.2×10^{-1}	8.0×10^{-6}	1.2×10^{-1}	1.3×10^{-11}
13	59.8	10.08	14.83	$2.8 \times 10^{+2}$	6.1×10^{-1}	9.1×10^{-6}	1.4×10^{-1}	1.7×10^{-11}
14	64.4	11.22	18.82	$3.5 \times 10^{+2}$	7.7×10^{-1}	9.2×10^{-6}	1.7×10^{-1}	1.7×10^{-11}
15	70.6	12.44	18.32	$4.3 \times 10^{+2}$	7.5×10^{-1}	8.6×10^{-6}	1.9×10^{-1}	1.5×10^{-11}
16	75.5	11.88	17.92	$3.9 \times 10^{+2}$	7.3×10^{-1}	8.8×10^{-6}	1.8×10^{-1}	1.5×10^{-11}
17	82.9	11.29	16.33	$3.5 \times 10^{+2}$	6.7×10^{-1}	8.8×10^{-6}	1.6×10^{-1}	1.5×10^{-11}
18	88.2	12.25	19.32	$4.2 \times 10^{+2}$	7.9×10^{-1}	8.8×10^{-6}	1.9×10^{-1}	1.5×10^{-11}
19	93.9	13.38	35.91	$9.9 \times 10^{+2}$	1.5	8.2×10^{-6}	3.9×10^{-1}	1.3×10^{-11}
20	104.7	15.30	38.54	$1.3 \times 10^{+3}$	1.6	7.8×10^{-6}	4.6×10^{-1}	1.2×10^{-11}
21	118.6	17.92	37.54	$1.8 \times 10^{+3}$	1.5	7.0×10^{-6}	5.1×10^{-1}	9.8×10^{-12}
22	125.5	18.19	32.09	$1.8 \times 10^{+3}$	1.3	6.7×10^{-6}	4.8×10^{-1}	8.8×10^{-12}
23	139.1	17.69	17.44	$1.7 \times 10^{+3}$	7.1×10^{-1}	5.7×10^{-6}	3.3×10^{-1}	6.4×10^{-12}
24	146.7	13.34	11.12	$9.9 \times 10^{+2}$	4.5×10^{-1}	5.9×10^{-6}	2.0×10^{-1}	6.9×10^{-12}
25	154.6	13.68	10.41	$1.0 \times 10^{+3}$	4.3×10^{-1}	5.7×10^{-6}	2.0×10^{-1}	6.4×10^{-12}
26	165.4	16.96	10.23	$1.6 \times 10^{+3}$	4.2×10^{-1}	5.0×10^{-6}	2.3×10^{-1}	5.0×10^{-12}
27		17.12	6.87	$1.6 \times 10^{+3}$	2.8×10^{-1}	4.4×10^{-6}	1.9×10^{-1}	3.9×10^{-12}
28	190.1	23.30	11.73	$3.0 \times 10^{+3}$	4.8×10^{-1}	4.3×10^{-6}	3.3×10^{-1}	3.7×10^{-12}
29	197.3	30.30	17.77	$5.1 \times 10^{+3}$	7.3×10^{-1}	4.2×10^{-6}	5.3×10^{-1}	3.5×10^{-12}
30	201.0	34.33	20.31	$6.5 \times 10^{+3}$	8.3×10^{-1}	4.1×10^{-6}	6.3×10^{-1}	3.3×10^{-12}
31	207.9	40.80	22.52	$9.2 \times 10^{+3}$	9.2×10^{-1}	3.8×10^{-6}	7.8×10^{-1}	2.9×10^{-12}
32	220.6	30.80	17.27	$5.3 \times 10^{+3}$	7.1×10^{-1}	4.1×10^{-6}	5.3×10^{-1}	3.4×10^{-12}
33	228.7	27.45	11.08	$4.2 \times 10^{+3}$	4.5×10^{-1}	3.9×10^{-6}	3.7×10^{-1}	3.0×10^{-12}

(1975b), (2695 MHz), Roland et al. (1975) (2700 MHz), Owen, Rudnick, and Peterson (1977), (2695 MHz), Fanti et al. (1978), (408 and 1415 MHz), Valentijn (1979a) (610 MHz), who classifies it a WAT by the spectral index behavior, and Valentijn (1979b). More recently, it has been used as an example of the subclass of large WATs as designated by Burns (1986) and a candidate for bending by dark clouds (Burns, Norman, and Clarke 1986). Parma et al. (1987) have discussed it in a study of radio jets at 1400 MHz, determining the sidedness of the jets to be always greater than 4.

i) Polarization

The polarization is shown in Figure 17. Both the northern jet and southern hot spot show significant polarized flux. At 20 cm full resolution, the northern jet starts out being $\sim 20\%$ polarized and increases smoothly to $\sim 40\%$ polarization. The southern hot spot is $\sim 20\%$ polarized at the farthest point from the core, and up to 70% polarized closer to the core. This behavior is similar at 6 cm, except that the increase in

the jet is from $\sim 30\%$ to $\sim 50\%$, while the hot spot shows 50% to 80% polarization.

In the displayed contour plot it can be seen that the vectors are perpendicular to the edge of the southern hot spot. While the rotation measure is not known, this might suggest that the magnetic field is oriented along the curve. Such an orientation of the polarization vectors is typical of the sources in this paper. Although some cluster sources exhibit large rotation measures (e.g., M87 in Hines, Owen, and Eilek 1990), WATs are typically found in clusters that do not exhibit the high central X-ray emissivities that identify cooling flows (Norman, Burns, and Sulkanen 1988). There is not yet evidence for large rotation measures in noncooling flow clusters (Burns, private communication).

ii) Spectral Index and Minimum Pressure Analysis

Spectral information was found from the slices shown in Figure 18; the results are given in Figure 19. Difficulties in the imaging prevented many details from being observed in the

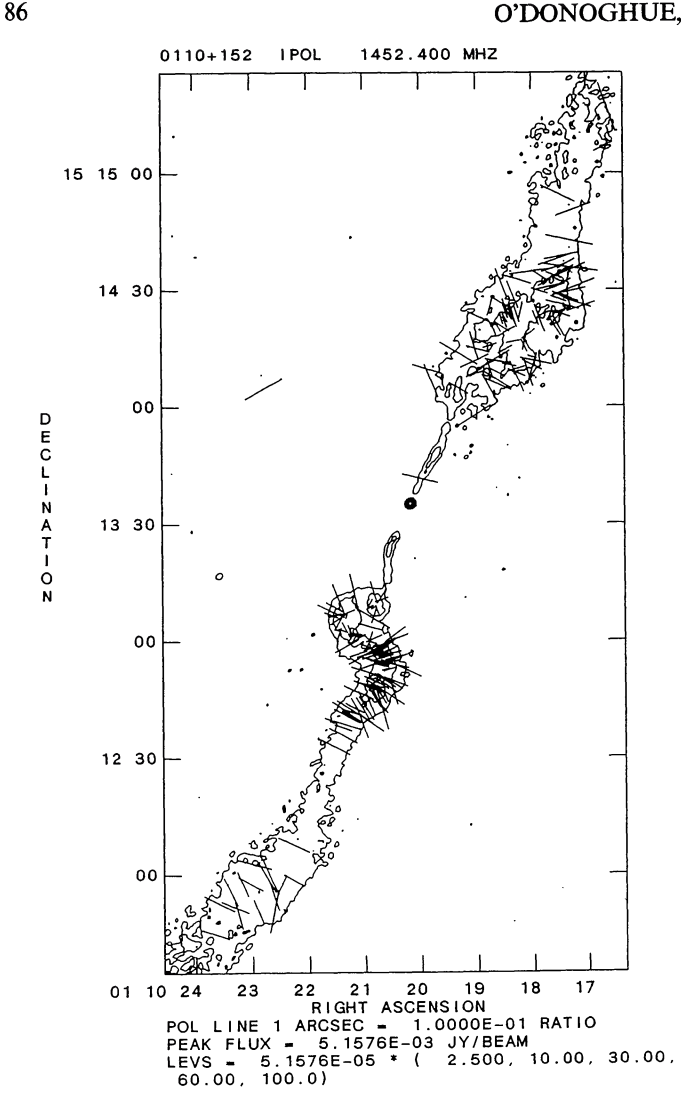


Fig. 10.—Polarization angles for the inner part of 0110+152 uncorrected for Faraday rotation. Polarized emission further out than shown in this image is less than 3 σ above the noise. Contours are those of the full resolution 20 cm image, and lengths of the vectors are proportional to the fractional polarization at 6 cm.

spectral index. The tendency to steepen along the tails (from about -0.5 to less than -1) and the flattening at the southern hot spot are the notable features.

The results of the minimum pressure analysis are shown in Figure 20 and are given in Tables 9 and 10.

d) 0908-103

0908-103 is the physically largest source in the sample. This source was imaged at 365 MHz by Ghigo and Owen (1973). The 20 cm image, at 4" resolution, is shown in Figure 21 (Plate 53). This is an unusual WAT in that it exhibits no particular hot spots, but rather knots in the tails that are not accompanied by bends. Also, the entire source curves instead of having a distinct, localized bend. The gentleness of the curve and the symmetry makes it appear to be a NAT attached to a slow-moving galaxy. Strongly core-dominated,

and accompanied by a very bright confusing source to the west, the extended structure is completely lost at full resolution. Thus, only low-resolution images are presented and analyzed.

i) Source Morphology

As a result of the low signal-to-noise ratio, low resolution was required, and no detailed features are observed in this source. With higher resolution, how the knots occur while the general trend of the tail continues may be quite interesting. However, the bend of the entire source is the only feature noted here. The radio contours are shown overlaid on the optical galaxy image in Figure 22 (Plate 54). 0908-103 and a bright background source to the west are shown in Figure 23 (Plate 55). The background source appears also to be a WAT, although one at greater distance than 0908-103.

ii) Polarization

The polarized flux density is not apparent above the noise until the data are tapered to an 8" resolution image. The values are all less than 30% for the 20 cm image and less than 40% for the 6 cm image, both increasing away from the core as in other WATs. The fractional polarization vectors at 6 cm are shown in Figure 24.

iii) Spectral Index and Minimum Pressure Analysis

Slice centers and numbers are shown in Figure 25. The spectral index values at the slices are shown in Figure 26. In general, the spectral index is smooth and, disregarding spurious edge effects, steepens from -0.5 at the beginning of the northern tail to -1.3 at its end. The southern tail steepens to -1.3.

The minimum pressure estimates of magnetic field, energy per slice, and pressure are shown in Figure 27 and are presented in Tables 11 and 12.

e) 1159+583

At low resolution, this small source exhibits classic WAT features of smooth tails and localized bends. It is slightly asymmetric in that the southern tail is longer and narrower than the northern tail. A high resolution image at 20 cm is shown in Figure 28 (Plate 56). It is clear from this image that this source displays a wealth of internal structure. More than any other single source, these features may call into question the conventional interpretation of radio tails as uniformly filled cylinders. The radio contours overlaid on the optical image of the galaxy are shown in Figure 29 (Plate 57).

The cluster, Abell 1446, is classified a Bautz-Morgan type I with a single dominant galaxy by McHardy (1974), but later work by Leir and van den Bergh (1977) classifies it as type II-III. The cluster was more extensively studied by Burns and Balonek (1982), who claim it is an early, dynamically unevolved cluster. From Einstein Observatory IPC observations, they calculate an ICM thermal pressure of 6.6×10^{-12} dyne cm⁻². They present a contour plot of the X-ray emission overlaid on the optical field and indicate the position and orientation of the radio source with respect to the ICM. The radio source is south of the X-ray peak, with the southern tail

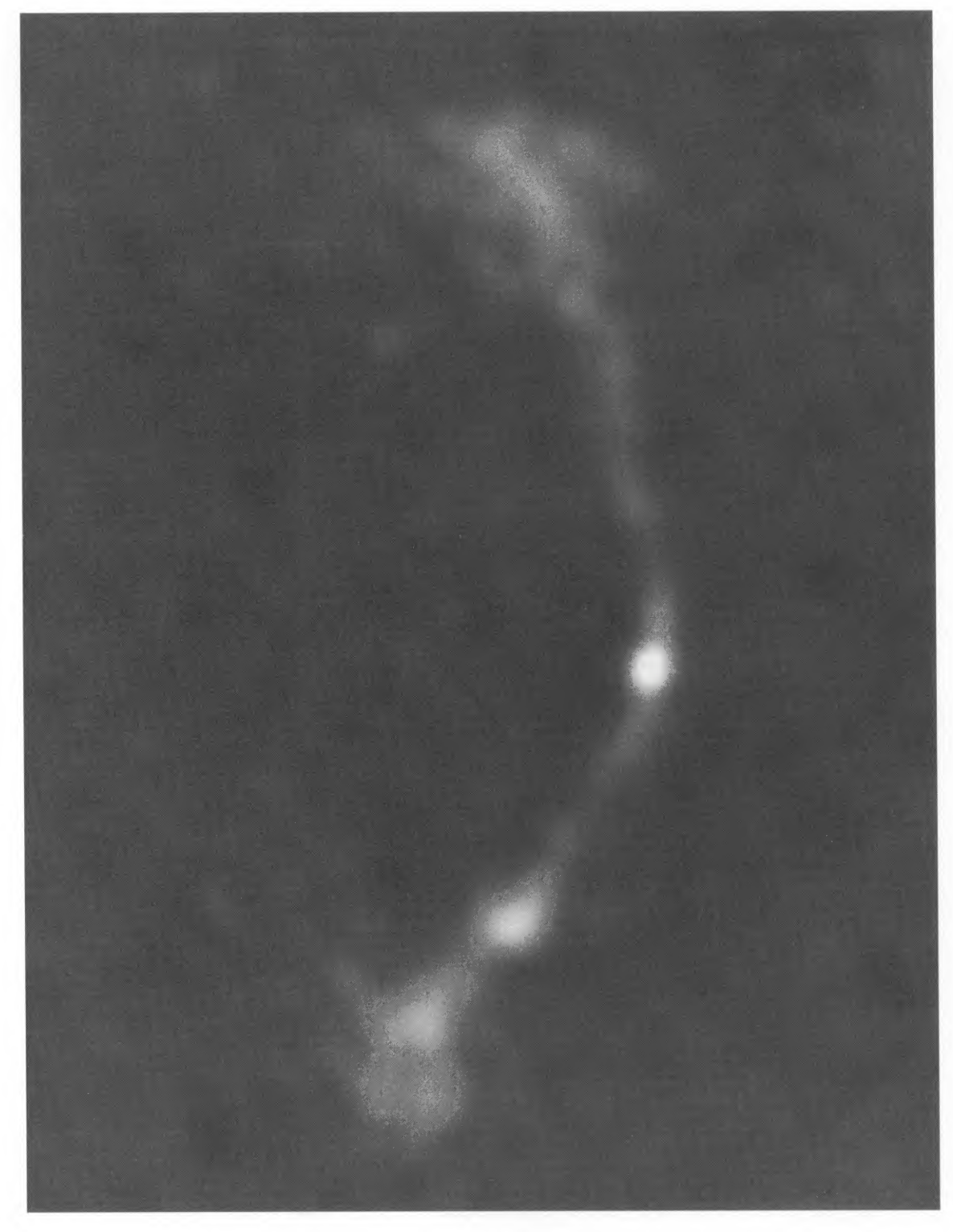
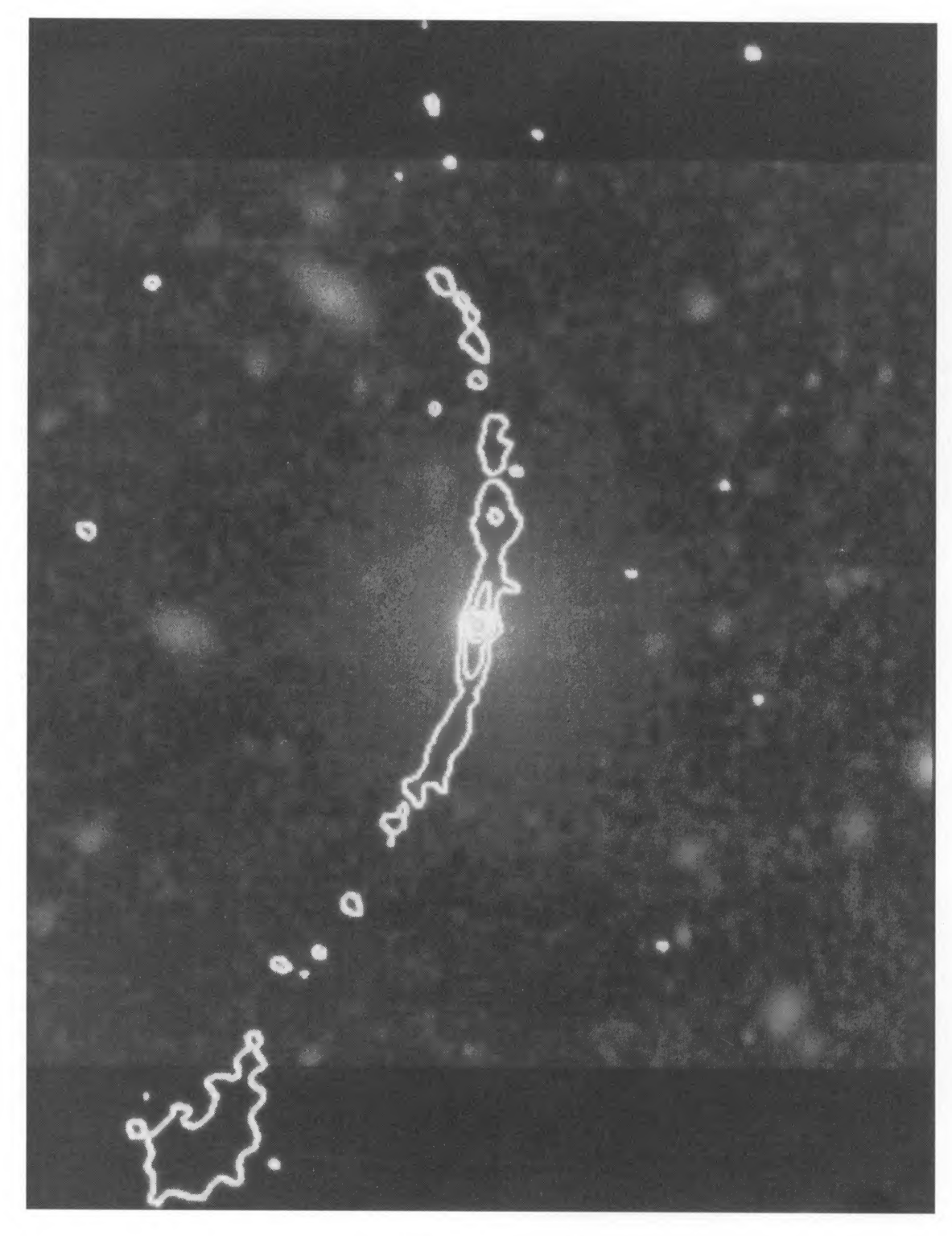


Fig. 21.—Low-resolution (4") image of 0908-103 at 20 cm

O'DONOGHUE, OWEN, AND EILEK (see 72, 86)



 $\label{eq:Fig. 22.} Fig. 22.-20~cm~contours~of~0908-103~overlaid~on~the~optical~galaxy~image~O'Donoghue,~Owen,~and~Eilek~(\textit{see}~72,~86)$

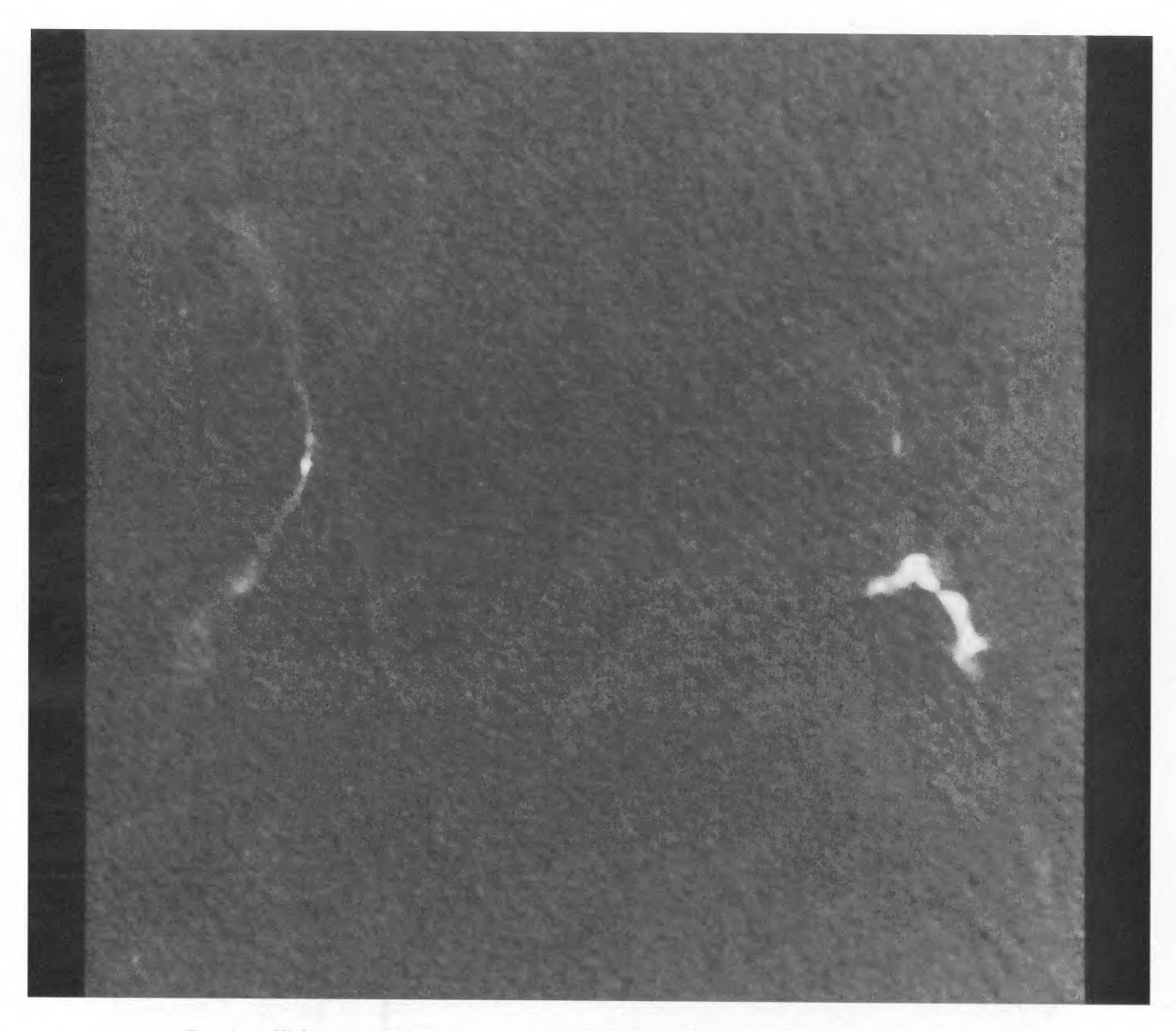


Fig. 23.—High-resolution (2") 20 cm image of 0908-103, including the confusing source to the west O'Donoghue, Owen, and Eilek (see 72, 86)



Fig. 28.—High-resolution (1") image of 1159+583 at 20~cm

O'Donoghue, Owen, and Eilek (see 72, 86)

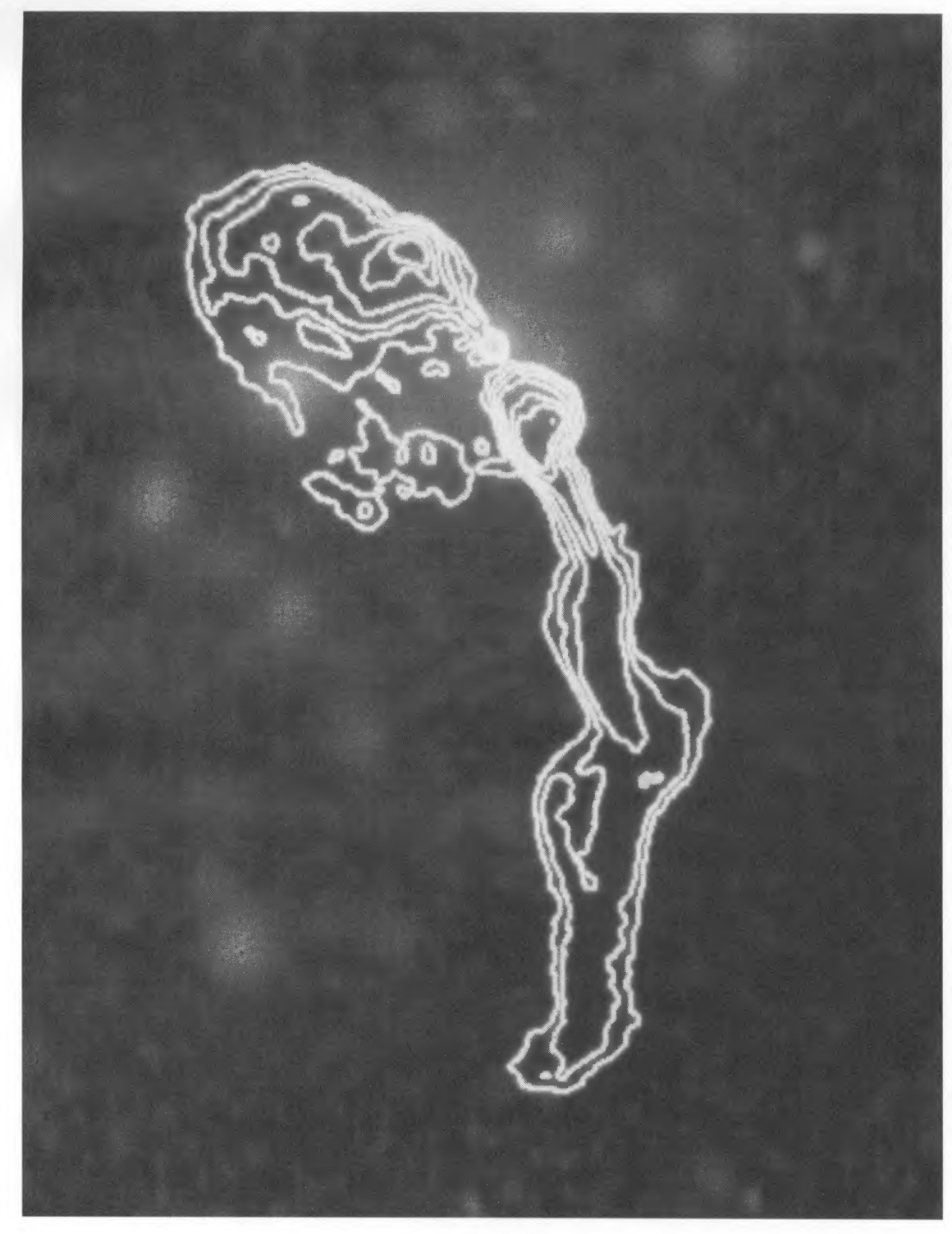
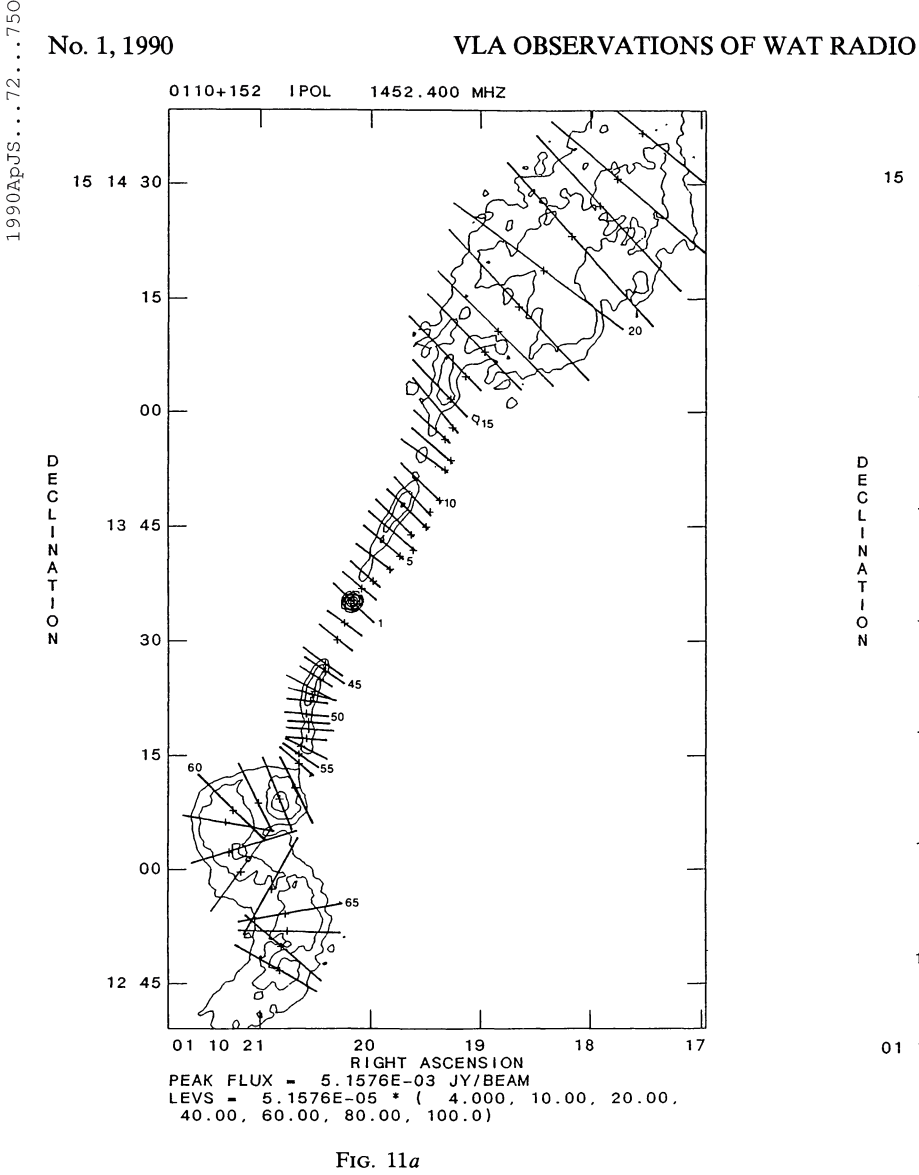


Fig. 29.—20 cm contours of 1159+583 overlaid on the optical galaxy image

O'Donoghue, Owen, and Eilek (see 72, 86)



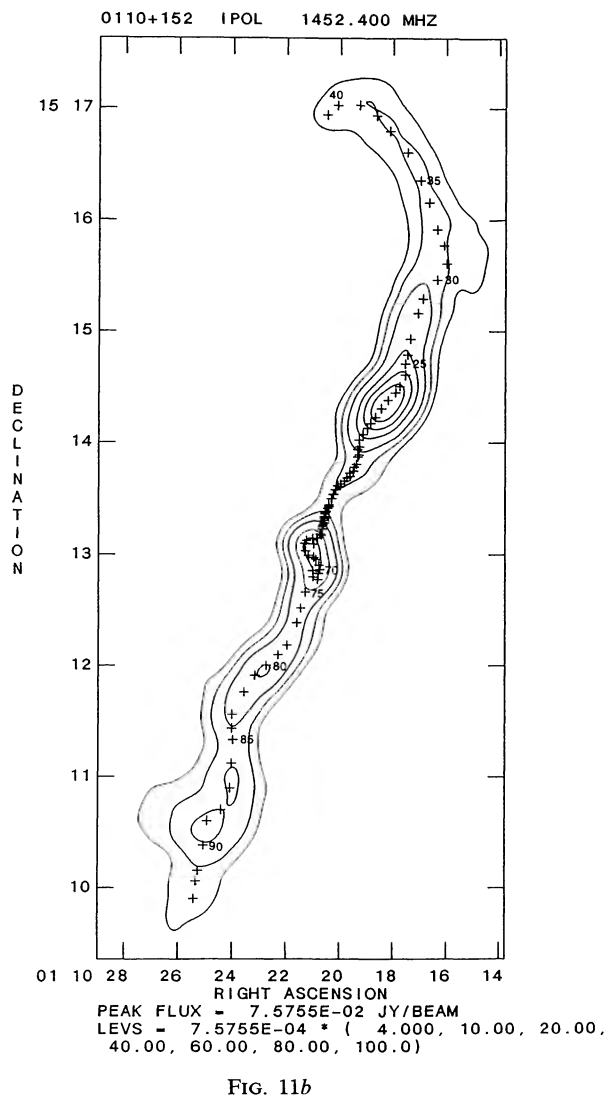


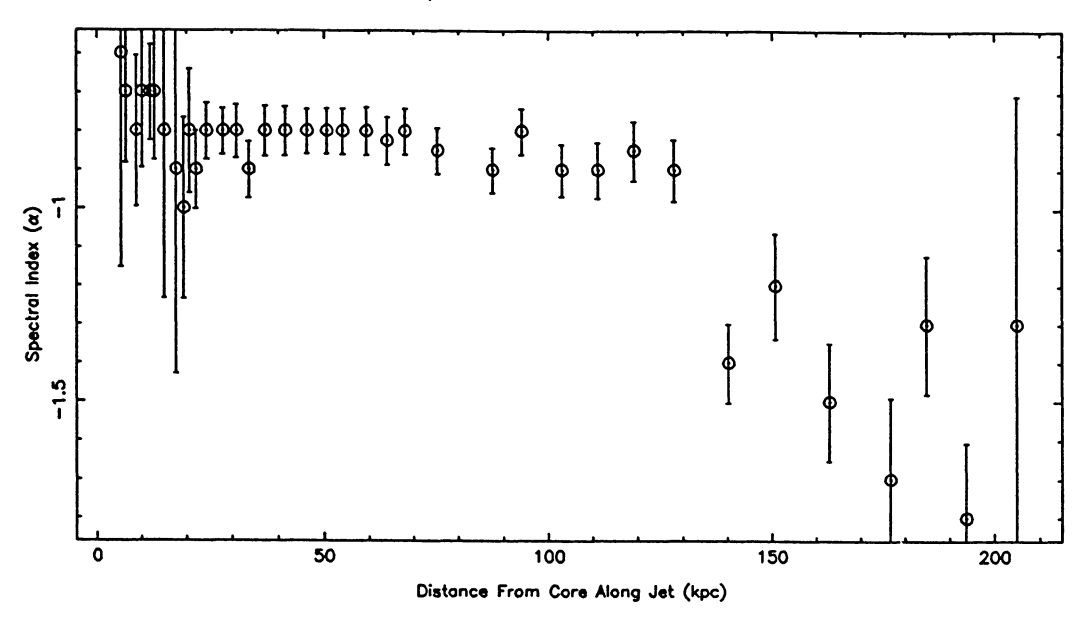
Fig. 11.—Positions of the centers of slices taken perpendicular to the jets and tails of 0110+152. (a) Slices in the inner part of the source; (b) all of the slices. Spectral indices and minimum pressure values for these slices are shown in Figs. 12 and 13.

extending along the gradient. The final claim by Burns and Balonek is that the source could be bent by dynamic pressure from slow (~ 200 km s⁻¹) galaxy motion with respect to the ICM acting with buoyancy. Radio observations are reported by Ghigo and Owen (1973) (2695 MHz), Owen (1975b) (2695 MHz), Owen and Rudnick (1976), who include this source in the original six WATs defining the class, Rudnick and Owen (1977) (2695 and 8085 MHz), McHardy (1978a, b) (408, 1407, and 2700 MHz), Simon (1978), Valentijn (1979a, b), Harris, Kapahi, and Ekers (1980) (1415 MHz), and Burns (1986), who gives this as an example of intermediate WATs in his size classification. The most extensive studies of this source, however, are by Burns, Owen, and Rudnick (1979) and Burns and Balonek (1982). The first study noted the "recollimation" of the southern tail past the hot spot and derived minimum pressure energy, magnetic field, and pressure values of 5×10^{56} ergs s⁻¹, 13 μ G, and 3×10^{-12} dyne cm⁻² for the southern tail assuming a filled cylinder. They also derive an upper limit to the electron density from the polarization data at 2695 MHz of 7×10^{-4} cm⁻³ for the recollimated southern tail. Comparison of the data to the independent blob model (Jaffe and Perola 1973) indicated a blob density up to 200 times that derived from the polarization data in order for the blobs to form the southern tail. The plasma beam model was more successful in explaining their data, allowing bending by both the dynamic pressure of the galaxy and the buoyant force of the ICM for a nonrelativistic, subsonic (below the ICM sound speed) beam.

i) Source Structure

The most remarkable features in this source are the filaments south of the northern tail. These were completely unsuspected and present in their existence, form, and orienta-





Spectral Index for the Southern Tail

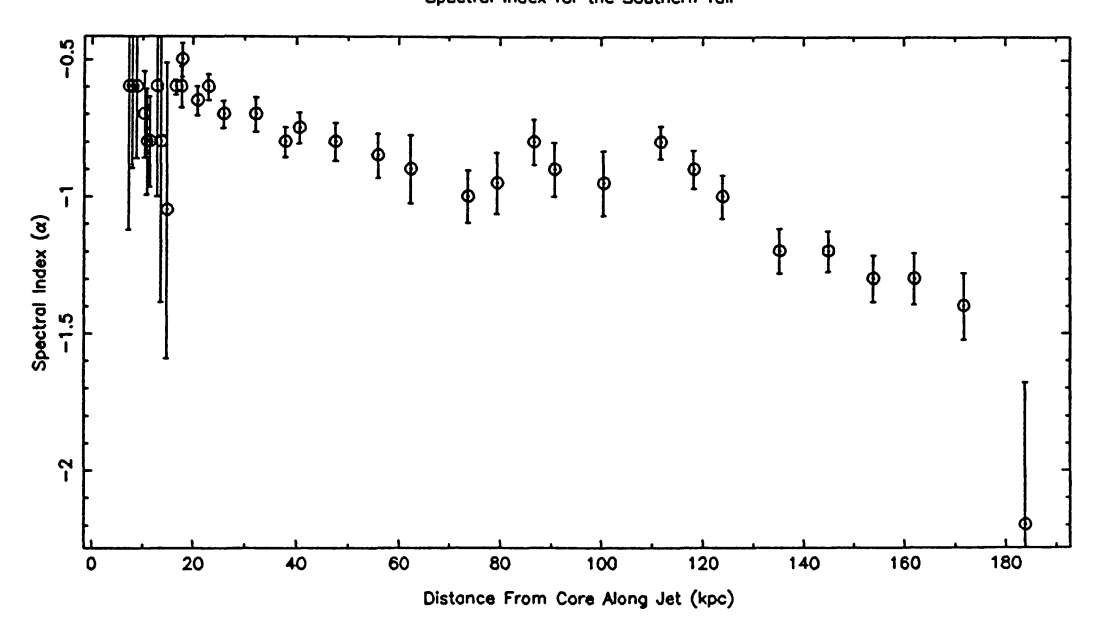


FIG. 12.—Spectral index values between 6 and 20 cm for 0110+152. Values were determined using estimated mean values from slices taken across the total intensity maps, at positions shown in Fig. 11.

tion, a new challenge in the ongoing study of WATs. They are long and thin ($\sim 20''$ long and <1'' wide [unresolved]), curving and intertwining, and all end abruptly along the same line. This last phenomenon may be due to bending in the projected dimension. In local flux density, they tend to be ~ 10 times the interfilament (noise) value. The 6 cm image shown in the top left corner of Figure 30 (Plate 58) lacks the details of the lower frequency image.

ii) Polarization

At 20 cm, the polarized flux density is quite patchy with the arc in the northern lobe and the recollimation area and second narrowing in the southern lobe being the only features above the noise. At 6 cm, the northern edge of the northern lobe and the arc are quite bright. In addition, most of the southern tail is also bright: the hot spot, the recollimation

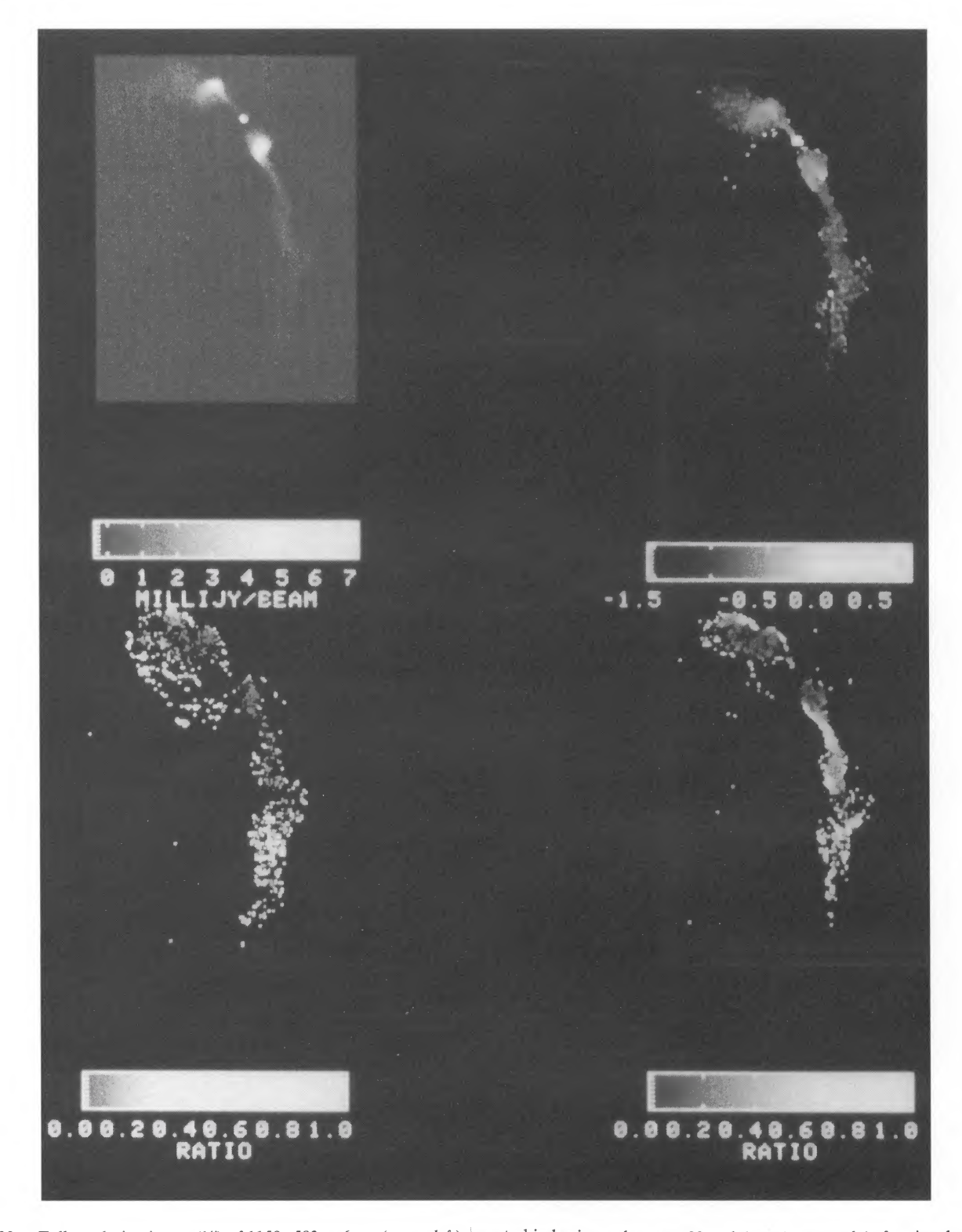


Fig. 30.—Full resolution image (1") of 1159+583 at 6 cm (upper left); spectral index image between 20 and 6 cm (upper right); fractional polarization at 20 cm (lower left) and at 6 cm (lower right).

O'DONOGHUE, OWEN, AND EILEK (see 72, 88)

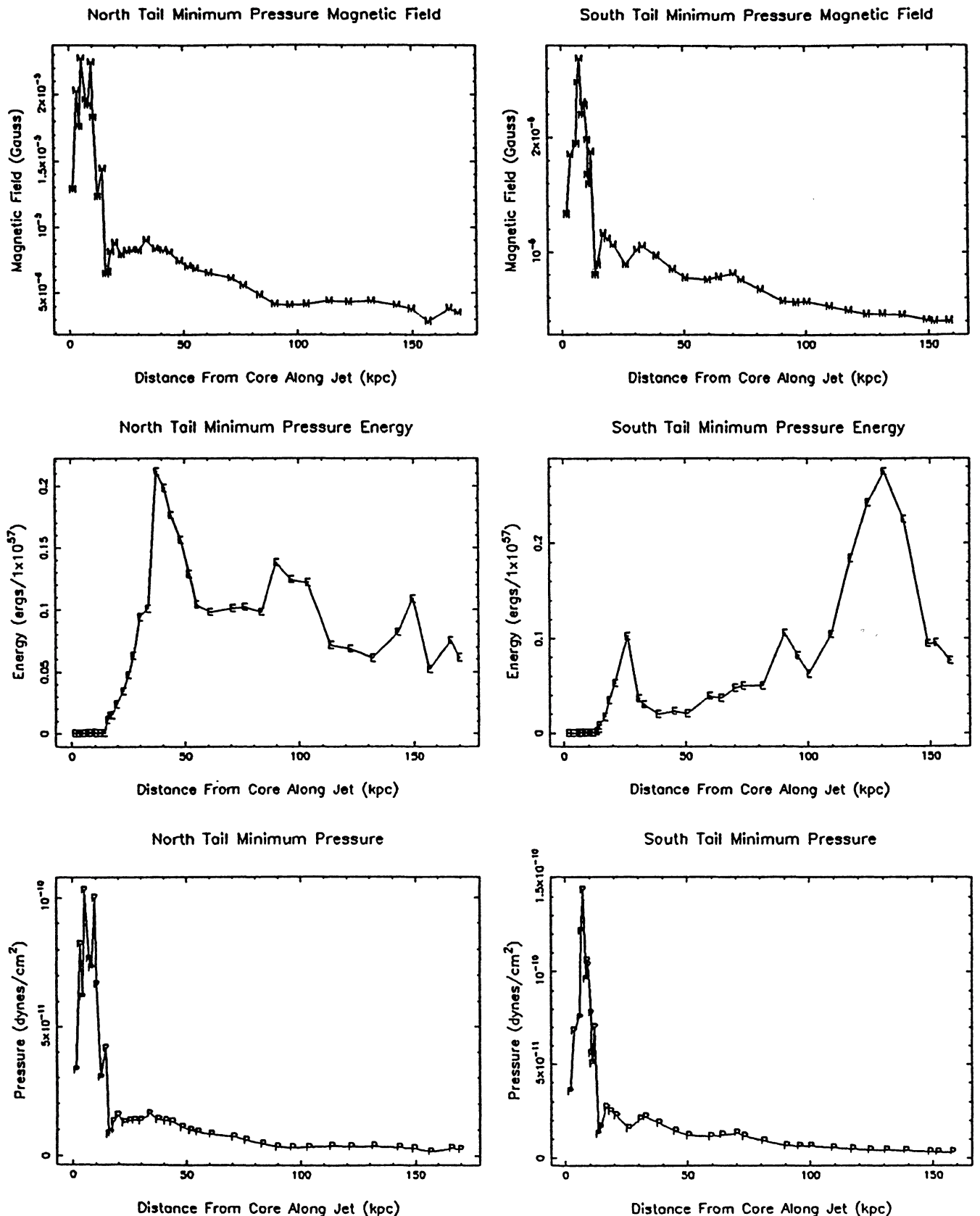


FIG. 13.—Estimates of the magnetic field, total energy (within one slice across the tail), and pressure, derived from minimum pressure arguments, for the north and south tails of 0110+152. Values are given for slice positions shown in Fig. 11. Data are given in Tables 7 and 8.

TABLE 7
0110+152 Northern Tail Minimum Pressure

Number	Distance (kpc)	Diameter (kpc)	S per Beam (mJy per beam)	Volume (kpc³)	Luminosity (10 ⁴¹ ergs s ⁻¹)	H _{min} (G)	E_{\min} (10 ⁵⁷ ergs)	P_{\min} (dyne cm ⁻²)
2	1.7	0.42	0.06	7.0×10^{-2}	3.5×10^{-4}	1.3×10^{-5}	6.8×10^{-5}	3.3×10^{-11}
3	3.9	0.42	0.29	7.0×10^{-2}	1.7×10^{-3}	2.0×10^{-5}	1.7×10^{-4}	8.2×10^{-11}
4	5.3	0.36	0.13	5.0×10^{-2}	7.5×10^{-4}	1.8×10^{-5}	9.1×10^{-5}	6.2×10^{-11}
5	6.4	0.36	0.31	5.0×10^{-2}	1.8×10^{-3}	2.3×10^{-5}	1.5×10^{-4}	1.0×10^{-10}
6	8.8	0.66	0.63	1.7×10^{-1}	3.7×10^{-3}	2.0×10^{-5}	3.8×10^{-4}	7.6×10^{-11}
7	10.0	0.71	0.67	2.0×10^{-1}	3.9×10^{-3}	1.9×10^{-5}	4.2×10^{-4}	7.3×10^{-11}
8	11.9	0.71	1.17	2.0×10^{-1}	6.8×10^{-3}	2.2×10^{-5}	5.8×10^{-4}	1.0×10^{-10}
9	12.8	0.73	0.60	2.1×10^{-1}	3.5×10^{-3}	1.8×10^{-5}	4.0×10^{-4}	6.7×10^{-11}
10	15.0	1.24	0.44	6.1×10^{-1}	2.5×10^{-3}	1.2×10^{-5}	5.3×10^{-4}	3.0×10^{-11}
11	17.6	0.93	0.43	3.4×10^{-1}	2.5×10^{-3}	1.4×10^{-5}	4.2×10^{-4}	4.2×10^{-11}
12	19.3	5.31	3.39	$4.5 \times 10^{+1}$	2.0×10^{-2}	6.4×10^{-6}	1.1×10^{-2}	8.3×10^{-12}
13	20.5	5.93	4.67	$5.6 \times 10^{+1}$	2.0×10^{-2}	6.6×10^{-6}	1.1×10^{-2}	8.7×10^{-12}
14	22.0	4.91	6.53	$3.8 \times 10^{+1}$	3.8×10^{-2}	8.1×10^{-6}	1.5×10^{-2}	1.3×10^{-11}
15	24.3	5.69	11.61	$5.1 \times 10^{+1}$	6.8×10^{-2}	8.8×10^{-6}	2.3×10^{-2}	1.5×10^{-11}
16	27.9	7.62	14.49	9.2×10 ⁺¹	8.4×10^{-2}	7.9×10^{-6}	3.4×10^{-2}	1.3×10^{-11}
17	30.9	8.70	21.10	$1.2 \times 10^{+2}$	1.2×10^{-1}	8.2×10^{-6}	4.7×10^{-2}	1.3×10^{-11} 1.3×10^{-11}
18	33.5	9.94	28.31	$1.6 \times 10^{+2}$	1.6×10^{-1}	8.3×10^{-6}	6.3×10^{-2}	1.4×10^{-11}
19	37.1	12.19	42.16	$2.4 \times 10^{+2}$	2.5×10^{-1}	8.2×10^{-6}	9.4×10^{-2}	1.3×10^{-11}
20	41.5	11.56	51.66	$2.1 \times 10^{+2}$	3.0×10^{-1}	9.0×10^{-6}	1.0×10^{-1}	1.6×10^{-11}
21	46.3	10.42	97.16	5.2×10 ⁺²	5.7×10^{-1}	8.4×10^{-6}	2.1×10^{-1}	1.4×10^{-11}
22	50.6	10.42	88.91	$5.0 \times 10^{+2}$	5.7×10^{-1} 5.2×10^{-1}	8.2×10^{-6}	2.0×10^{-1}	1.3×10^{-11}
23	54.1	9.82	77.09	$4.6 \times 10^{+2}$	4.5×10^{-1}	8.1×10^{-6}	1.8×10^{-1}	1.3×10^{-11}
24	59.4	10.09	60.01	$4.9 \times 10^{+2}$	3.5×10^{-1}	7.4×10^{-6}	1.6×10^{-1}	1.3×10^{-11} 1.1×10^{-11}
25	64.0	9.69	45.46	$4.5 \times 10^{+2}$	2.6×10^{-1}	7.0×10^{-6}	1.3×10^{-1}	9.8×10^{-12}
26	68.1	8.96	35.20	$3.8 \times 10^{+2}$	2.1×10^{-1}	6.8×10^{-6}	1.0×10^{-1}	9.2×10^{-12}
27	75.3	9.14	30.84	$4.0 \times 10^{+2}$	1.8×10^{-1}	6.5×10^{-6}	9.8×10^{-2}	8.4×10^{-12}
28	87.5	9.1 4 9.87	28.91	$4.6 \times 10^{+2}$	1.8×10^{-1} 1.7×10^{-1}	6.3×10^{-6}	9.8×10^{-1} 1.0×10^{-1}	7.4×10^{-12}
29	94.0	10.91	25.35	$5.7 \times 10^{+2}$	1.7×10^{-1} 1.5×10^{-1}	5.5×10^{-6}	1.0×10^{-1} 1.0×10^{-1}	6.1×10^{-12}
30	102.9	12.24	19.90	$7.1 \times 10^{+2}$	1.3×10^{-1} 1.2×10^{-1}	4.8×10^{-6}	9.8×10^{-2}	4.7×10^{-12}
21	111.0	16.91	22.19	1.4×10 ⁺³	1.3×10^{-1}	4.2×10^{-6}	1.4×10^{-1}	3.4×10^{-12}
31	111.0	16.43	19.40	1.4×10^{-1} $1.3 \times 10^{+3}$	1.3×10^{-1} 1.1×10^{-1}	4.2×10^{-6} 4.1×10^{-6}	1.4×10^{-1} 1.2×10^{-1}	3.4×10^{-12} 3.3×10^{-12}
32	119.1	15.94	19.40	1.3×10 $1.2 \times 10^{+3}$	1.1×10 1.1×10^{-1}	4.1×10^{-6}	1.2×10^{-1} 1.2×10^{-1}	3.4×10^{-12}
33 34	140.2	13.94	12.62	$6.2 \times 10^{+2}$	7.4×10^{-2}	4.1×10 4.4×10^{-6}	7.1×10^{-2}	3.9×10^{-12}
35	150.7	11.41	11.69	$6.2 \times 10^{+2}$	6.8×10^{-2}	4.4×10^{-6}	6.8×10^{-2}	3.7×10^{-12}
26	162.9	10.50	10.66	5.3×10 ⁺²	6.2×10^{-2}	4.4×10^{-6}	6.1×10^{-2}	3.9×10^{-12}
36		10.58 13.27	10.66 12.79	$8.4 \times 10^{+2}$	6.2×10^{-2}	4.4×10^{-6} 4.1×10^{-6}	8.2×10^{-2}	3.9×10^{-12} 3.3×10^{-12}
37	176.6	16.43	15.30	0.4×10^{-2} $1.3 \times 10^{+3}$	8.9×10^{-2}	3.8×10^{-6}	8.2×10^{-1} 1.1×10^{-1}	2.9×10^{-12}
38	184.7	15.13	4.75	$1.3 \times 10^{+3}$ $1.1 \times 10^{+3}$	$\frac{8.9 \times 10^{-2}}{2.8 \times 10^{-2}}$	2.8×10^{-6}	5.2×10^{-2}	1.6×10^{-12}
39	205.0	13.13	4.75 10.73	$8.7 \times 10^{+2}$	6.3×10^{-2}	2.8×10^{-6} 3.8×10^{-6}	5.2×10^{-2} 7.5×10^{-2}	1.6×10^{-12} 2.9×10^{-12}
40 41	203.0	13.30	7.63	$8.7 \times 10^{+2}$ $8.5 \times 10^{+2}$	4.4×10^{-2}	3.8×10^{-6} 3.5×10^{-6}	6.1×10^{-2}	2.9×10^{-12} 2.5×10^{-12}
	207.0						0.1/(10	2.5 / 10

TABLE 8
0110+152 SOUTHERN TAIL MINIMUM PRESSURE

Number	Distance (kpc)	Diameter (kpc)	S per Beam (mJy beam)	Volume (kpc³)	Luminosity (10 ⁴¹ ergs s ⁻¹)	H _{min} (G)	E_{\min} (10 ⁵⁷ ergs)	P _{min} (dyne cm ⁻²)
42	2.4	0.42	0.06	7.0×10^{-2}	3.1×10 ⁻⁴	1.3×10 ⁻⁵	7.3×10^{-5}	3.5×10^{-11}
43	4.3	0.15	0.02	9.2×10^{-3}	1.3×10^{-4}	1.9×10^{-5}	1.8×10^{-5}	6.8×10^{-11}
44	7.3	0.53	0.33	1.1×10^{-1}	1.8×10^{-3}	1.9×10^{-5}	2.1×10^{-4}	7.5×10^{-11}
45	8.0	0.39	0.41	5.9×10^{-2}	2.2×10^{-3}	2.5×10^{-5}	2.1×10^{-4}	1.2×10^{-10}
46	8.9	0.28	0.28	3.0×10^{-2}	1.5×10^{-3}	2.7×10^{-5}	1.3×10^{-4}	1.4×10^{-10}
47	10.4	0.65	0.76	1.6×10^{-1}	4.1×10^{-3}	2.2×10^{-5}	4.6×10^{-4}	9.6×10^{-11}
48	10.9	0.54	0.64	1.2×10^{-1}	3.5×10^{-3}	2.3×10^{-5}	3.6×10^{-4}	1.1×10^{-10}
49	11.5	0.55	0.62	1.2×10^{-1}	4.4×10^{-3}	2.3×10^{-5}	3.6×10^{-4}	1.0×10^{-10}
50	12.9	0.43	0.23	7.2×10^{-2}	1.3×10^{-3}	2.0×10^{-5}	1.7×10^{-4}	7.8×10^{-11}
51	13.0	0.57	0.23	1.3×10^{-1}	1.2×10^{-3}	1.7×10^{-5}	2.1×10^{-4}	5.6×10^{-11}
52	13.7	0.95	0.53	3.5×10^{-1}	2.9×10^{-3}	1.6×10^{-5}	5.2×10^{-4}	5.0×10^{-11}
53	14.8	0.47	0.23	8.6×10^{-2}	1.2×10^{-3}	1.9×10^{-5}	1.8×10^{-4}	7.0×10^{-11}
54	16.6	1.88	0.75	5.6	4.1×10^{-3}	8.0×10^{-6}	2.1×10^{-3}	1.3×10^{-11}
55	17.7	2.38	1.91	9.0	1.0×10^{-2}	9.1×10^{-6}	4.4×10^{-3}	1.7×10^{-11}
56	17.8	3.35	3.35	$1.8 \times 10^{+1}$	1.8×10^{-2}	8.8×10^{-6}	8.1×10^{-3}	1.5×10^{-11}
69	20.8	3.64	10.56	$2.1 \times 10^{+1}$	5.7×10^{-2}	1.2×10^{-5}	1.7×10^{-2}	2.7×10^{-11}
70	23.0	5.45	20.38	$4.7 \times 10^{+1}$	1.1×10^{-1}	1.1×10^{-5}	3.4×10^{-2}	2.5×10^{-11}
71	25.9	7.06	28.96	$7.9 \times 10^{+1}$	1.6×10^{-1}	1.1×10^{-5}	5.2×10^{-2}	2.3×10^{-11}
72	32.2	11.73	43.02	$2.2 \times 10^{+2}$	2.3×10^{-1}	8.9×10^{-6}	1.0×10^{-1}	1.6×10^{-11}
73	37.9	6.12	18.75	$5.9 \times 10^{+1}$	1.0×10^{-1}	1.0×10^{-5}	3.6×10^{-2}	2.1×10^{-11}
74	40.6	5.41	16.37	$4.7 \times 10^{+1}$	8.9×10^{-2}	1.1×10^{-5}	3.0×10^{-2}	2.2×10^{-11}
75	47.6	4.78	9.50	$3.6 \times 10^{+1}$	5.2×10^{-2}	9.7×10^{-6}	2.0×10^{-2}	1.9×10^{-11}
76	55.9	5.83	9.00	$5.4 \times 10^{+1}$	4.9×10^{-2}	8.5×10^{-6}	2.3×10^{-2}	1.4×10^{-11}
77	62.4	6.02	6.99	$5.8 \times 10^{+1}$	3.8×10^{-2}	7.8×10^{-6}	2.0×10^{-2}	1.2×10^{-11}
78	73.7	8.54	12.98	$1.2 \times 10^{+2}$	7.1×10^{-2}	7.6×10^{-6}	3.9×10^{-2}	1.1×10^{-11}
79	79.4	8.01	12.93	$1.0 \times 10^{+2}$	7.0×10^{-2}	7.9×10^{-6}	3.7×10^{-2}	1.2×10^{-11}
80	86.7	8.74	17.70	$1.2 \times 10^{+2}$	9.6×10^{-2}	8.2×10^{-6}	4.8×10^{-2}	1.3×10^{-11}
81	90.7	9.60	16.77	$1.5 \times 10^{+2}$	9.1×10^{-2}	7.6×10^{-6}	5.0×10^{-2}	1.2×10^{-11}
82	100.5	10.82	13.91	$1.9 \times 10^{+2}$	7.6×10^{-2}	6.8×10^{-6}	5.0×10^{-2}	9.1×10^{-12}
83	111.8	10.62	23.20	$5.4 \times 10^{+2}$	1.3×10^{-1}	5.8×10^{-6}	1.1×10^{-1}	6.6×10^{-12}
84	118.3	9.54	17.37	$4.3 \times 10^{+2}$	9.4×10^{-2}	5.7×10^{-6}	8.1×10^{-2}	6.4×10^{-12}
85	124.0	8.26	13.56	$3.3 \times 10^{+2}$	7.4×10^{-2}	5.7×10^{-6}	6.2×10^{-2}	6.5×10^{-12}
86	135.3	11.49	20.17	$6.3 \times 10^{+2}$	1.1×10^{-1}	5.3×10^{-6}	1.0×10^{-1}	5.6×10^{-12}
87	145.0	16.38	32.21	$1.3 \times 10^{+3}$	1.8×10^{-1}	5.0×10^{-6}	1.8×10^{-1}	4.9×10^{-12}
88	153.9	20.18	38.20	$1.9 \times 10^{+3}$	2.1×10^{-1}	4.6×10^{-6}	2.4×10^{-1}	4.2×10^{-12}
89	162.0	21.36	43.85	$2.2 \times 10^{+3}$	2.4×10^{-1}	4.7×10^{-6}	2.8×10^{-1}	4.3×10^{-12}
90	171.8	19.78	34.58	$1.9 \times 10^{+3}$	1.9×10^{-1}	4.5×10^{-6}	2.2×10^{-1}	4.1×10^{-12}
91	183.9	14.16	12.38	$9.6 \times 10^{+2}$	6.7×10^{-2}	4.1×10^{-6}	9.4×10^{-2}	3.3×10^{-12}
92	188.0	14.71	11.87	$1.0 \times 10^{+3}$	6.5×10^{-2}	4.0×10^{-6}	9.5×10^{-2}	3.1×10^{-12}
93	195.3	12.95	9.77	$8.0 \times 10^{+2}$	5.3×10^{-2}	4.0×10^{-6}	7.6×10^{-2}	3.2×10^{-12}

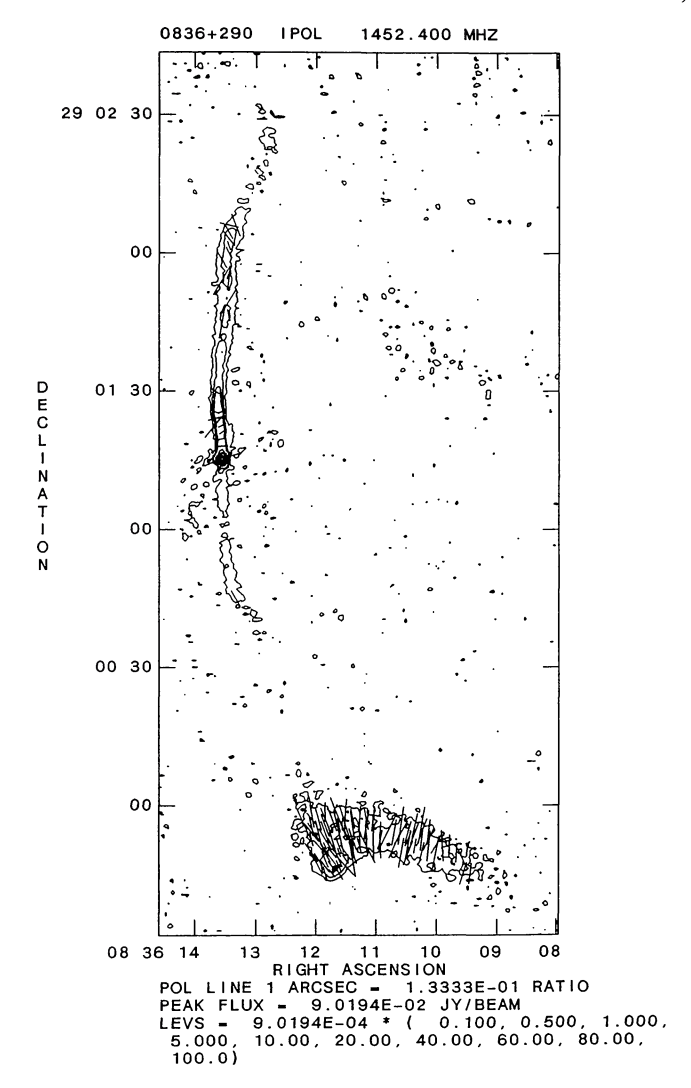


Fig. 17.—Polarization angles for 0836+290, uncorrected for Faraday rotation. Contours are those of the full resolution 20 cm image, and lengths of the vectors are proportional to the fractional polarization at 6 cm.

area, and patches in the second broadening and narrowing are obvious. In the southern hot spot, some beam depolarization is observed between the twin jet areas. Beam depolarization occurs when regions of perpendicular polarization angles are mixed within a beam where they are averaged together. This yields artificially low values for the polarized flux density. The phenomenon gives rise to narrow, sinuous paths of low polarized flux density. It is positively identified by looking at the orientation of the polarization vectors on each side of the path to see if they are close to perpendicular.

The fractional polarization images at 20 and 6 cm are shown in the lower left and right corners of Figure 30, respectively. At 6 cm, the source is mostly less than 40% polarized, with the edges and the ends more polarized. The polarization vectors at 6 cm are shown in Figure 31. At 20 cm, the source is mostly less than 30% polarized with the northern

lobe mostly less than 10%. The filaments are obvious on the fractional polarization but are quite patchy, ranging from 30% to 50% in no particular pattern. The lobe of the southern tail is mostly 5% to 15% polarized. At the second broadening, the polarization suddenly jumps to 20% and increases to 40% at the end.

iii) Spectral Index and Minimum Pressure Analysis

As shown in the top right of Figure 30, both the northern and southern jets appear in the spectral index image at full resolution, although the southern "jet" is only a slight spur on the lobe. The northern jet actually flattens from -0.6 to -0.5away from the core. The southern jet is around -0.5. In the northern lobe, the jet's northern arc has the flattest spectral index of about -0.5, with the rest of the lobe near the arc having α 's of -0.7 to -0.8. Past this area, the lobe steepens to values around -1.0. With the filaments lost in the noise at 6 cm, only a few pixels in the filament area were not blanked by the 3 σ clip. A limit to the spectral index, taking the filament flux density at 6 cm as the rms noise (0.04 mJy per beam) and the 20 cm flux density as 0.2 mJy per beam, yields a value of -1.33. The spectral index, then, must be steeper than this. The positions of the slice centers are shown in Figure 32, and the spectral index from these slices in shown in Figure 33.

The two "jets" in the southern lobe are not obvious in spectral index. However, the area between where they lie on the total intensity image is slightly steeper. The values in the lobe range from -0.4 to -0.6. A rather sudden steepening of the spectral index occurs at the point where the flow recollimates. Just at the edge of the lobe surrounding the hot spot, α steepens from about -0.6 to -0.7. It then steepens gradually to the end of the tail where it approaches -1.0.

The results of the minimum pressure analysis are listed in Tables 13 and 14 and shown in Figure 34.

f) 1231+674

Another small source, 1231+674 is a prototype for the definition of the rapid jet expansions into lobes at symmetric distances from the core. This source was used by Norman et al. (1988) to illustrate such disruption, and it was among those included in the original definition of the WAT class. The remarkable features in this source are the nondisrupting bends of the southern jet and the pronounced "flattening" of the tails at the ends (similar to that in 0043+201), as though they encounter some barrier.

Abell cluster 1559 is classified a Bautz-Morgan type I by McHardy (1974). The central galaxy is cited by Hoessel and Schneider (1985) in a discussion of multiple nuclei. Radio data in the literature include presentations by Ghigo and Owen (1973) (365 MHz), Owen (1975b) (2695 MHz), Owen and Rudnick (1976), who include it in the original six WATs defining the class, Rudnick and Owen (1977) (2695 and 8085 MHz), Fomalont and Bridle (1978), and Simon (1978) (408 MHz).

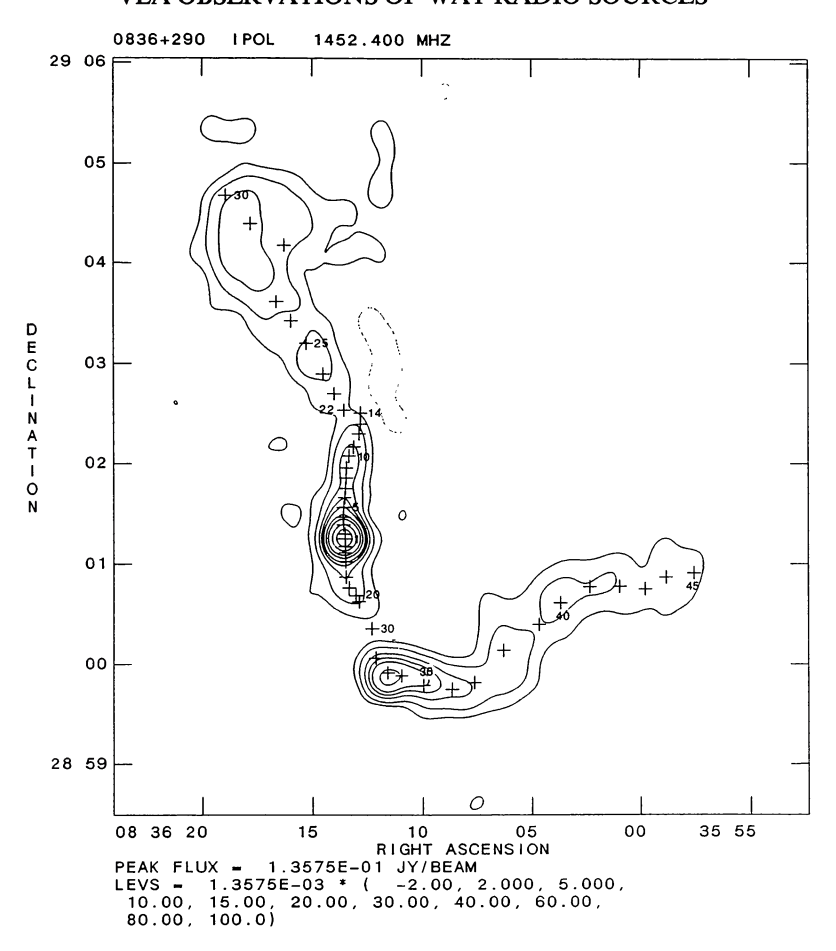


FIG. 18.—Positions of the centers of slices taken perpendicular to the jets and tails of 0836+290, on a low-resolution contour plot. Spectral indices and minimum pressure values for these slices are shown in Figs. 19 and 20.

i) Source Structure

The high-resolution image at 20 cm is shown in Figure 35 (Plate 59). Again, the source contains many striking features. The radio contours overlaid on the optical galaxy image are shown in Figure 36 (Plate 60). The low-resolution image at 20 cm, displayed in Figure 37 (Plate 61), shows the flattening at the ends. The shape of the flattening appears to correspond to the shape of the isophotes of the optical galaxy.

In this source, a most remarkable feature is apparent at both frequencies in the southern tail. A very thin (unresolved) arc forms perpendicular to the tail and arcs to the east and south. This feature is seen in polarization images as well.

ii) Polarization

At 20 cm, little polarized flux is evident above the noise. Most of the source is less than 20% polarized. Most of the northern lobe is less than 10% polarized. The southern jet is not seen except for the kinks which are up to 20% polarized.

At 6 cm, more of the source is seen in polarized emission. The northern jet as it enters the lobe is $\sim 30\%$ polarized, but drops to less than 10% in the region where it broadens. The lobe itself then increases to 60%, and the flattening ridge

stands out clearly from the 3 σ blanking. The southern jet is again polarized at the kinks, having values from 20% to 30%. In the center of the broadest region of this tail, the area of the jet disruption and deflection, the fractional polarization falls to between 10% and 20%. It then increases again to high values greater than 60% at the end.

The polarization vectors at 6 cm are shown in Figure 38.

iii) Spectral Index and Minimum Pressure Analysis

The spectral index was determined at the slices shown in Figure 39; the results are shown in Figure 40. The northern jet has mixed values between -0.4 and -0.8, the southern between -0.6 and -1.0. In the lobes, the values start at around -0.7 and steepen smoothly to -1.5 at the ends. There is also steepening from the west to the east across both tails. The southern arc does not appear until the data has been tapered to a 2" resolution. Then two distinct knots appear. The northern knot shows a steeper spectral index than the second, but low signal to noise makes the values quite uncertain.

The results of the minimum pressure analysis are given in Tables 15 and 16 and is shown in Figure 41.



Fig. 35.—High-resolution (1") image of 1231+674 at 20 cm

O'DONOGHUE, OWEN, AND EILEK (see 72, 93)

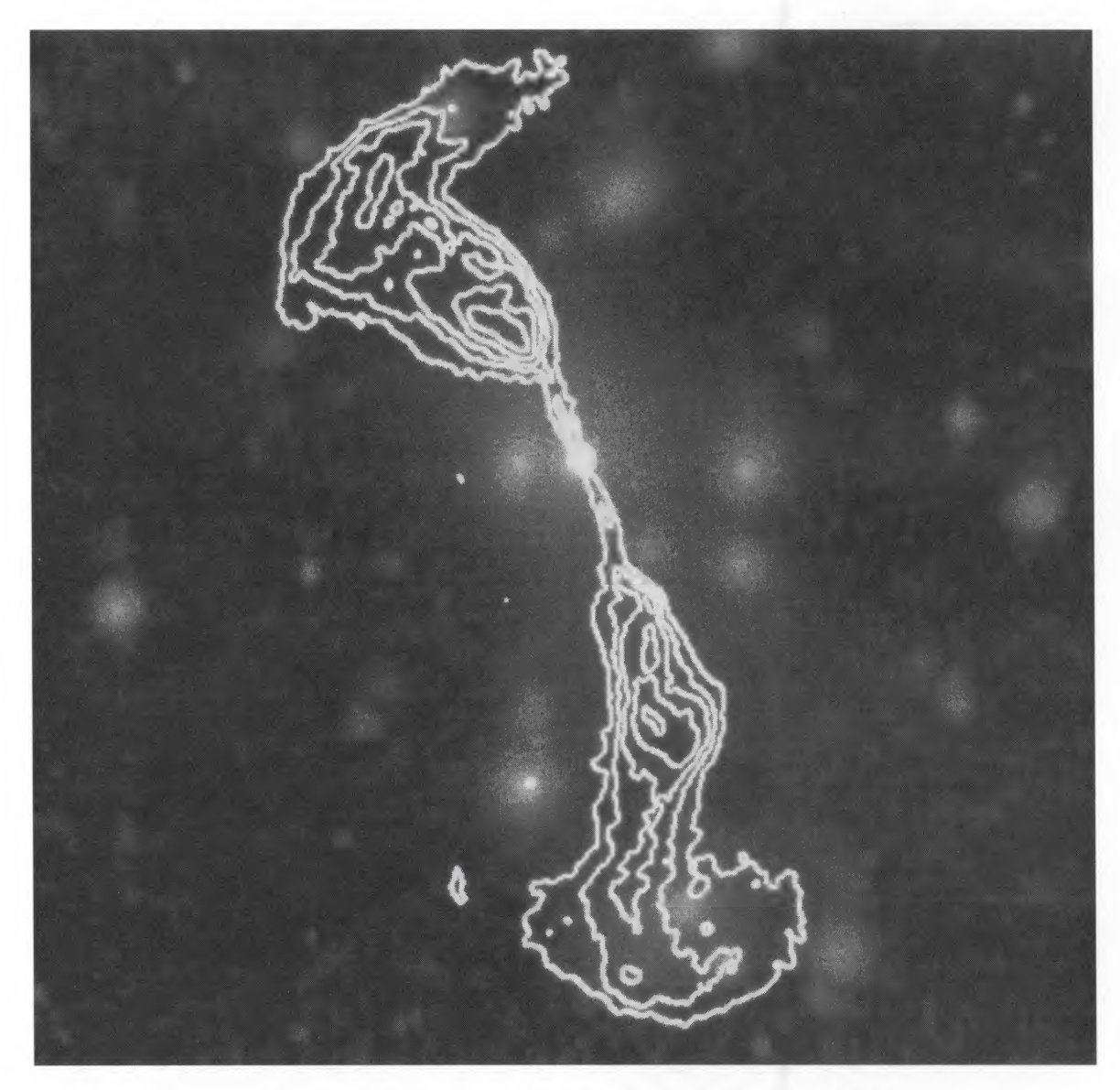


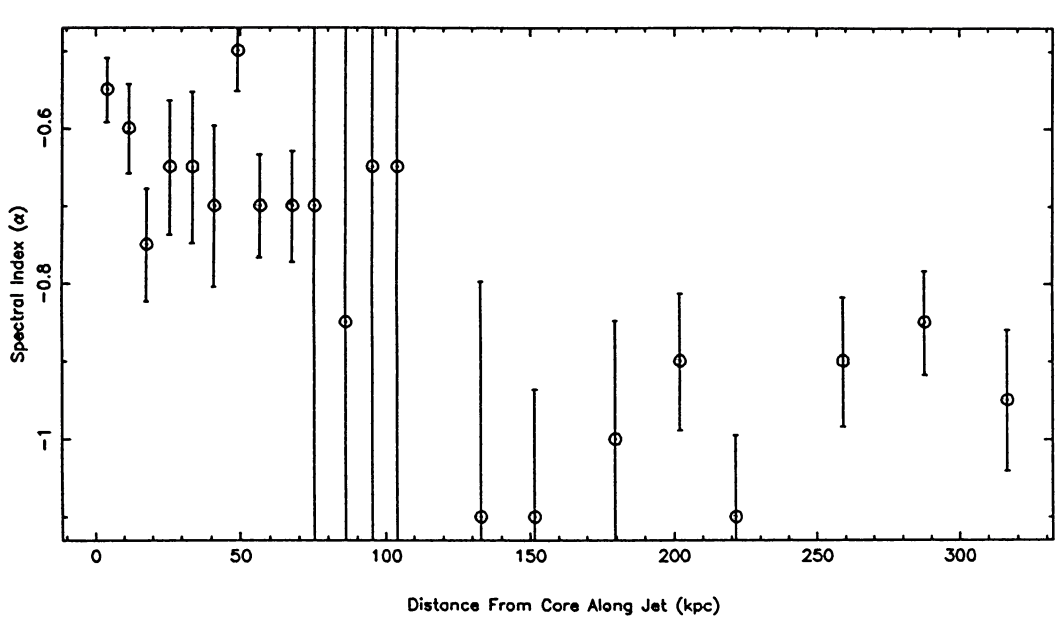
Fig. 36.—20 cm contours of 1231+674 overlaid on the optical galaxy image

O'DONOGHUE, OWEN, AND EILEK (see 72, 93)



FIG. 37.—Low-resolution (13") 20 cm image of 1231+674, showing the flattening at the ends of the tails and the apparent "breakthrough" of some material.

O'Donoghue, Owen, and Eilek (see 72, 93)



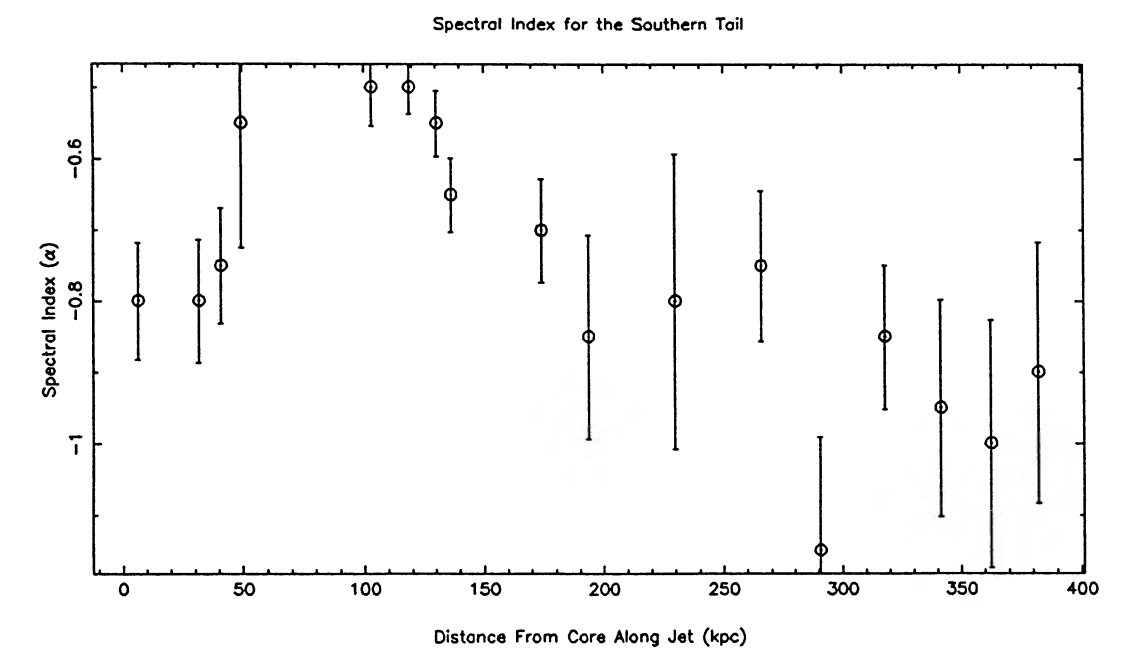


Fig. 19.—Spectral index values between 6 and 20 cm for 0836+290. Values were determined using estimated mean values from slices taken across the total intensity maps, at positions shown in Fig. 18.

g) 1306+107

This source exhibits the single most prominent filament in the survey. At low resolution, the most noteworthy feature is a spur at the end of the northern tail that extends perpendicular to the rest of the tail, completely unmatched in the southern tail. It is also accompanied by a second source within the extent of the tails and a third, that turns out to be a background classical double, to the south.

McHardy (1974) classifies Abell 1684 as a Bautz-Morgan type II cluster. This cluster is also included by Owen (1975a) in a study of the 1400 MHz luminosity function for Abell clusters. Discussions of radio data include Ghigo and Owen (1973) (365 MHz), Owen (1974a) (1400 MHz) and Owen

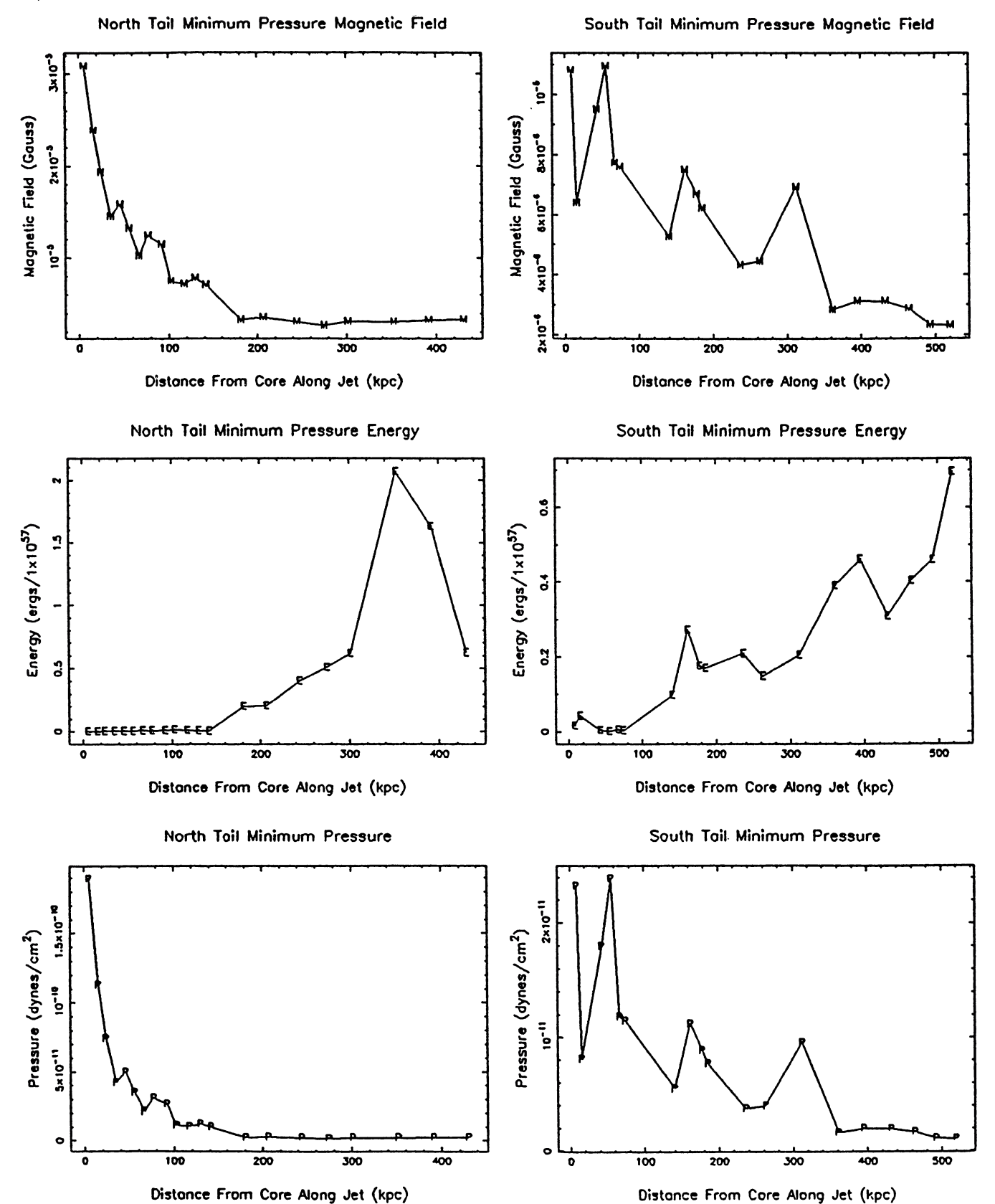


FIG. 20.—Estimates of the magnetic field, total energy (within one slice across the tail), and pressure, derived from minimum pressure arguments, for the north and south tails of 0836+290. Values are given for slice positions shown in Fig. 18. Data are given in Tables 9 and 10.

96

O'DONOGHUE, OWEN, AND EILEK

TABLE 9 0836+290 Northern Tail Minimum Pressure

Number	Distance (kpc)	Diameter (kpc)	S per Beam (mJy per beam)	Volume (kpc ³)	Luminosity (10 ⁴¹ ergs s ⁻¹)	H _{min} (G)	$E_{\rm min} \ (10^{57} {\rm ergs})$	P_{\min} (dyne cm ⁻²)
2	4.1	0.68	2.06	2.9×10^{-1}	4.5×10^{-2}	3.1×10^{-5}	1.6×10^{-3}	1.9×10^{-10}
3	11.7	1.03	1.90	6.7×10^{-1}	4.2×10^{-2}	2.4×10^{-5}	2.2×10^{-3}	1.1×10^{-10}
4	17.8	1.54	2.02	1.5	4.5×10^{-2}	1.9×10^{-5}	3.2×10^{-3}	7.4×10^{-11}
5	25.8	1.91	1.16	2.3	2.6×10^{-2}	1.5×10^{-5}	2.8×10^{-3}	4.2×10^{-11}
6	33.6	1.71	1.24	1.8	2.7×10^{-2}	1.6×10^{-5}	2.7×10^{-3}	5.0×10^{-11}
7	41.1	2.55	1.49	4.1	3.3×10^{-2}	1.3×10^{-5}	4.2×10^{-3}	3.5×10^{-11}
8	49.1	3.22	1.95	$1.3 \times 10^{+1}$	4.3×10^{-2}	1.0×10^{-5}	8.0×10^{-3}	2.1×10^{-11}
9	56.7	2.55	2.37	8.2	5.3×10^{-2}	1.2×10^{-5}	7.4×10^{-3}	3.1×10^{-11}
10	67.7	2.95	2.41	$1.1 \times 10^{+1}$	5.3×10^{-2}	1.1×10^{-5}	8.4×10^{-3}	2.6×10^{-11}
11	75.3	4.35	1.99	$4.0 \times 10^{+1}$	4.4×10^{-2}	7.5×10^{-6}	1.3×10^{-2}	1.1×10^{-11}
12	86.1	3.97	1.45	$3.4 \times 10^{+1}$	3.2×10^{-2}	7.2×10^{-6}	1.0×10^{-2}	1.0×10^{-11}
13	95.3	3.13	1.20	$2.1 \times 10^{+1}$	2.7×10^{-2}	7.8×10^{-6}	7.5×10^{-3}	1.2×10^{-11}
14	104.0	2.40	0.51	$1.2 \times 10^{+1}$	1.1×10^{-2}	7.1×10^{-6}	3.6×10^{-3}	1.0×10^{-11}
23	133.0	19.17	8.79	$3.1 \times 10^{+3}$	1.9×10^{-1}	3.3×10^{-6}	2.0×10^{-1}	2.2×10^{-12}
24	151.6	17.95	10.13	$2.7 \times 10^{+3}$	2.2×10^{-1}	3.6×10^{-6}	2.0×10^{-1}	2.5×10^{-12}
25	179.6	29.07	15.96	$7.2 \times 10^{+3}$	3.5×10^{-1}	3.0×10^{-6}	4.0×10^{-1}	1.9×10^{-12}
26		37.67	16.19	$1.2 \times 10^{+4}$	3.6×10^{-1}	2.7×10^{-6}	5.0×10^{-1}	1.4×10^{-12}
27		35.55	25.06	$1.1 \times 10^{+4}$	5.5×10^{-1}	3.1×10^{-6}	6.2×10^{-1}	1.9×10^{-12}
28		65.80	82.61	$3.7 \times 10^{+4}$	1.8	3.1×10^{-6}	2.1	1.9×10^{-12}
29	287.8	55.54	70.23	2.6×10 ⁺⁴	1.6	3.3×10^{-6}	1.6	2.1×10^{-12}
30	316.5	33.67	27.75	$9.7 \times 10^{+3}$	6.1×10^{-1}	3.3×10^{-6}	6.2×10^{-1}	2.2×10^{-12}

 ${\bf TABLE~10} \\ {\bf 0836+290~Southern~Tail~Minimum~Pressure}$

Number	Distance (kpc)	Diameter (kpc)	S per Beam (mJy per beam)	Volume (kpc³)	Luminosity (10 ⁴¹ ergs s ⁻¹)	H _{min} (G)	E_{\min} (10 ⁵⁷ ergs)	P_{\min} (dyne cm ⁻²)
15	6.1	3.31	4.18	2.3×10 ⁺¹	9.3×10^{-2}	1.1×10^{-5}	1.6×10^{-2}	2.3×10^{-11}
16	11.4	9.14	5.03	$1.8 \times 10^{+2}$	1.1×10^{-1}	6.4×10^{-6}	4.2×10^{-2}	8.1×10^{-12}
18	31.5	2.51	0.90	7.9	2.0×10^{-2}	9.5×10^{-6}	4.2×10^{-3}	1.8×10^{-11}
19	40.7	1.63	0.31	1.7	7.0×10^{-3}	1.1×10^{-5}	1.2×10^{-3}	2.4×10^{-11}
20	49.2	3.44	0.81	$1.5 \times 10^{+1}$	1.8×10^{-2}	7.7×10^{-6}	5.2×10^{-3}	1.2×10^{-11}
21	54.5	2.61	0.44	8.6	9.8×10^{-3}	7.6×10^{-6}	2.9×10^{-3}	1.1×10^{-11}
32	103.1	11.93	8.71	$6.1 \times 10^{+2}$	1.9×10^{-1}	5.3×10^{-6}	9.3×10^{-2}	5.5×10^{-12}
33	118.8	13.90	40.91	$8.3 \times 10^{+2}$	9.1×10^{-1}	7.5×10^{-6}	2.7×10^{-1}	1.1×10^{-11}
34	130.4	12.57	22.31	$6.7 \times 10^{+2}$	4.9×10^{-1}	6.7×10^{-6}	1.8×10^{-1}	8.9×10^{-12}
35	136.2	13.28	19.32	$7.5 \times 10^{+2}$	4.3×10^{-1}	6.2×10^{-6}	1.7×10^{-1}	7.7×10^{-12}
36	173.9	21.13	13.75	1.9×10 ⁺³	3.0×10^{-1}	4.3×10^{-6}	2.1×10^{-1}	3.7×10^{-12}
37	193.5	17.26	10.21	$1.3 \times 10^{+3}$	2.3×10^{-1}	4.5×10^{-6}	1.5×10^{-1}	4.0×10^{-12}
38	229.8	9.23	27.33	$7.3 \times 10^{+2}$	6.1×10^{-1}	6.9×10^{-6}	2.0×10^{-1}	9.5×10^{-12}
39	265.7	31.07	13.77	$8.2 \times 10^{+3}$	3.0×10^{-1}	2.8×10^{-6}	3.9×10^{-1}	1.6×10^{-12}
40	290.7	30.66	18.82	$8.0 \times 10^{+3}$	4.2×10^{-1}	3.1×10^{-6}	4.6×10^{-1}	2.0×10^{-12}
41	317.9	25.12	12.54	5.4×10 ⁺³	2.8×10^{-1}	3.1×10^{-6}	3.1×10^{-1}	1.9×10^{-12}
42	341.4	31.25	14.50	$8.3 \times 10^{+3}$	3.2×10^{-1}	2.9×10^{-6}	4.0×10^{-1}	1.6×10^{-12}
43	362.5	41.09	12.11	$1.4 \times 10^{+4}$	2.7×10^{-1}	2.3×10^{-6}	4.6×10^{-1}	1.1×10^{-12}
44		51.15	17.98	$2.2 \times 10^{+4}$	4.0×10^{-1}	2.3×10^{-6}	7.0×10^{-1}	1.1×10^{-12}

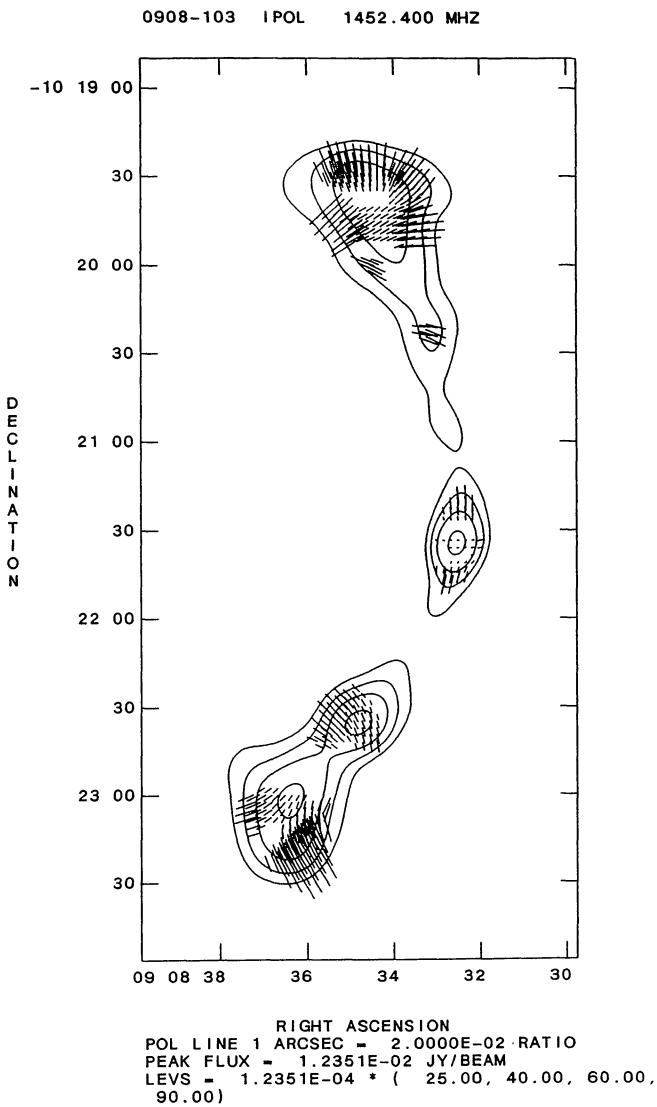


FIG. 24.—Polarization angles of 0908–103, uncorrected for Faraday rotation. Contours are those of the full resolution 20 cm image, and lengths of the vectors are proportional to the fractional polarization at 6 cm.

(1975b) (2695 MHz), Simon (1978) (408 MHz), and Valentijn (1979a, b).

i) Source Structure

The high-resolution image at 20 cm is shown in Figure 42 (Plate 62), and the radio contours overlaid on the optical image are shown in Figure 43 (Plate 63). The feature that is immediately noticeable in the high-resolution image is the bright filament, or pair of filaments in the northern tail.

ii) Polarization

At full resolution at 20 cm, far more polarized flux density stands out above the noise than in any other of the survey

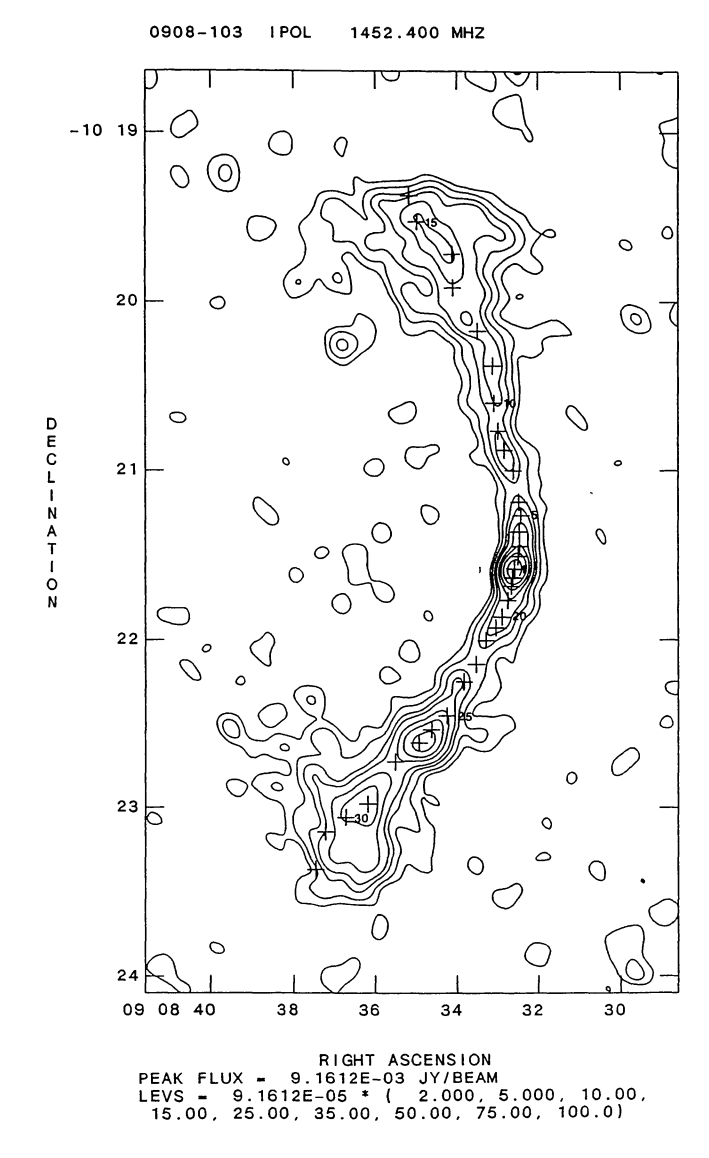


Fig. 25.—Positions of the centers of slices taken perpendicular to the jets and tails of 0908–103, on a low-resolution contour plot. Spectral indices and minimum pressure values for these slices are shown in Figs. 26 and 27.

sources. The southern tail is particularly bright in polarized emission, with quite a lot of beam depolarization evident.

The primary filament is quite apparent in fractional polarization, particularly at 6 cm. At 20 cm, the northern tail is less than 20% polarized at the hot spot, increasing toward the end of the tail up to nearly full polarization. The southern tail at this frequency reflects the same range of fractional polarization. At 6 cm, the northern tail exhibits fractional polarization in the hot spot of 10% to 20%, while the primary filament has mottled values between 40% and 80%. The southern tail at 6 cm is initially 10% to 20% polarized, increasing to ~50% at the end. No features are obvious in this tail. The polarization vectors scaled to the 6 cm fractional polarization are shown in Figure 44.

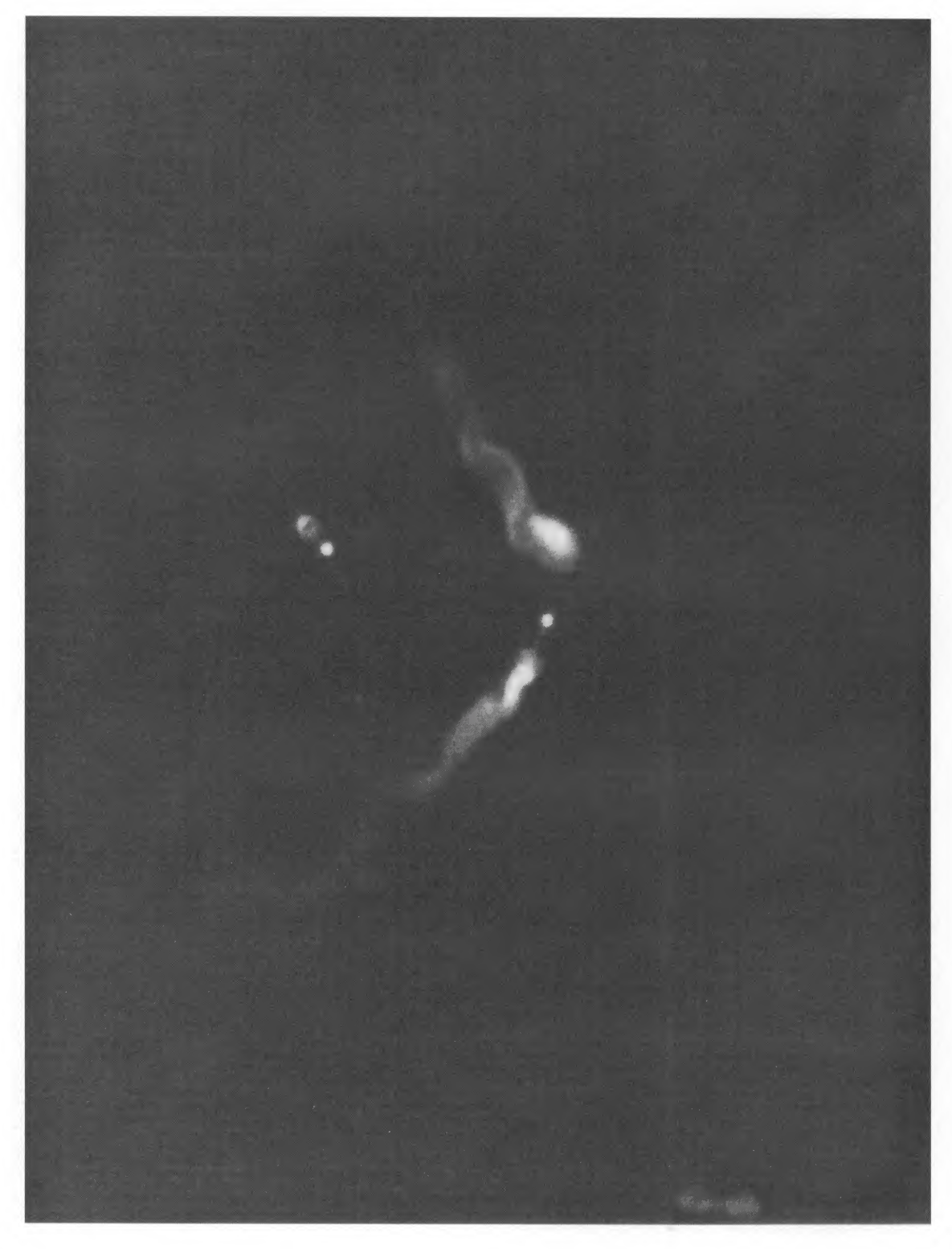


FIG. 42.—High-resolution (1") image of 1306+107 at 20 cm

O'Donoghue, Owen, and Eilek (see 72, 97)

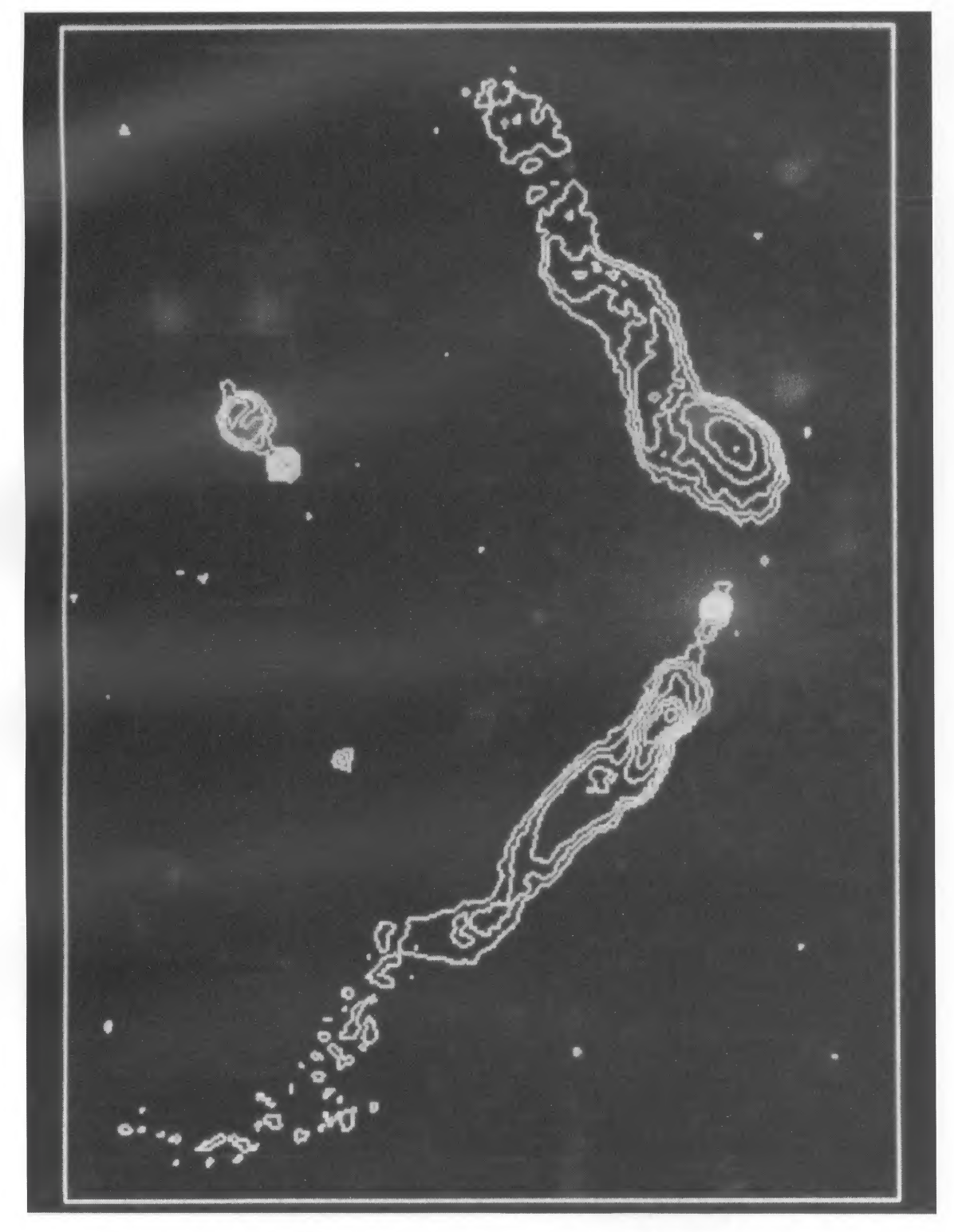
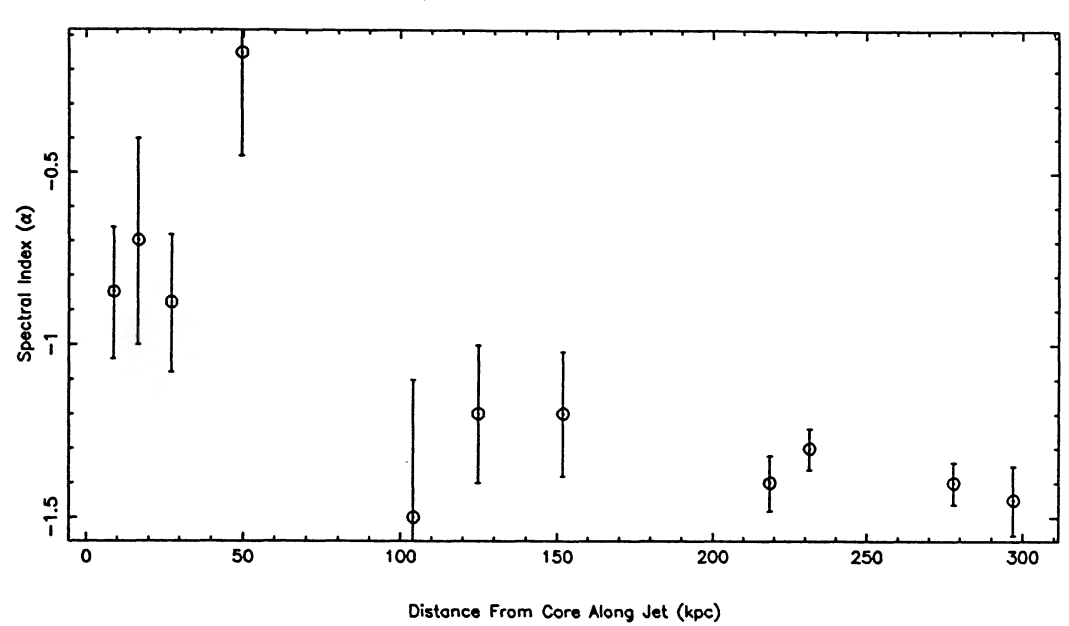


Fig. 43.—20 cm contours of 1306+107 overlaid on the optical galaxy image

O'DONOGHUE, OWEN, AND EILEK (see 72, 97)

98





Spectral Index for the Southern Tail

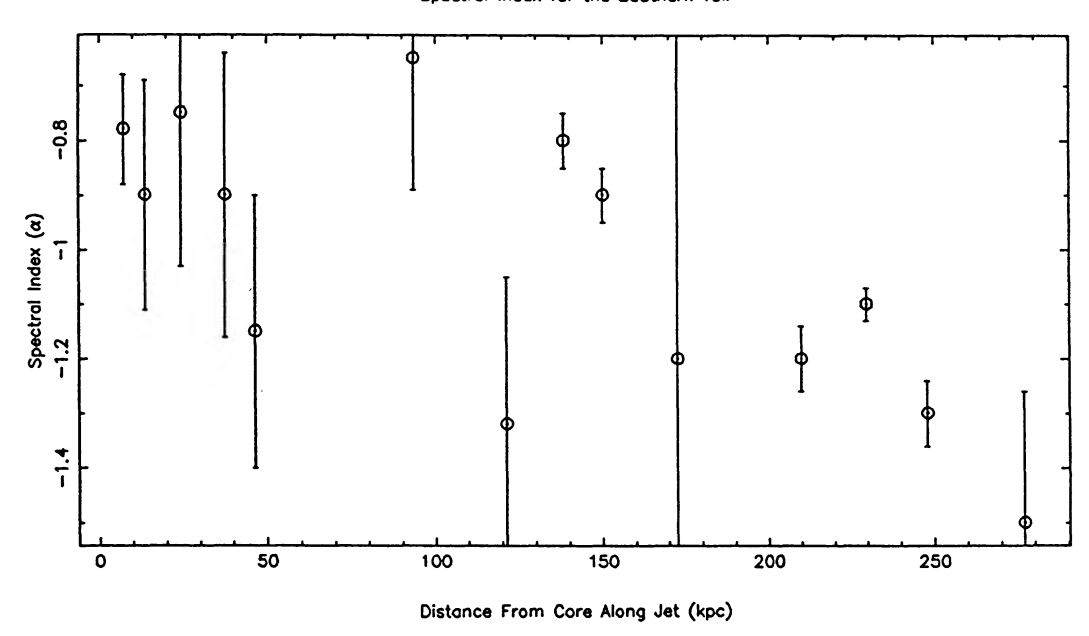


FIG. 26.—Spectral index values between 6 and 20 cm for 0908-103. Values were determined using estimated mean values from slices taken across the total intensity maps, at positions shown in Fig. 25.

iii) Spectral Index and Minimum Pressure Analysis

Because of low surface brightness at 6 cm, the full resolution spectral index image is mottled and lacking detail. However, the primary filament in the northern tail does appear with a spectral index that steepens away from the core. Tapering the data to lower resolution shows steepening trends of the spectral index in both tails. In the northern tail, α steepens away from the hot spot in all directions from -0.5to -0.8 at the northwestern edge and -1.5 at the end of the northern spur. It is notable that the spectral index appears to steepen across the northern spur instead of along it.

The southern tail exhibits no particular features other than a gradual steepening from -0.5 at the core to -1.5 at the end.

1990ApJS...72...750

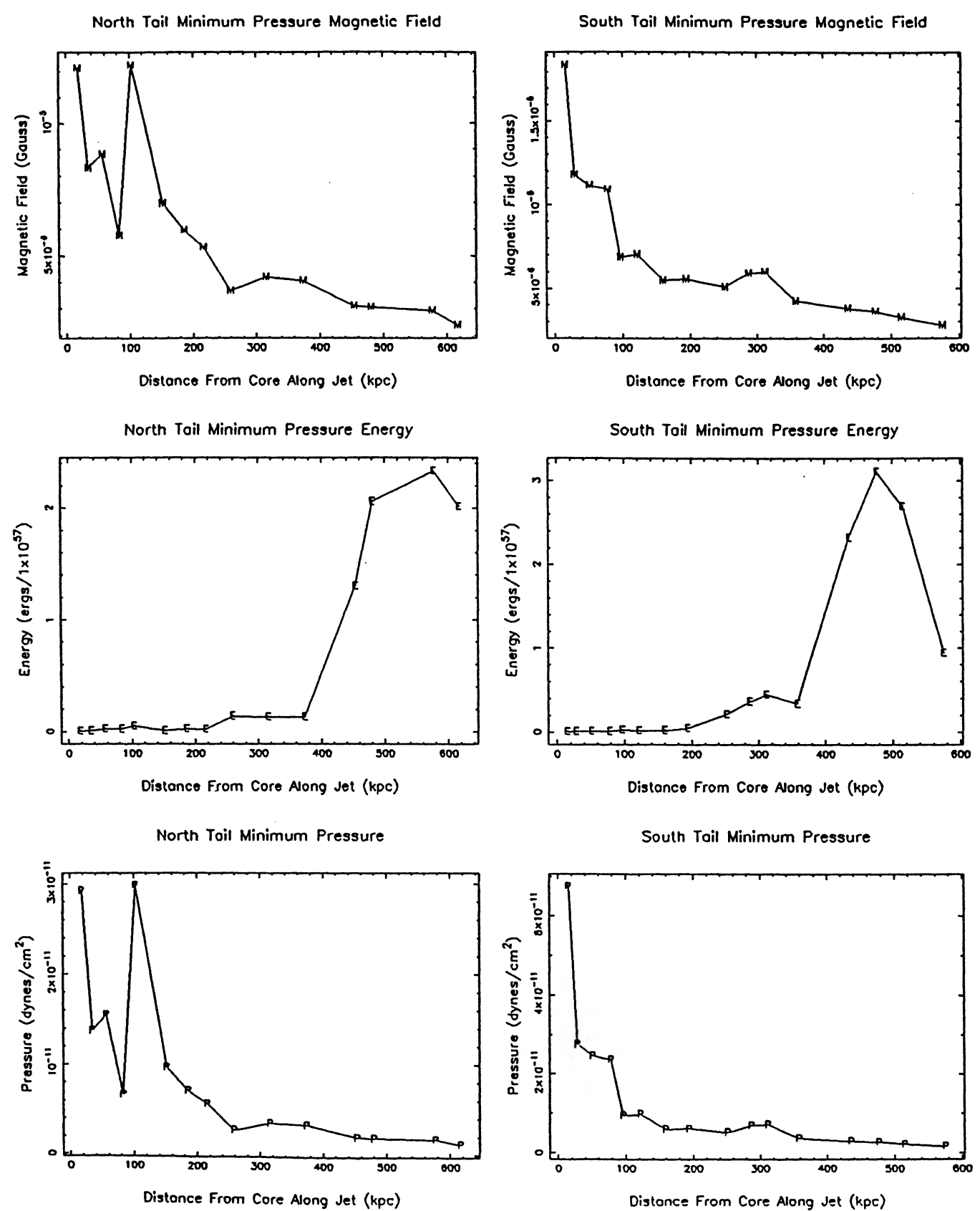


FIG. 27.—Estimates of the magnetic field, total energy (within one slice across the tail), and pressure, derived from minimum pressure arguments, for the north and south tails of 0908–103. Values are given for slice positions shown in Fig. 25. Data are given in Tables 11 and 12.

TABLE 11 0908-103 Northern Tail Minimum Pressure

Number	Distance (kpc)	Diameter (kpc)	S per Beam (mJy per beam)	Volume (kpc³)	Luminosity (10 ⁴¹ ergs s ⁻¹)	H _{min} (G)	$\frac{E_{\min}}{(10^{57}\mathrm{ergs})}$	P_{\min} (dyne cm ⁻²)
2	8.7	1.91	0.46	6.0	2.4×10^{-2}	1.2×10 ⁻⁵	5.1×10^{-3}	2.9×10^{-11}
3	16.6	3.36	0.38	$1.8 \times 10^{+1}$	2.0×10^{-2}	8.3×10^{-6}	7.4×10^{-3}	1.4×10^{-11}
4	27.2	5.69	1.35	$5.3 \times 10^{+1}$	7.1×10^{-2}	8.8×10^{-6}	2.4×10^{-2}	1.5×10^{-11}
5	39.9	8.60	0.69	$1.2 \times 10^{+2}$	3.6×10^{-2}	5.8×10^{-6}	2.3×10^{-2}	6.6×10^{-12}
6	49.4	4.12	4.47	5.5×10 ⁺¹	2.3×10^{-1}	1.2×10^{-5}	4.9×10^{-2}	3.0×10^{-11}
7	72.9	2.78	0.28	$2.5 \times 10^{+1}$	1.5×10^{-2}	7.0×10^{-6}	7.2×10^{-3}	9.7×10^{-12}
8	89.3	5.99	0.76	$1.2 \times 10^{+2}$	4.0×10^{-2}	6.0×10^{-6}	2.4×10^{-2}	7.1×10^{-12}
9	104.0	6.14	0.53	$1.2 \times 10^{+2}$	2.8×10^{-2}	5.3×10^{-6}	2.0×10^{-2}	5.6×10^{-12}
10	124.8	16.28	2.06	$1.7 \times 10^{+3}$	1.1×10^{-1}	3.7×10^{-6}	1.4×10^{-1}	2.7×10^{-12}
11	151.8	13.97	2.39	$1.3 \times 10^{+3}$	1.3×10^{-1}	4.2×10^{-6}	1.3×10^{-1}	3.5×10^{-12}
12	180.0	14.49	2.29	$1.4 \times 10^{+3}$	1.2×10^{-1}	4.0×10^{-6}	1.3×10^{-1}	3.3×10^{-12}
13	218.4	42.17	15.27	$2.3 \times 10^{+4}$	8.0×10^{-1}	3.1×10^{-6}	1.3	1.9×10^{-12}
14	231.3	53.87	23.59	$3.8 \times 10^{+4}$	1.2	3.0×10^{-6}	2.1	1.9×10^{-12}
15	277.8	59.93	24.96	$4.7 \times 10^{+4}$	1.3	2.9×10^{-6}	2.3	1.7×10^{-12}
16	296.9	68.33	15.89	6.1×10 ⁺⁴	8.4×10^{-1}	2.4×10^{-6}	2.0	1.1×10^{-12}

TABLE 12 0908-103 Northern Tail Minimum Pressure

Number	Distance (kpc)	Diameter (kpc)	S per Beam (mJy per beam)	Volume (kpc ³)	Luminosity (10 ⁴¹ ergs s ⁻¹)	H _{min} (G)	E_{\min} (10 ⁵⁷ ergs)	P_{\min} (dyne cm ⁻²)
17	7.3	1.32	0.58	2.8	2.8×10^{-2}	1.8×10 ⁻⁵	5.6×10 ⁻³	6.7×10^{-11}
18	13.7	2.75	0.53	$1.2 \times 10^{+1}$	2.5×10^{-2}	1.2×10^{-5}	9.9×10^{-3}	2.8×10^{-11}
19	24.5	3.02	0.53	$1.5 \times 10^{+1}$	2.5×10^{-2}	1.1×10^{-5}	1.1×10^{-2}	2.5×10^{-11}
20	37.6	2.98	0.48	$1.5 \times 10^{+1}$	2.3×10^{-2}	1.1×10^{-5}	1.0×10^{-2}	2.4×10^{-11}
21	46.5	5.36	0.61	$9.4 \times 10^{+1}$	2.9×10^{-2}	6.9×10^{-6}	2.6×10^{-2}	9.4×10^{-12}
22	58.6	4.36	0.44	$6.2 \times 10^{+1}$	2.1×10^{-2}	7.0×10^{-6}	1.8×10^{-2}	9.8×10^{-12}
23	76.8	6.02	0.35	$1.2 \times 10^{+2}$	1.7×10^{-2}	5.5×10^{-6}	2.1×10^{-2}	6.0×10^{-12}
24	93.4	8.74	0.77	$2.5 \times 10^{+2}$	3.6×10^{-2}	5.5×10^{-6}	4.5×10^{-2}	6.1×10^{-12}
25	121.3	14.64	3.18	$1.4 \times 10^{+3}$	1.5×10^{-1}	5.1×10^{-6}	2.1×10^{-1}	5.1×10^{-12}
26	138.3	16.49	6.79	$1.8 \times 10^{+3}$	3.2×10^{-1}	5.9×10^{-6}	3.6×10^{-1}	6.9×10^{-12}
27	150.1	18.00	8.61	$2.1 \times 10^{+3}$	4.1×10^{-1}	6.0×10^{-6}	4.4×10^{-1}	7.2×10^{-12}
28	172.6	22.08	3.86	$3.2 \times 10^{+3}$	1.8×10^{-1}	4.2×10^{-6}	3.3×10^{-1}	3.6×10^{-12}
29	209.9	46.05	22.65	$2.8 \times 10^{+4}$	1.1	3.8×10^{-6}	2.3	2.9×10^{-12}
30	229.7	55.89	28.12	$4.1 \times 10^{+4}$	1.3	3.6×10^{-6}	3.1	2.6×10^{-12}
31	247.9	57.68	20.89	4.3×10 ⁺⁴	9.9×10^{-1}	3.3×10^{-6}	2.7	2.1×10^{-12}
32	277.0	39.86	5.78	$2.1 \times 10^{+4}$	2.7×10^{-1}	2.8×10^{-6}	9.4×10^{-1}	1.5×10^{-12}

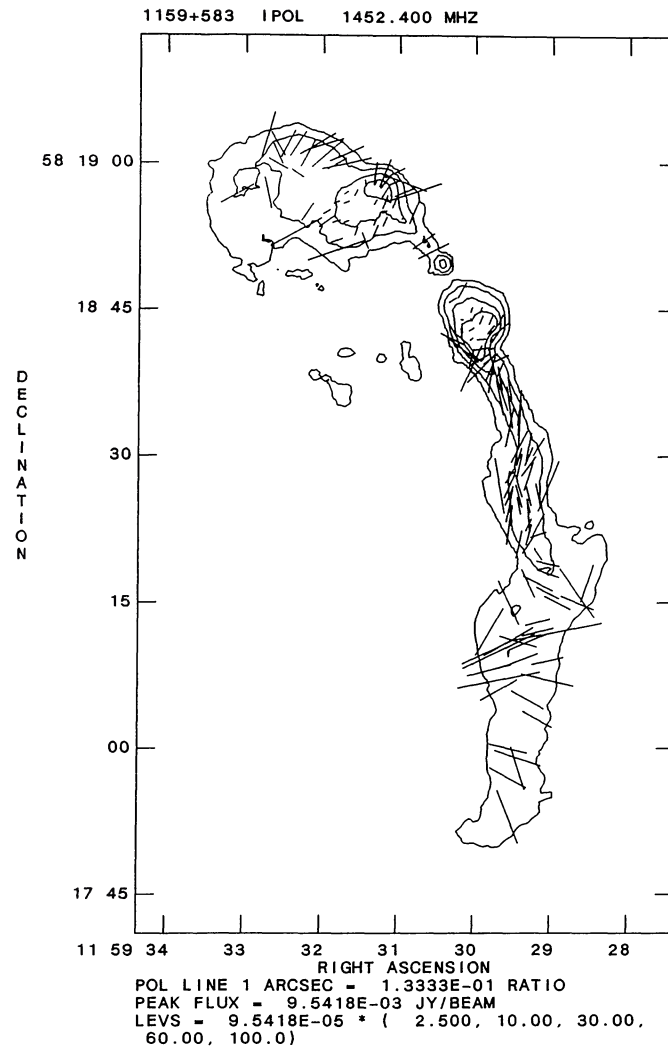


FIG. 31.—Polarization angles for 1159+583, uncorrected for Faraday rotation. Contours are those of the full resolution 20 cm image, and lengths of the vectors are proportional to the fractional polarization at 6 cm.

The spectral index was sampled by cross-tail slices centered at the positions shown in Figure 45. The spectral index values are shown in Figure 46. The results of the minimum pressure analysis are shown in Figure 47 and are presented in Tables 17 and 18.

h) 1433+553

A rather small source, 1433+553, may, like 1159+583, be strongly projected. The appearance of the southern tail suggests this. The northern tail does not seem to be suffering as much projection and may indicate that the tails are not in a plane. The northern jet in this source is unusual in that it appears to be a pair of jets that bifurcate at the source, bend away from each other, and come back toward each other near the lobe. They do not quite rejoin before entering the lobe. This can be seen in the high-resolution 20 cm image presented in Figure 48 (Plate 64).

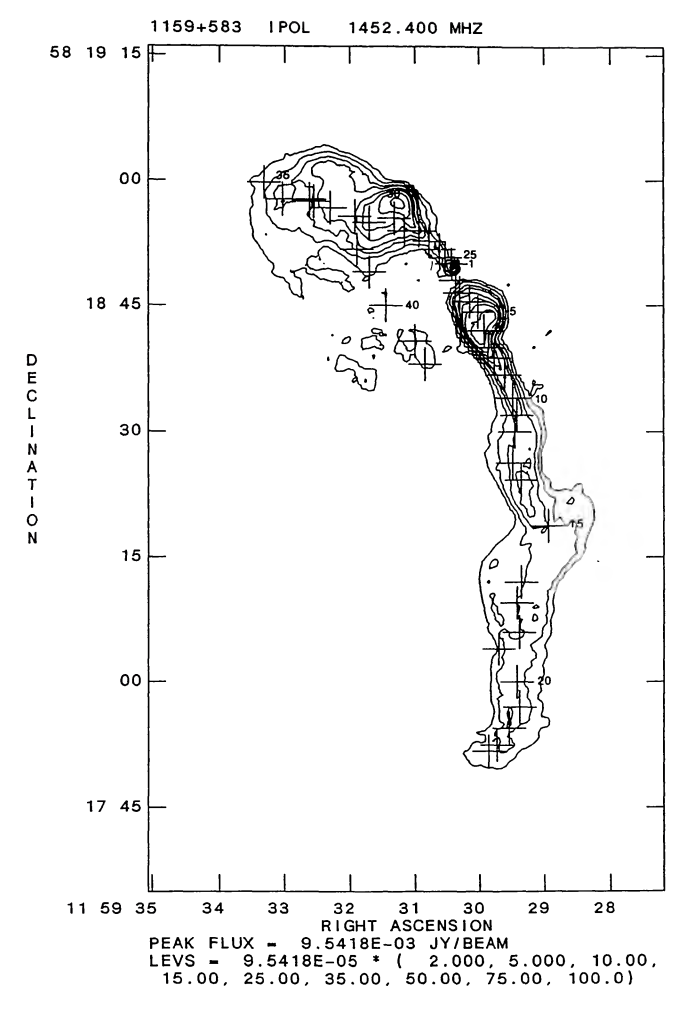


Fig. 32.—Positions of the centers of slices taken perpendicular to the jets and tails of 1159+583, on a low-resolution contour plot. Spectral indices and minimum pressure values for these slices are shown in Figs. 33 and 34.

Both Bautz (1972) and McHardy (1974) classify Abell 1940 as a Bautz-Morgan II clusters. Further studies of the cluster were done by McHardy (1978a, b), who investigated the X-ray properties, and Owen (1975a), who examined the 1400 MHz luminosity function for clusters. The velocity dispersion of the cluster is studied by Yahil and Vidal (1977) and Danese, De Zotti, and diTullio (1980). Radio data are reported by Owen and Rudnick (1976), who include this in the original six WATs defining the class, Rudnick and Owen (1977) (2695 and 8085 MHz), Simon (1978) (408 MHz), Valentijn (1979a, b), and Fanti et al. (1983) (1400 MHz).

i) Source Structure

At 20 cm many details in both tails are revealed, along with the northern "twin" jets. Of these, the southern twin is much straighter and is better defined against the noise. The northern twin actually bows away from the southern and is fainter, having down to 10% of the other's flux density. Between the jets, the flux density is noticeably below the noise level. There

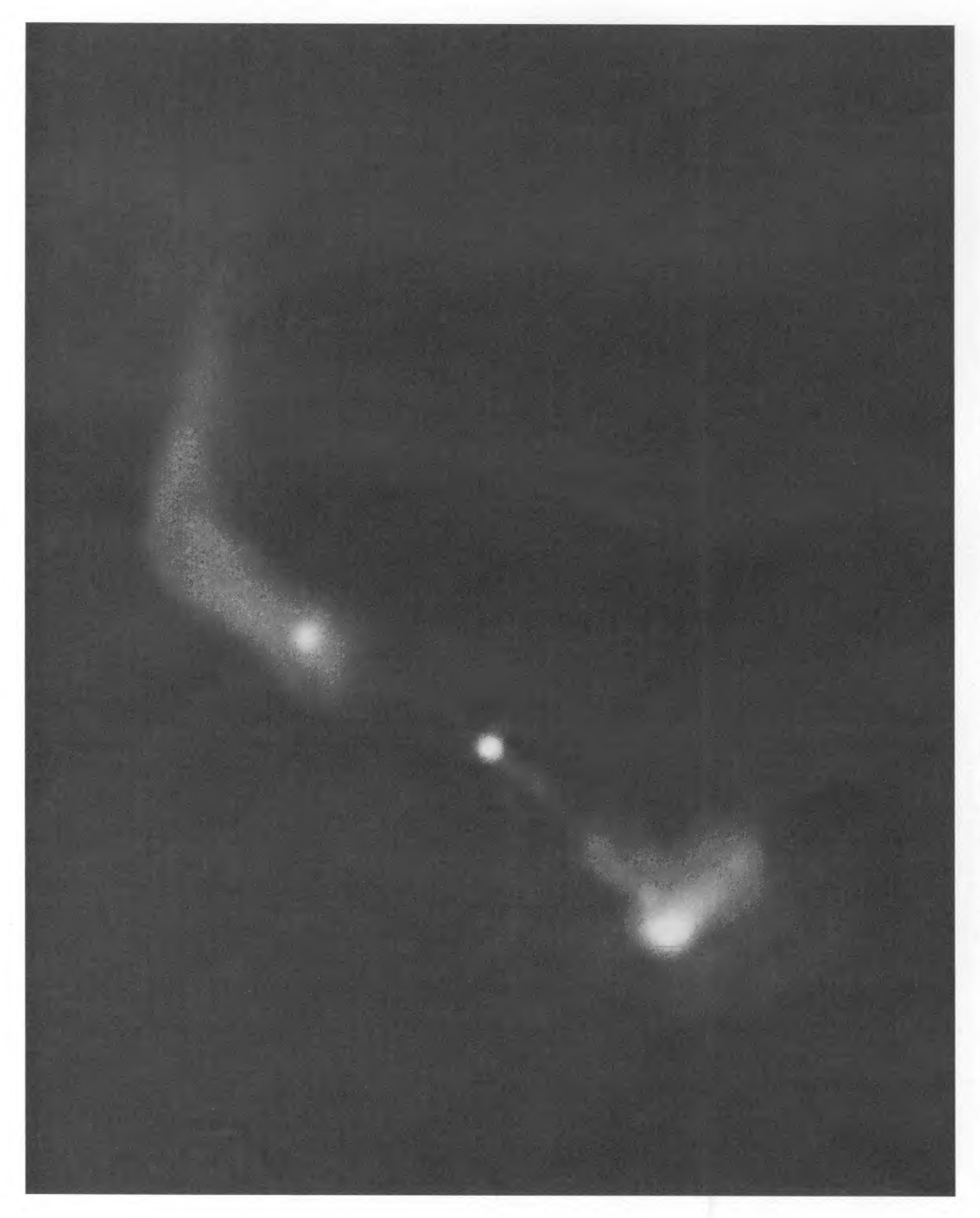
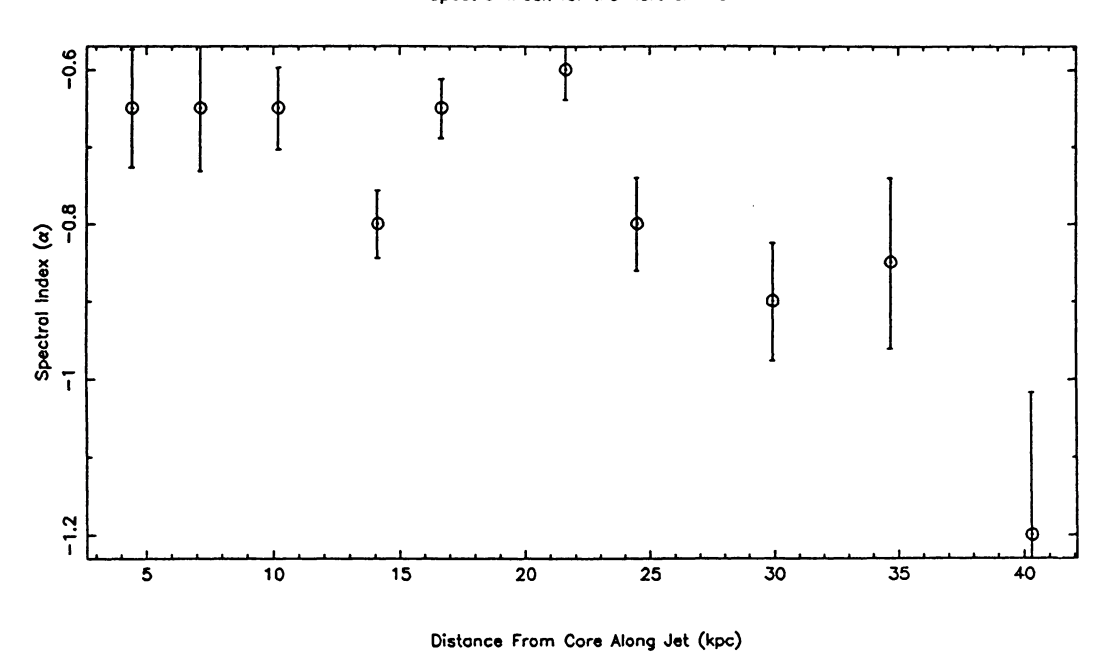
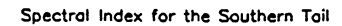


Fig. 48.—High-resolution (1") image of 1433+553 at 20 cm

O'DONOGHUE, OWEN, AND EILEK (see 72, 101)

Spectral Index for the Northern Tail





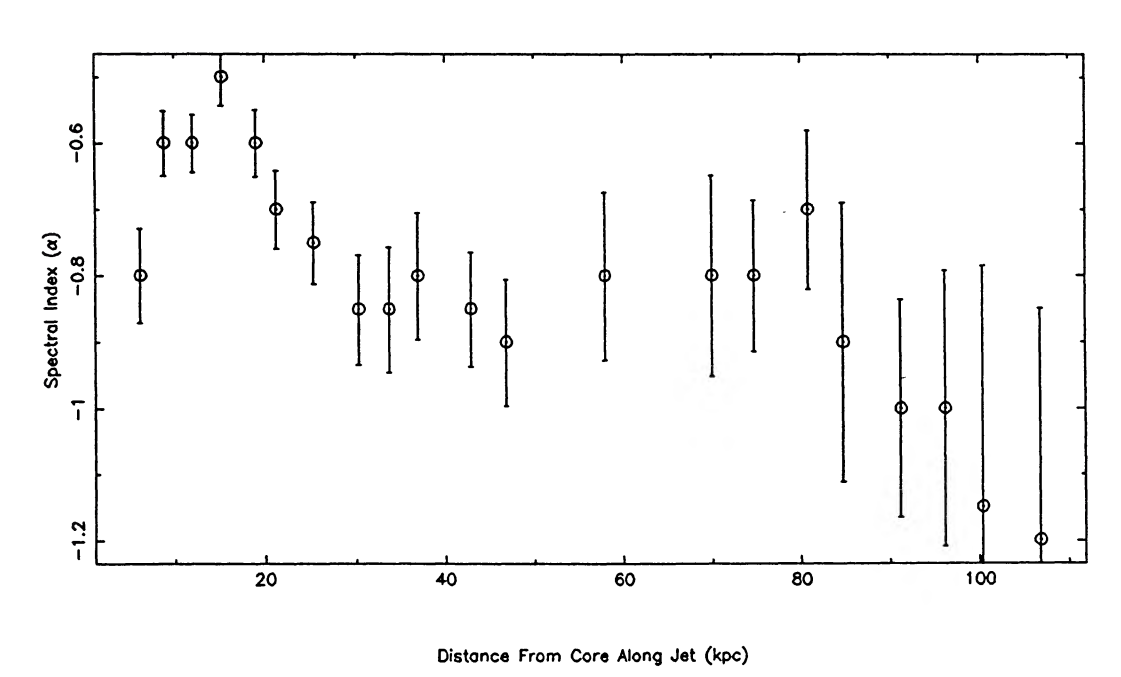


Fig. 33.—Spectral index values between 6 and 20 cm for 1159+583. Values were determined using estimated mean values from slices taken across the total intensity maps, at positions shown in Fig. 32.

No. 1, 1990

TABLE 13 1159+583 Northern Tail Minimum Pressure

Number	Distance (kpc)	Diameter (kpc)	S per Beam (mJy per beam)	Volume (kpc ³)	Luminosity (10 ⁴¹ ergs s ⁻¹)	H_{\min} (G)	$E_{\min} (10^{57} \mathrm{ergs})$	P_{\min} (dyne cm ⁻²)
25	2.2	0.29	0.15	6.0×10^{-2}	5.6×10^{-3}	2.7×10^{-5}	2.5×10^{-4}	1.4×10^{-10}
26	4.4	0.74	0.92	3.7×10^{-1}	3.5×10^{-2}	2.6×10^{-5}	1.5×10^{-3}	1.4×10^{-10}
27	7.1	1.26	1.02	$1.1 \times 10^{+0}$	3.9×10^{-2}	2.0×10^{-5}	2.6×10^{-3}	8.0×10^{-11}
28	10.2	2.13	5.94	$3.1 \times 10^{+0}$	2.3×10^{-1}	2.5×10^{-5}	1.1×10^{-2}	1.2×10^{-10}
29	14.1	3.21	11.56	$7.1 \times 10^{+0}$	4.4×10^{-1}	2.4×10^{-5}	2.3×10^{-2}	1.1×10^{-10}
30	16.7	5.51	40.62	$2.1 \times 10^{+1}$	$1.6 \times 10^{+0}$	2.5×10^{-5}	7.5×10^{-2}	1.2×10^{-10}
31	21.6	10.29	60.02	$7.3 \times 10^{+1}$	$2.3 \times 10^{+0}$	1.9×10^{-5}	1.6×10^{-1}	7.5×10^{-11}
32	24.5	8.24	19.44	$4.7 \times 10^{+1}$	7.5×10^{-1}	1.6×10^{-5}	7.0×10^{-2}	5.1×10^{-11}
33	29.9	11.75	21.66	$9.5 \times 10^{+1}$	8.3×10^{-1}	1.3×10^{-5}	1.0×10^{-1}	3.6×10^{-11}
34	34.7	10.14	14.79	$7.1 \times 10^{+1}$	5.7×10^{-1}	1.3×10^{-5}	7.1×10^{-2}	3.4×10^{-11}
35	40.3	8.17	9.46	$4.6 \times 10^{+1}$	3.6×10^{-1}	1.3×10^{-5}	4.6×10^{-2}	3.4×10^{-11}
36	44.9	9.70	32.05	$6.5 \times 10^{+1}$	$1.2 \times 10^{+0}$	1.7×10^{-5}	1.1×10^{-1}	5.6×10^{-11}

TABLE 14 1159+583 SOUTHERN TAIL MINIMUM PRESSURE

Number	Distance (kpc)	Diameter (kpc)	S per Beam (mJy per beam)	Volume (kpc ³)	Luminosity (10 ⁴¹ ergs s ⁻¹)	H _{min} (G)	E_{\min} (10 ⁵⁷ ergs)	P_{\min} (dyne cm ⁻²)
3	6.1	4.30	5.94	1.3×10 ⁺¹	1.9×10^{-1}	1.8×10^{-5}	2.3×10^{-2}	6.2×10^{-11}
4	8.8	5.13	16.29	$1.8 \times 10^{+1}$	5.1×10^{-1}	2.1×10^{-5}	4.8×10^{-2}	9.1×10^{-11}
5	12.1	5.88	33.79	$2.4 \times 10^{+1}$	$1.1 \times 10^{+0}$	2.4×10^{-5}	8.2×10^{-2}	1.2×10^{-10}
6	15.3	5.58	44 52	$2.1 \times 10^{+1}$	$1.4 \times 10^{+0}$	2.7×10^{-5}	9.2×10^{-2}	1.5×10^{-10}
7		2.22	10.95	$3.4 \times 10^{+0}$	3.4×10^{-1}	3.1×10^{-5}	1.9×10^{-2}	1.9×10^{-10}
8	21.3	2.31	6.43	$3.7 \times 10^{+0}$	2.0×10^{-1}	2.6×10^{-5}	1.4×10^{-2}	1.3×10^{-10}
9		2.04	4.38	$2.9 \times 10^{+0}$	1.4×10^{-1}	2.5×10^{-5}	1.0×10^{-2}	1.2×10^{-10}
10	30.3	1.95	3.85	$2.6 \times 10^{+0}$	1.2×10^{-1}	2.5×10^{-5}	9.2×10^{-3}	1.2×10^{-10}
11	33.7	2.97	3.95	61×10 ⁺⁰	1.2×10^{-1}	1.9×10^{-5}	1.3×10^{-2}	7.5×10^{-11}
12	36.9	5.43	5.82	$2.0 \times 10^{+1}$	1.2×10^{-1}	1.5×10^{-5}	2.8×10^{-2}	4.7×10^{-11}
13		5.95	7.81	$2.0 \times 10^{+1}$	2.5×10^{-1}	1.6×10^{-5}	3.6×10^{-2}	5.0×10^{-11}
14	46.8	5.36	7.86	$2.0 \times 10^{+1}$	2.5×10^{-1}	1.7×10^{-5}	3.3×10^{-2}	5.7×10^{-11}
15		11.45	11.79	$9.0 \times 10^{+1}$	3.7×10^{-1}	1.2×10^{-5}	8.0×10^{-2}	3.0×10^{-11}
16	69.9	12.62	7.36	1 1×10 ⁺²	2.3×10^{-1}	1.0×10^{-5}	6.6×10 ⁻²	2.1×10^{-11}
17		11.60	7.30 5.87	$9.3 \times 10^{+1}$	1.8×10^{-1}	1.0×10^{-5}	5.0×10^{-2}	2.1×10^{-11}
18		10.07	4.84	$7.0 \times 10^{+1}$	1.5×10^{-1}	1.0×10^{-5}	4.3×10^{-2}	2.0×10^{-11} 2.1×10^{-11}
19		7.24	3.85	$3.6 \times 10^{+1}$	1.3×10^{-1}	1.0×10^{-5}	2.8×10^{-2}	2.7×10^{-11}
20		3.32	2.31	$7.6 \times 10^{+0}$	7.3×10^{-2}	1.6×10^{-5}	1.1×10^{-2}	4.9×10^{-11}
0.1	061		417	2210+1	1 2 10 = 1	1.010=5	2010=2	20.410=11
21	96.1	6.84	4.17	$3.2 \times 10^{+1}$	1.3×10^{-1}	1.2×10^{-5}	2.8×10^{-2}	3.0×10^{-11}
22		7.40	3.24	$3.8 \times 10^{+1}$	1.0×10^{-1}	1.1×10^{-5}	2.6×10^{-2}	2.4×10^{-11}
23	104.6	6.77	2.44	$3.2 \times 10^{+1}$	7.7×10^{-2}	1.1×10^{-5}	2.1×10^{-2}	2.2×10^{-11}
24	106.8	12.18	6.48	$1.0 \times 10^{+2}$	2.0×10^{-1}	1.0×10^{-5}	6.0×10^{-2}	2.0×10^{-11}

1990ApJS...72...750

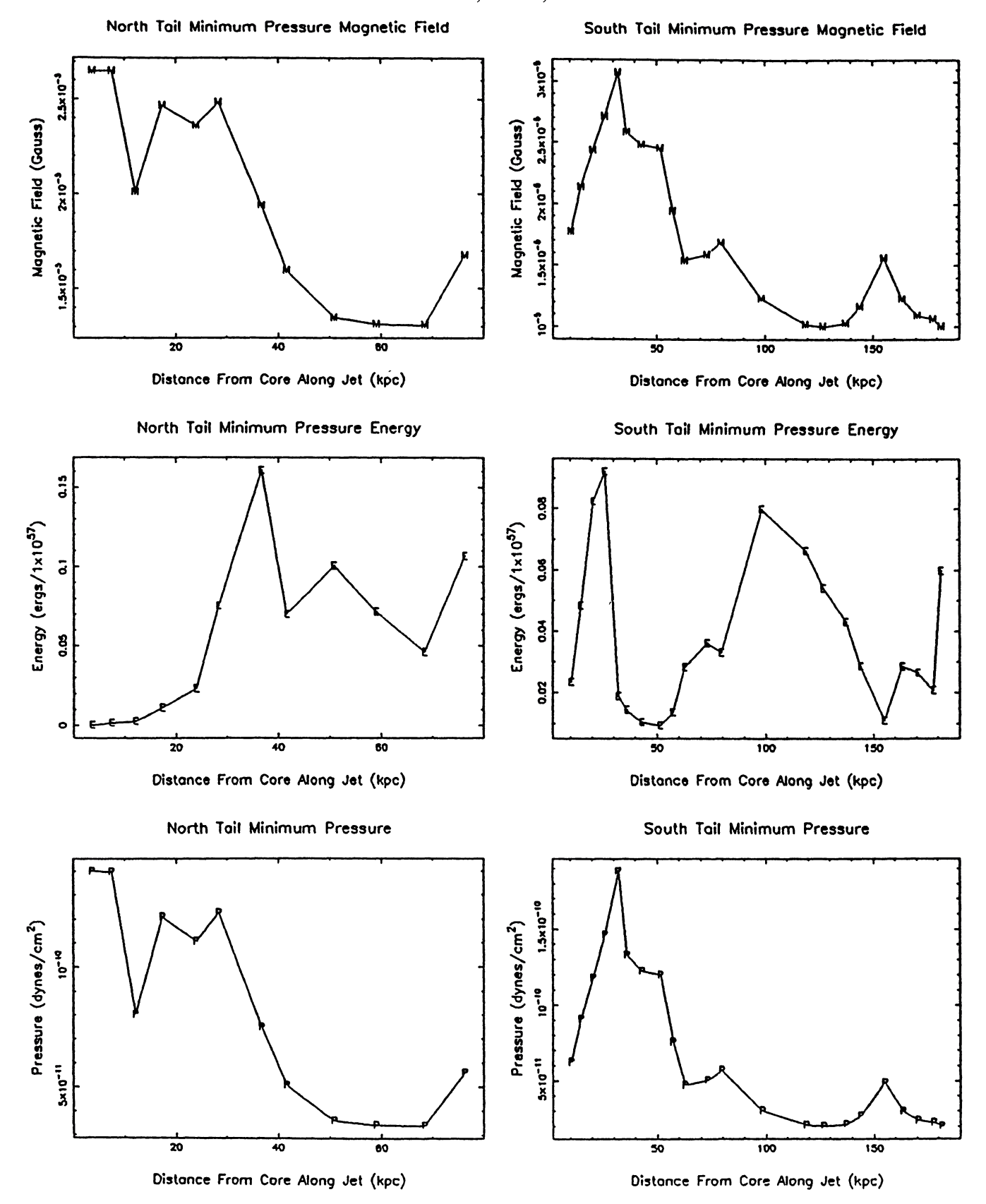


FIG. 34.—Estimates of the magnetic field, total energy (within one slice across the tail), and pressure, derived from minimum pressure arguments, for the north and south tails of 1159+583. Values are given for slice positions shown in Fig. 32. Data are given in Tables 13 and 14.

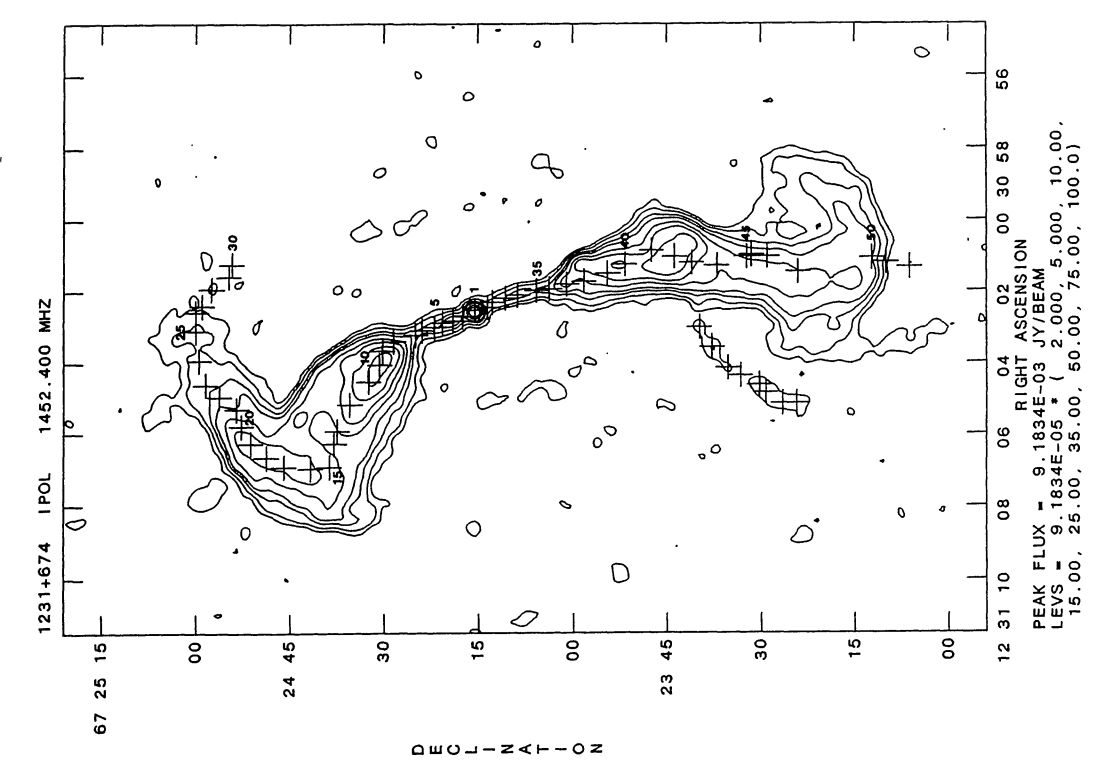


FIG. 39.—Positions of the centers of slices taken perpendicular to the jets and tails of 1231+674, on a low-resolution contour plot. Spectral indices and minimum pressure values for these slices are shown in Figs. 40 and 41.

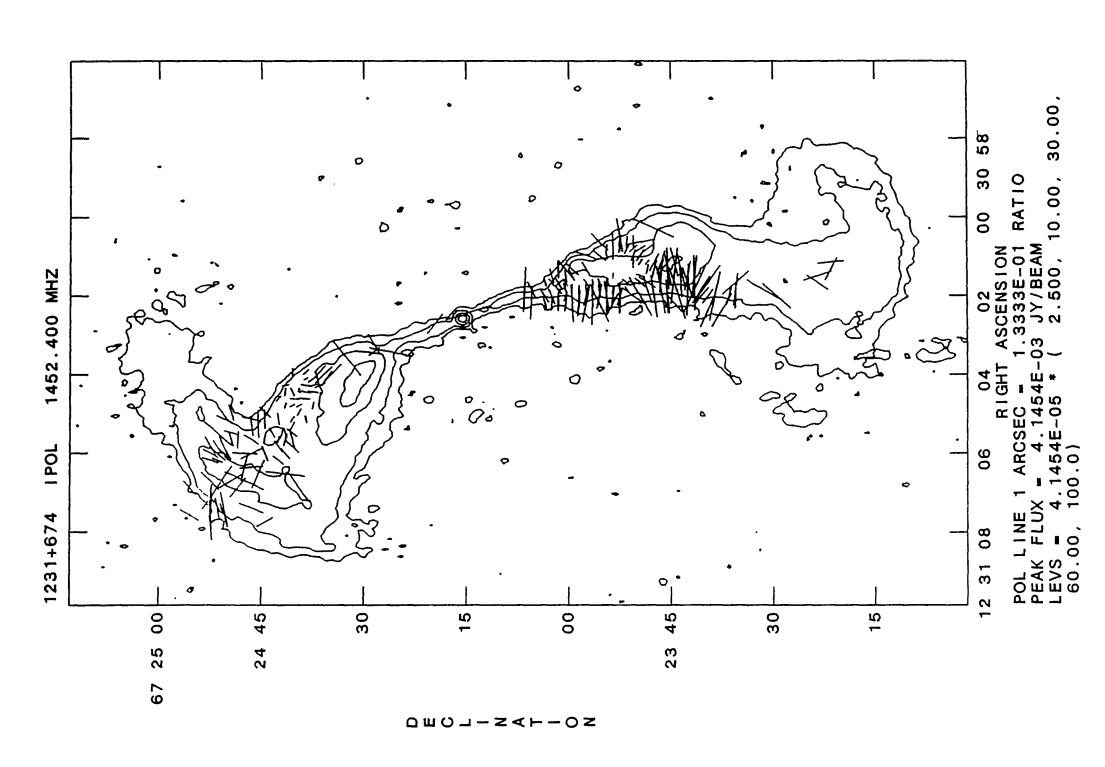
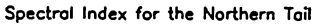
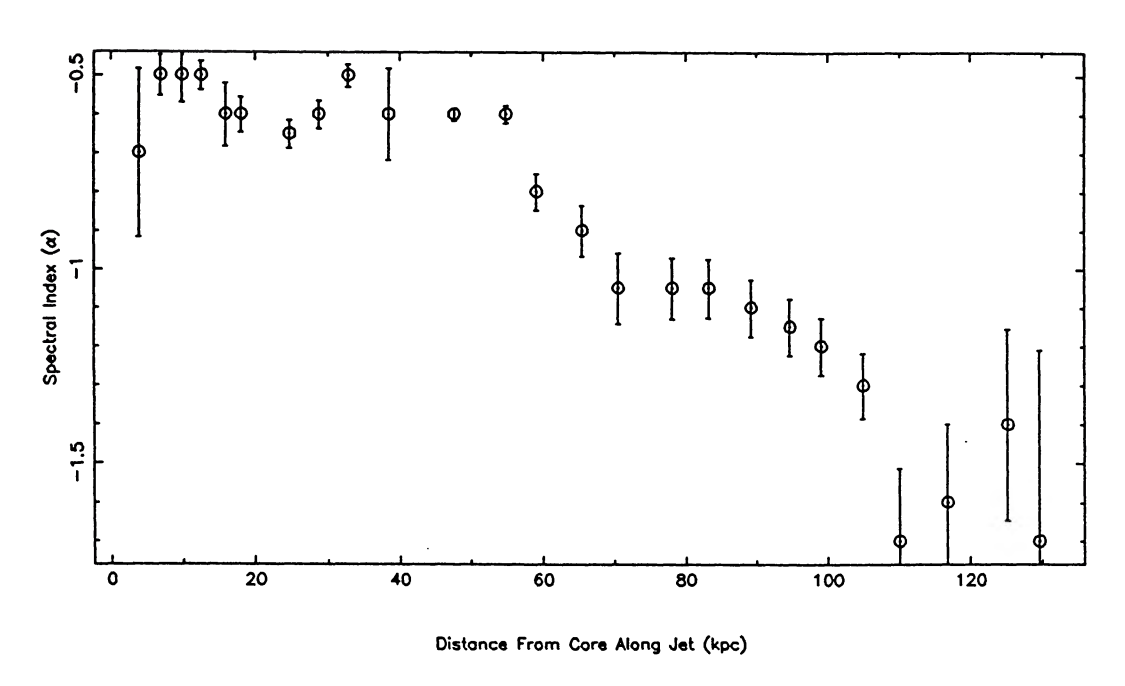


FIG. 38.—Polarization angles for 1231+674, uncorrected for Faraday rotation. Contours are those of the full resolution 20 cm image, and lengths of the vectors are proportional to the fractional polarization at 6 cm.





Spectral Index for the Southern Tail

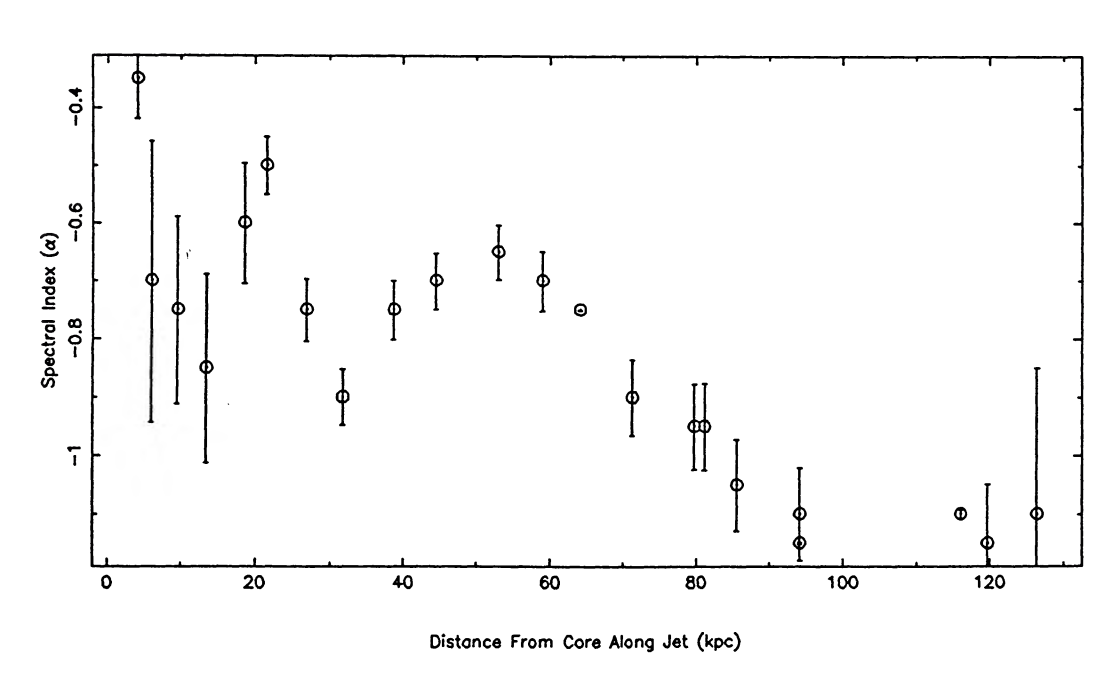


FIG. 40.—Spectral index values between 6 and 20 cm for 1231+674. Values were determined using estimated mean values from slices taken across the total intensity maps, at positions shown in Fig. 39.

TABLE 15
1231+674 Northern Tail Minimum Pressure

Number	Distance (kpc)	Diameter (kpc)	S per Beam (mJy per beam)	Volume (kpc ³)	Luminosity (10 ⁴¹ ergs s ⁻¹)	H _{min} (G)	$\frac{E_{\min}}{(10^{57} \text{ergs})}$	P_{\min} (dyne cm ⁻²)
2	3.9	0.51	0.24	2.1×10^{-1}	1.3×10^{-2}	2.1×10^{-5}	5.6×10^{-4}	9.0×10^{-11}
3	6.9	1.19	0.99	1.2	5.0×10^{-2}	2.0×10^{-5}	2.6×10^{-3}	7.6×10^{-11}
4	9.9	1.79	0.99	2.6	5.0×10^{-2}	1.5×10^{-5}	3.7×10^{-3}	4.7×10^{-11}
5	12.5	2.40	1.13	4.7	5.8×10^{-2}	1.4×10^{-5}	5.1×10^{-3}	3.7×10^{-11}
6	15.9	2.80	1.17	$1.1 \times 10^{+1}$	6.0×10^{-2}	1.1×10^{-5}	7.4×10^{-3}	2.3×10^{-11}
7	18.0	2.29	1.16	7.2	5.9×10^{-2}	1.2×10^{-5}	6.2×10^{-3}	2.9×10^{-11}
8	24.7	6.46	9.14	$5.8 \times 10^{+1}$	4.7×10^{-1}	1.2×10^{-5}	4.9×10^{-2}	2.9×10^{-11}
9	28.7	8.11	23.24	$9.1 \times 10^{+1}$	1.2	1.4×10^{-5}	1.0×10^{-1}	3.8×10^{-11}
10	32.8	8.80	29.95	$1.1 \times 10^{+2}$	1.5	1.4×10^{-5}	1.3×10^{-1}	4.0×10^{-11}
11	38.4	12.39	63.22	$4.3 \times 10^{+2}$	3.2	1.2×10^{-5}	3.5×10^{-1}	2.8×10^{-11}
12	47.6	16.01	53.41	$7.1 \times 10^{+2}$	2.7	9.7×10^{-6}	3.9×10^{-1}	1.9×10^{-11}
13	54.8	20.74	48.80	$1.2 \times 10^{+3}$	2.5	8.2×10^{-6}	4.7×10^{-1}	1.3×10^{-11}
14	59.1	22.31	50.50	$1.4 \times 10^{+3}$	2.6	7.9×10^{-6}	5.1×10^{-1}	1.3×10^{-11}
15	65.4	24.75	67.13	$1.7 \times 10^{+3}$	3.4	8.1×10^{-6}	6.5×10^{-1}	1.3×10^{-11}
16	70.5	22.93	72.78	1.5×10 ⁺³	3.7	8.7×10^{-6}	6.4×10^{-1}	1.5×10^{-11}
17	78.1	16.56	54.59	$7.6 \times 10^{+2}$	2.8	9.6×10^{-6}	4.1×10^{-1}	1.8×10^{-11}
18	83.2	14.00	45.65	$5.4 \times 10^{+2}$	2.3	1.0×10^{-5}	3.2×10^{-1}	2.0×10^{-11}
19	89.2	12.19	36.54	$4.1 \times 10^{+2}$	1.9	1.0×10^{-5}	2.5×10^{-1}	2.1×10^{-11}
20	94.7	10.82	26.61	$3.2 \times 10^{+2}$	1.4	1.0×10^{-5}	1.9×10^{-1}	2.0×10^{-11}
21	99.1	10.78	18.87	3.2×10 ⁺²	9.7×10^{-1}	9.1×10^{-6}	1.6×10^{-1}	1.6×10^{-11}
22	104.9	11.96	13.08	$4.0 \times 10^{+2}$	6.7×10^{-1}	7.7×10^{-6}	1.4×10^{-1}	1.2×10^{-11}
23	110.0	13.16	10.65	$4.8 \times 10^{+2}$	5.4×10^{-1}	6.9×10^{-6}	1.3×10^{-1}	9.4×10^{-12}
24	116.7	11.30	6.78	$3.5 \times 10^{+2}$	3.5×10^{-1}	6.6×10^{-6}	9.0×10^{-2}	8.7×10^{-12}
25	125.5	14.84	10.84	$1.2 \times 10^{+3}$	5.5×10^{-1}	5.3×10^{-6}	2.0×10^{-1}	5.6×10^{-12}
26	129.6	17.73	8.72	$1.7 \times 10^{+3}$	4.5×10^{-1}	4.5×10^{-6}	2.1×10^{-1}	4.0×10^{-12}
27	132.1	18.41	7.63	$1.9 \times 10^{+3}$	3.9×10^{-1}	4.2×10^{-6}	2.0×10^{-1}	3.6×10^{-12}
28	137.2	20.71	6.04	$2.4 \times 10^{+3}$	3.1×10^{-1}	3.7×10^{-6}	1.9×10^{-1}	2.7×10^{-12}
29	142.5	17.89	4.45	$1.8 \times 10^{+3}$	2.3×10^{-1}	3.7×10^{-6}	1.4×10^{-1}	2.7×10^{-12}
30		17.82	3.70	$1.8 \times 10^{+3}$	1.9×10^{-1}	3.5×10^{-6}	1.3×10^{-1}	2.5×10^{-12}

TABLE 16
1231+674 SOUTHERN TAIL MINIMUM PRESSURE

Number	Distance (kpc)	Diameter (kpc)	S per Beam (mJy per beam)	Volume (kpc ³)	Luminosity (10 ⁴¹ ergs s ⁻¹)	H _{min} (G)	$\frac{E_{\min}}{(10^{57}\mathrm{ergs})}$	P_{\min} (dyne cm ⁻²)
31	4.1	0.56	0.11	2.6×10^{-1}	4.5×10^{-3}	1.6×10^{-5}	4.0×10^{-4}	5.3×10^{-11}
32	6.0	0.88	0.38	6.4×10^{-1}	1.6×10^{-2}	1.8×10^{-5}	1.2×10^{-3}	6.5×10^{-11}
33	9.5	0.99	0.44	8.1×10^{-1}	1.9×10^{-2}	1.8×10^{-5}	1.5×10^{-3}	6.2×10^{-11}
34	13.4	0.58	0.34	2.7×10^{-1}	1.5×10^{-2}	2.2×10^{-5}	8.0×10^{-4}	1.0×10^{-10}
35	18.5	1.64	0.61	2.2	2.6×10^{-2}	1.5×10^{-5}	2.7×10^{-3}	4.2×10^{-11}
36	21.5	3.14	1.44	$1.4 \times 10^{+1}$	6.1×10^{-2}	1.1×10^{-5}	9.7×10^{-3}	2.4×10^{-11}
37	26.8	3.79	4.61	$2.0 \times 10^{+1}$	2.0×10^{-1}	1.4×10^{-5}	2.2×10^{-2}	3.8×10^{-11}
38	31.7	7.27	10.82	$7.3 \times 10^{+1}$	4.6×10^{-1}	1.2×10^{-5}	6.3×10^{-2}	2.9×10^{-11}
39	38.6	7.76	14.44	$8.3 \times 10^{+1}$	6.2×10^{-1}	1.3×10^{-5}	7.9×10^{-2}	3.2×10^{-11}
40	44.4	8.71	29.85	$2.1 \times 10^{+2}$	1.3	1.2×10^{-5}	1.8×10^{-1}	2.9×10^{-11}
41	52.9	11.03	45.80	$3.4 \times 10^{+2}$	2.0	1.2×10^{-5}	2.8×10^{-1}	2.8×10^{-11}
42	58.9	11.69	57.80	$3.8 \times 10^{+2}$	2.5	1.2×10^{-5}	3.3×10^{-1}	3.0×10^{-11}
43	64.0	11.67	46.28	$3.8 \times 10^{+2}$	2.0	1.2×10^{-5}	2.9×10^{-1}	2.6×10^{-11}
44	71.2	11.39	28.08	$3.6 \times 10^{+2}$	1.2	1.0×10^{-5}	2.1×10^{-1}	2.0×10^{-11}
45	79.7	11.65	25.61	$3.8 \times 10^{+2}$	1.1	9.7×10^{-6}	2.1×10^{-1}	1.9×10^{-11}
46	81.1	12.00	26.23	$4.0 \times 10^{+2}$	1.1	9.6×10^{-6}	2.2×10^{-1}	1.8×10^{-11}
47	85.5	14.79	32.03	$6.1 \times 10^{+2}$	1.4	9.0×10^{-6}	2.9×10^{-1}	1.6×10^{-11}
48	94.2	24.03	46.77	$1.6 \times 10^{+3}$	2.0	7.6×10^{-6}	5.5×10^{-1}	1.2×10^{-11}
49	94.2	18.86	9.88	$9.9 \times 10^{+2}$	4.2×10^{-1}	5.6×10^{-6}	1.8×10^{-1}	6.3×10^{-12}
50	116.0	18.60	8.97	$9.6 \times 10^{+2}$	3.8×10^{-1}	5.5×10^{-6}	1.7×10^{-1}	6.1×10^{-12}
51	119.7	22.91	31.63	2.9×10 ⁺³	1.3	5.8×10^{-6}	5.6×10^{-1}	6.6×10^{-12}
52	126.4	31.05	10.57	$5.3 \times 10^{+3}$	4.5×10^{-1}	3.5×10^{-6}	3.9×10^{-1}	2.5×10^{-12}

1990ApJS...72...750

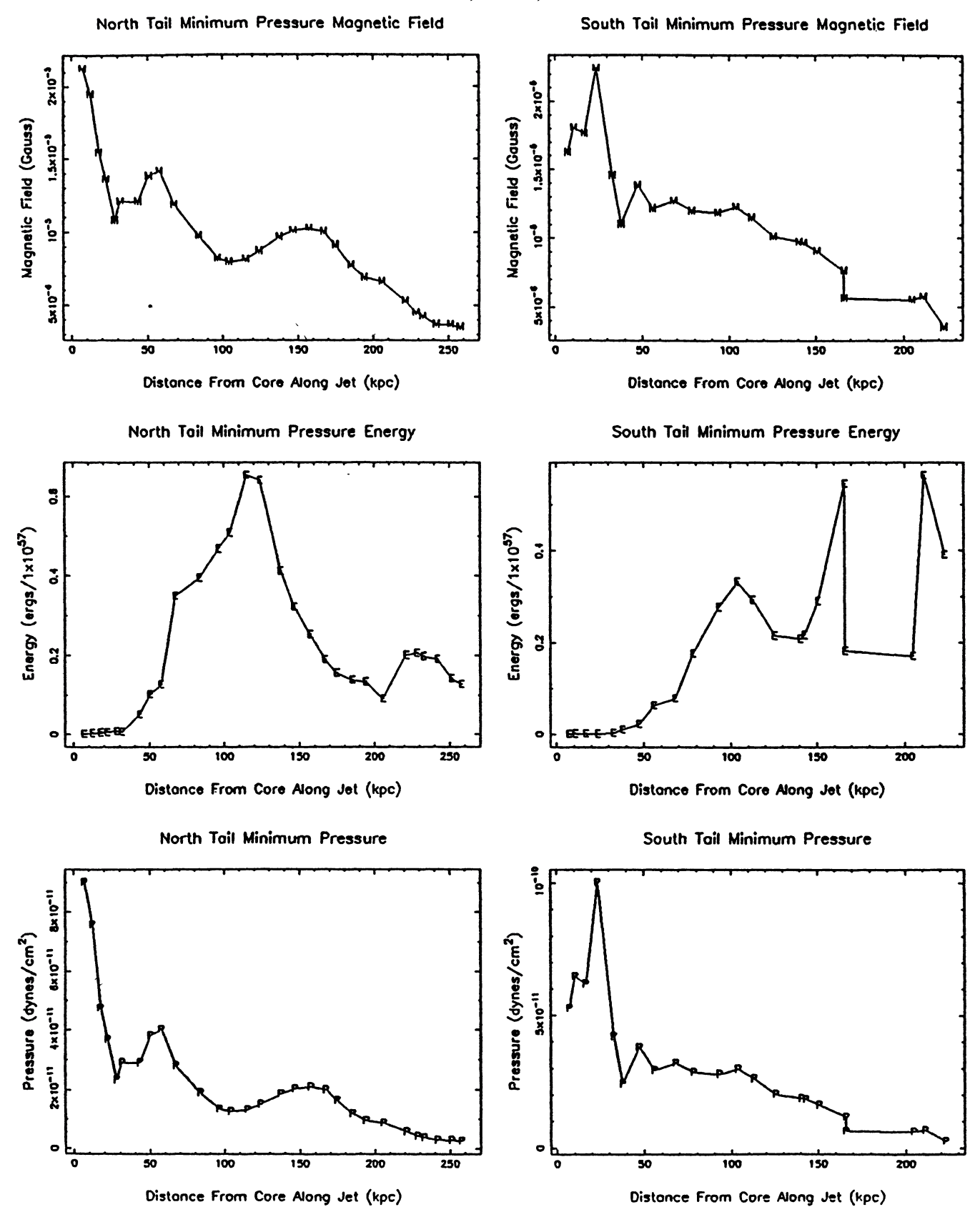


Fig. 41.—Estimates of the magnetic field, total energy (within one slice across the tail), and pressure, derived from minimum pressure arguments, for the north and south tails of 1231+674. The values are given for slice positions shown in Fig. 39. Data are given in Tables 15 and 16.

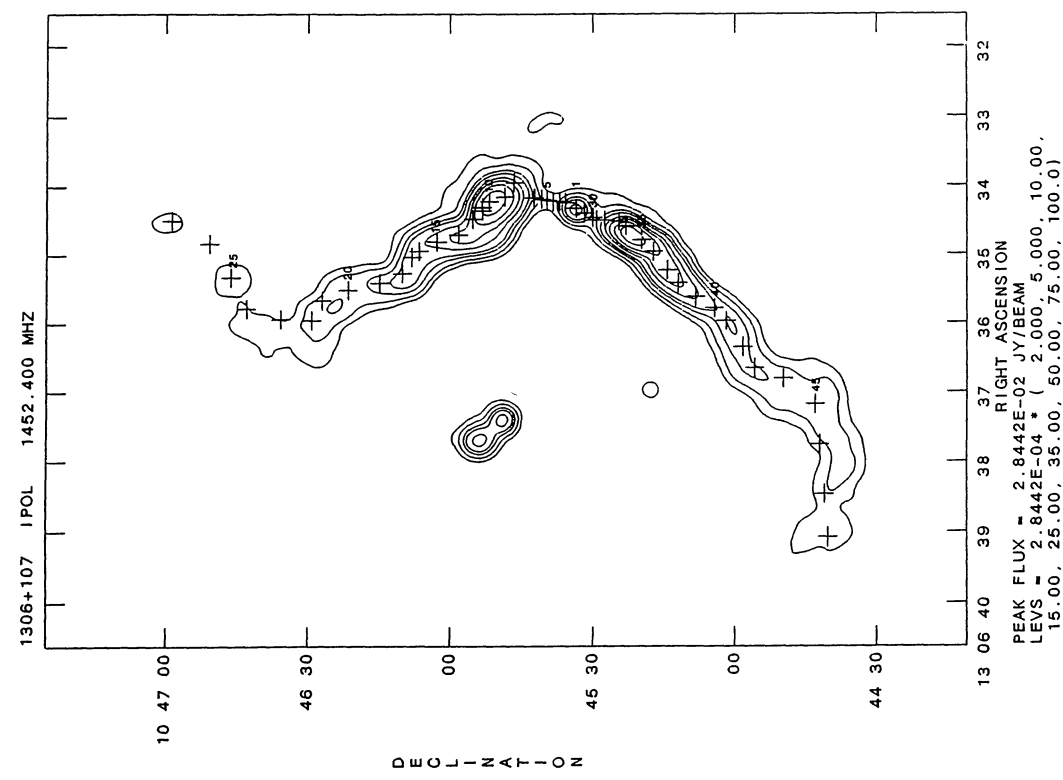


Fig. 45.—Positions of the centers of slices taken perpendicular to the jets and tails of 1306+107, on a low-resolution contour plot. Spectral indices and minimum pressure values for these slices are shown in Figs. 46 and 47.

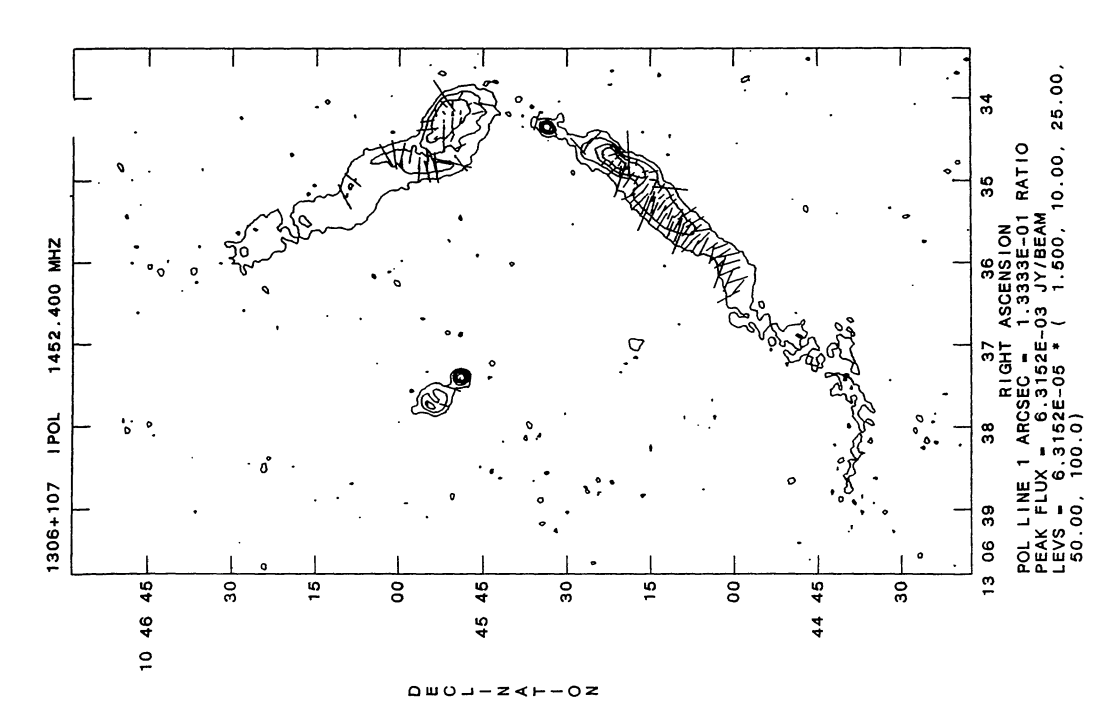
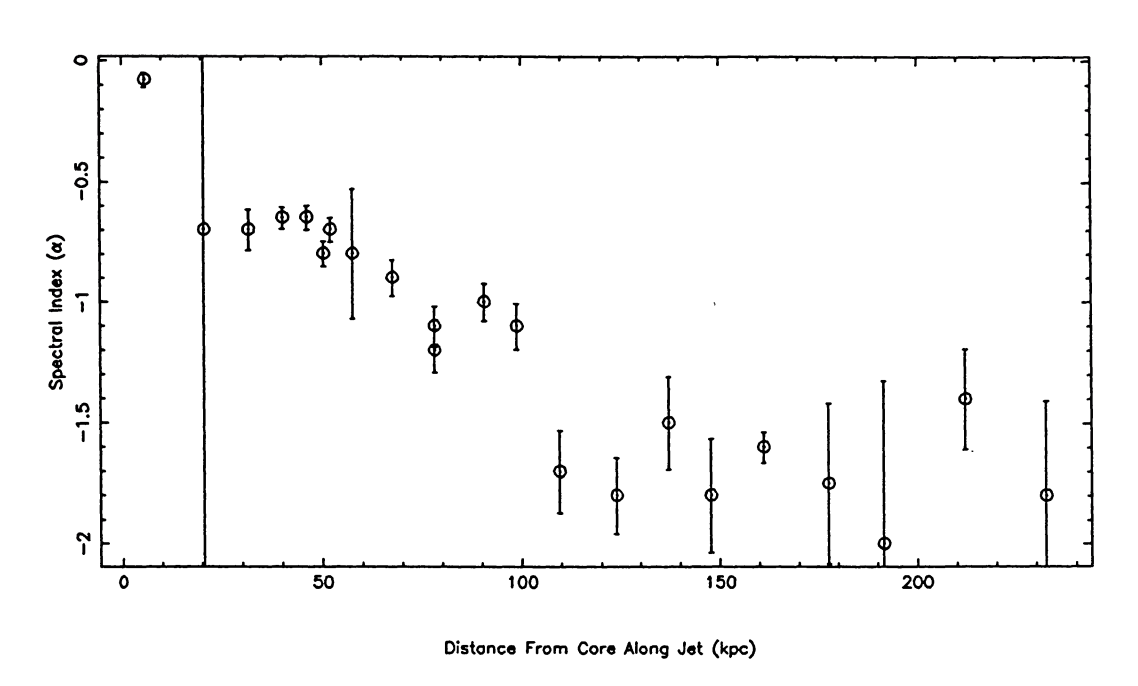
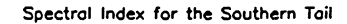


FIG. 44.—Polarization vectors for 1306+107, uncorrected for Faraday rotation. Contours are those of the full resolution 20 cm image, and lengths of the vectors are proportional to the fractional polarization at 6 cm.

Spectral Index for the Northern Tail





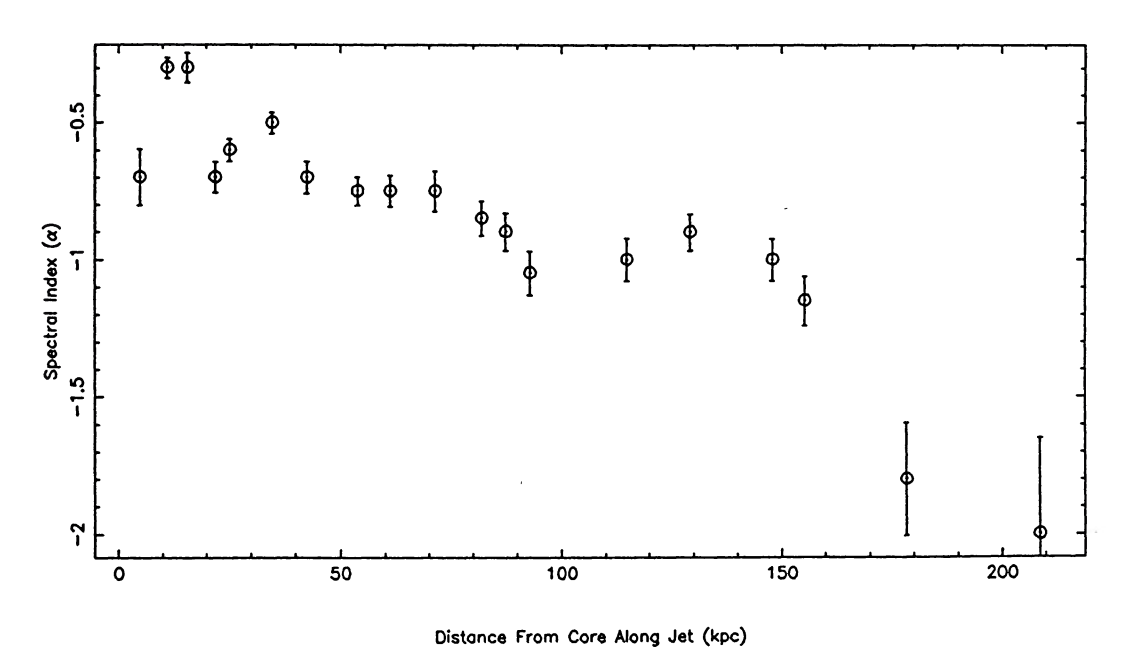


FIG. 46.—Spectral index values between 6 and 20 cm for 1306+107. Values were determined using estimated mean values from slices taken across the total intensity maps, at positions shown in Fig. 45.

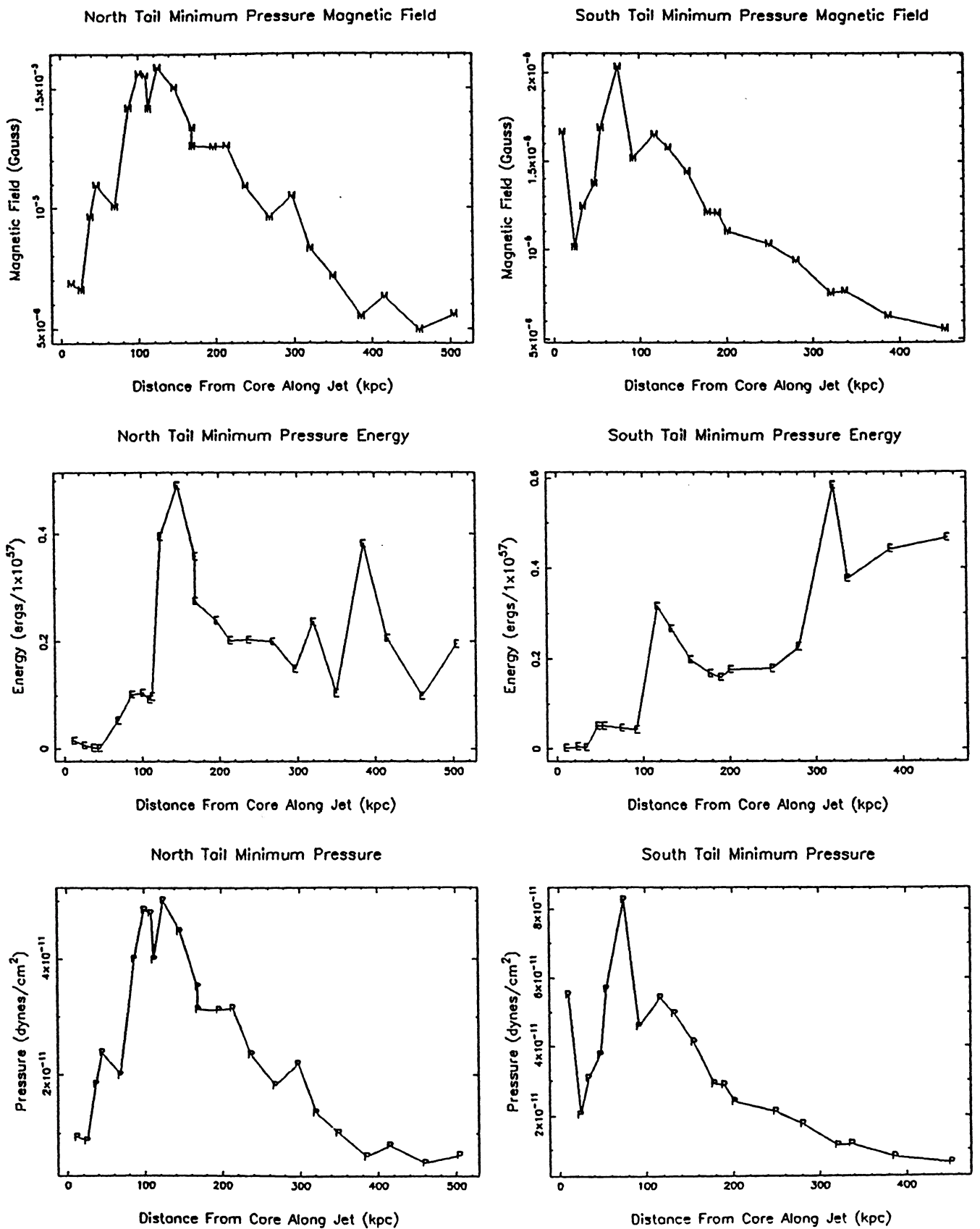


FIG. 47.—Estimates of the magnetic field, total energy (within one slice across the tail), and pressure, derived from minimum pressure arguments, for the north and south tails of 1306+107. Values are given for slice positions shown in Fig. 45. Data are given in Tables 17 and 18.

O'DONOGHUE, OWEN, AND EILEK TABLE 17

1306+107 Northern Tail Minimum Pressure

Number	Distance (kpc)	Diameter (kpc)	S per Beam (mJy per beam)	Volume (kpc ³)	Luminosity (10 ⁴¹ ergs s ⁻¹)	H_{\min} (G)	E_{\min} (10 ⁵⁷ ergs)	P_{\min} (dyne cm ⁻²)
2	5.6	7.20	0.61	5.2×10 ⁺¹	4.3×10 ⁻²	6.9×10 ⁻⁶	1.4×10^{-2}	9.3×10^{-12}
4	11.5	4.84	0.24	$2.4 \times 10^{+1}$	1.7×10^{-2}	6.6×10^{-6}	6.0×10^{-3}	8.7×10^{-12}
6	16.9	1.71	0.11	2.9	7.9×10^{-3}	9.6×10^{-6}	1.6×10^{-3}	1.8×10^{-11}
7	20.6	1.06	0.07	1.1	4.9×10^{-3}	1.1×10^{-5}	8.0×10^{-4}	2.4×10^{-11}
8	31.7	9.46	4.01	$9.0 \times 10^{+1}$	2.8×10^{-1}	1.0×10^{-5}	5.3×10^{-2}	2.0×10^{-11}
9	40.1	9.27	12.97	$8.6 \times 10^{+1}$	9.2×10^{-1}	1.4×10^{-5}	1.0×10^{-1}	4.0×10^{-11}
10	46.2	8.55	15.39	$7.3 \times 10^{+1}$	1.1	1.6×10^{-5}	1.0×10^{-1}	4.8×10^{-11}
11	50.3	8.09	13.48	$6.6 \times 10^{+1}$	9.5×10^{-1}	1.6×10^{-5}	9.2×10^{-2}	4.8×10^{-11}
12	52.0	9.11	12.48	$8.3 \times 10^{+1}$	8.8×10^{-1}	1.4×10^{-5}	9.8×10^{-2}	4.0×10^{-11}
13	57.5	12.51	59.55	$2.7 \times 10^{+2}$	4.2	1.6×10^{-5}	3.9×10^{-1}	5.0×10^{-11}
14	67.4	14.76	68.14	$3.7 \times 10^{+2}$	4.8	1.5×10^{-5}	4.9×10^{-1}	4.5×10^{-11}
15	78.1	14.19	41.50	$3.4 \times 10^{+2}$	2.9	1.3×10^{-5}	3.6×10^{-1}	3.5×10^{-11}
16	78.1	13.19	29.28	$3.0 \times 10^{+2}$	2.1	1.3×10^{-5}	2.8×10^{-1}	3.1×10^{-11}
17	90.7	12.32	25.34	$2.6 \times 10^{+2}$	1.8	1.3×10^{-5}	2.4×10^{-1}	3.1×10^{-11}
18	98.7	11.27	21.53	$2.2 \times 10^{+2}$	1.5	1.3×10^{-5}	2.0×10^{-1}	3.2×10^{-11}
19	,	13.09	17.39	$2.9 \times 10^{+2}$	1.2	1.1×10^{-5}	2.0×10^{-1}	2.4×10^{-11}
20		14.75	14.13	$3.7 \times 10^{+2}$	1.0	9.6×10^{-6}	2.0×10^{-1}	1.8×10^{-11}
21	137.1	11.62	12.04	2.3×10 ⁺²	8.5×10^{-1}	1.0×10^{-5}	1.5×10 ⁻¹	22×10 ⁻¹¹
22	147.7	18.54	13.41	$5.9 \times 10^{+2}$	9.5×10^{-1}	8.3×10^{-6}	2.4×10^{-1}	1.4×10^{-11}
23		14.23	4.70	$3.5 \times 10^{+2}$	3.3×10^{-1}	7.1×10^{-6}	1.0×10^{-1}	1.0×10^{-11}
24		25.18	11.73	$2.2 \times 10^{+3}$	8.3×10^{-1}	5.5×10^{-6}	3.8×10^{-1}	6.0×10^{-12}
25		16.13	7.76	$8.9 \times 10^{+2}$	5.5×10^{-1}	6.3×10^{-6}	2.1×10^{-1}	7.9×10^{-12}
26	212.1	14.21	2.59	6.9×10 ⁺²	1 8×10 ⁻¹	4.9×10^{-6}	9.8×10 ⁻²	4.9×10^{-12}
27		17.72	6.13	$1.1 \times 10^{+3}$	4.3×10^{-1}	5.6×10^{-6}	1.9×10^{-1}	6.2×10^{-12}

TABLE 18 1306+107 SOUTHERN TAIL MINIMUM PRESSURE

Number	Distance (kpc)	Diameter (kpc)	S per Beam (mJy per beam)	Volume (kpc ³)	Luminosity (10 ⁴¹ ergs s ⁻¹)	H _{min} (G)	$\frac{E_{\min}}{(10^{57}\mathrm{ergs})}$	P _{min} (dyne cm ⁻²)
28	4.8	1.09	0.31	1.2	2.1×10 ⁻²	1.7×10 ⁻⁵	1.9×10 ⁻³	5.5×10^{-11}
30	11.1	2.78	0.36	7.8	2.5×10^{-2}	1.0×10^{-5}	4.7×10^{-3}	2.0×10^{-11}
31	15.6	1.89	0.33	3.6	2.3×10^{-2}	1.2×10^{-5}	3.2×10^{-3}	3.1×10^{-11}
32	21.9	6.78	6.12	$4.6 \times 10^{+1}$	4.3×10^{-1}	1.4×10^{-5}	5.1×10^{-2}	3.8×10^{-11}
33	25.2	5.53	8.39	$3.1 \times 10^{+1}$	5.8×10^{-1}	1.7×10^{-5}	5.1×10^{-2}	5.7×10^{-11}
34	34.7	4.40	10.21	$1.9 \times 10^{+1}$	7.1×10^{-1}	2.0×10^{-5}	4.7×10^{-2}	8.3×10^{-11}
35	42.5	5.60	5.91	$3.1 \times 10^{+1}$	4.1×10^{-1}	1.5×10^{-5}	4.2×10^{-2}	4.6×10^{-11}
36	53.8	10.75	49.87	$2.0 \times 10^{+2}$	3.5	1.7×10^{-5}	3.2×10^{-1}	5.4×10^{-11}
37	61.2	10.31	39.26	$1.8 \times 10^{+2}$	2.7	1.6×10^{-5}	2.7×10^{-1}	5.0×10^{-11}
38	71.4	9.76	25.51	$1.6 \times 10^{+2}$	1.8	1.4×10^{-5}	2.0×10^{-1}	4.1×10^{-11}
39	82.0	10.68	16.61	$2.0 \times 10^{+2}$	1.2	1.2×10^{-5}	1.7×10^{-1}	2.9×10^{-11}
40	87.4	10.48	15.69	$1.9 \times 10^{+2}$	1.1	1.2×10^{-5}	1.6×10^{-1}	2.9×10^{-11}
41	92.8	12.06	15.20	2.5×10 ⁺²	1.1	1.1×10 ⁻⁵	1.8×10^{-1}	2.4×10^{-11}
42	114.9	12.95	14.00	$2.9 \times 10^{+2}$	9.7×10^{-1}	1.0×10^{-5}	1.8×10^{-1}	2.1×10^{-11}
43	129.3	15.97	15.33	$4.4 \times 10^{+2}$	1.1	9.4×10^{-6}	2.3×10^{-1}	1.8×10^{-11}
44	147.9	22.64	28.64	$1.7 \times 10^{+3}$	2.0	7.6×10^{-6}	5.8×10^{-1}	1.1×10^{-11}
45	155.3	17.95	18.93	$1.1 \times 10^{+3}$	1.3	7.7×10^{-6}	3.8×10^{-1}	1.2×10^{-11}
46	178.3	23.72	16.41	1.9×10 ⁺³	1.1	6.3×10^{-6}	4.4×10^{-1}	7.8×10^{-12}
47	208.6	27.55	14.41	$2.6 \times 10^{+3}$	1.0	5.6×10^{-6}	4.7×10^{-1}	6.1×10^{-12}

No. 1, 1990

are artifacts in the image, so it is not absolutely certain that the twin jet structure is real. The radio contours superposed on the optical galaxy image are shown in Figure 49 (Plate 65).

ii) Polarization

At 20 cm, almost none of the source shows polarized emission above the 3- σ level. At 6 cm, much more of the source is seen, indicating rather dramatic depolarization. The hot spots, in particular, stand out at 6 cm. Also seen are the northern tail through and slightly beyond the bend and the southern hot spot extension. The fractional polarization at 6 cm is shown by the vectors in Figure 50.

iii) Spectral Index and Minimum Pressure Analysis

In the spectral index image no particular features stand out. At full resolution the image is quite mottled, reflecting the low flux density at 6 cm. The northern tail steepens rather smoothly from -0.7 to about -1.0. The southern jet is unusual in that it flattens from -0.7 to -0.4; however, the jet at 6 cm is not much above the noise so this may not be a true trend. The southern hot spot has a spectral index ranging from -0.7 to -0.8. The southwest extension of the hot spot then steepens to almost -1.0.

The slice centers are shown in Figure 51; the spectral index values taken from these cross-tail slices are shown in Figure 52. The results of the minimum-pressure analysis are given in Tables 19 and 20, and shown in Figure 53.

i) 1636+379

One of the larger sources, 1636+379 presents an unusual displacement of the southern tail from the jet direction. This can be seen in the high-resolution 20 cm image, given in Figure 54 (Plate 66). The jet is actually lost in the noise and cannot be followed into the tail which is markedly south of the extrapolated jet location. Thus there must be an invisible bend. This is accompanied by an uncommon asymmetry where the northern tail and jet bend much less than the southern tail and jet, which bend well over 90°. Both of these features may indicate that the source does not lie in the plane of the sky.

The cluster, A2214, is cited as a Bautz-Morgan class II by Simon (1978). Radio data in the literature include discussions by Colla et al. (1973) in the 408 MHz B2 survey, Owen (1975b), (2695 MHz), Riley (1975) (408, and 1407 MHz), Owen and Rudnick (1976), who include this source in the original six WATs and the definition of the class, Rudnick and Owen (1977) (2695 and 8085 MHz), Simon (1978) (408 MHz), and Valentijn (1979a, b).

i) Source Structure

At low resolution, 1636+379 appears to be a classic WAT with nearly symmetric bends. It also displays, as do 0043+201 and 1231+674, flattening at the ends of the tails, and, at 20 cm, the flattening causes the tails to almost meet. The radio contours are overlaid on the optical galaxy image in Figure 55 (Plate 67).

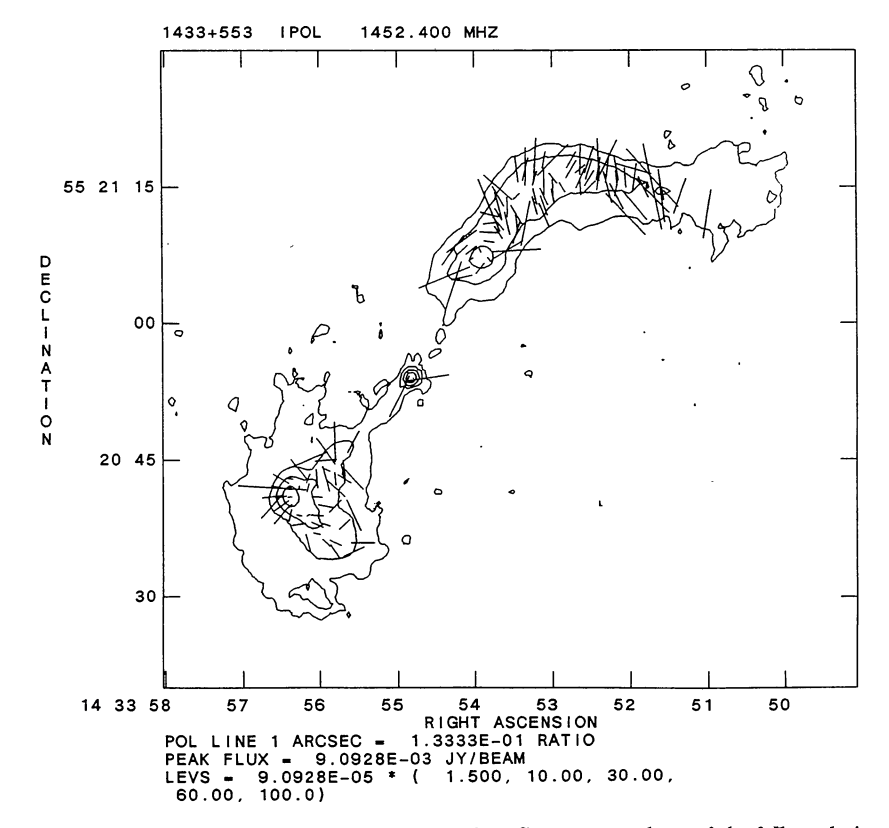


FIG. 50.—Polarization vectors for 1433+553, uncorrected for Faraday rotation. Contours are those of the full resolution 20 cm image, and lengths of the vectors are proportional to the fractional polarization at 6 cm.

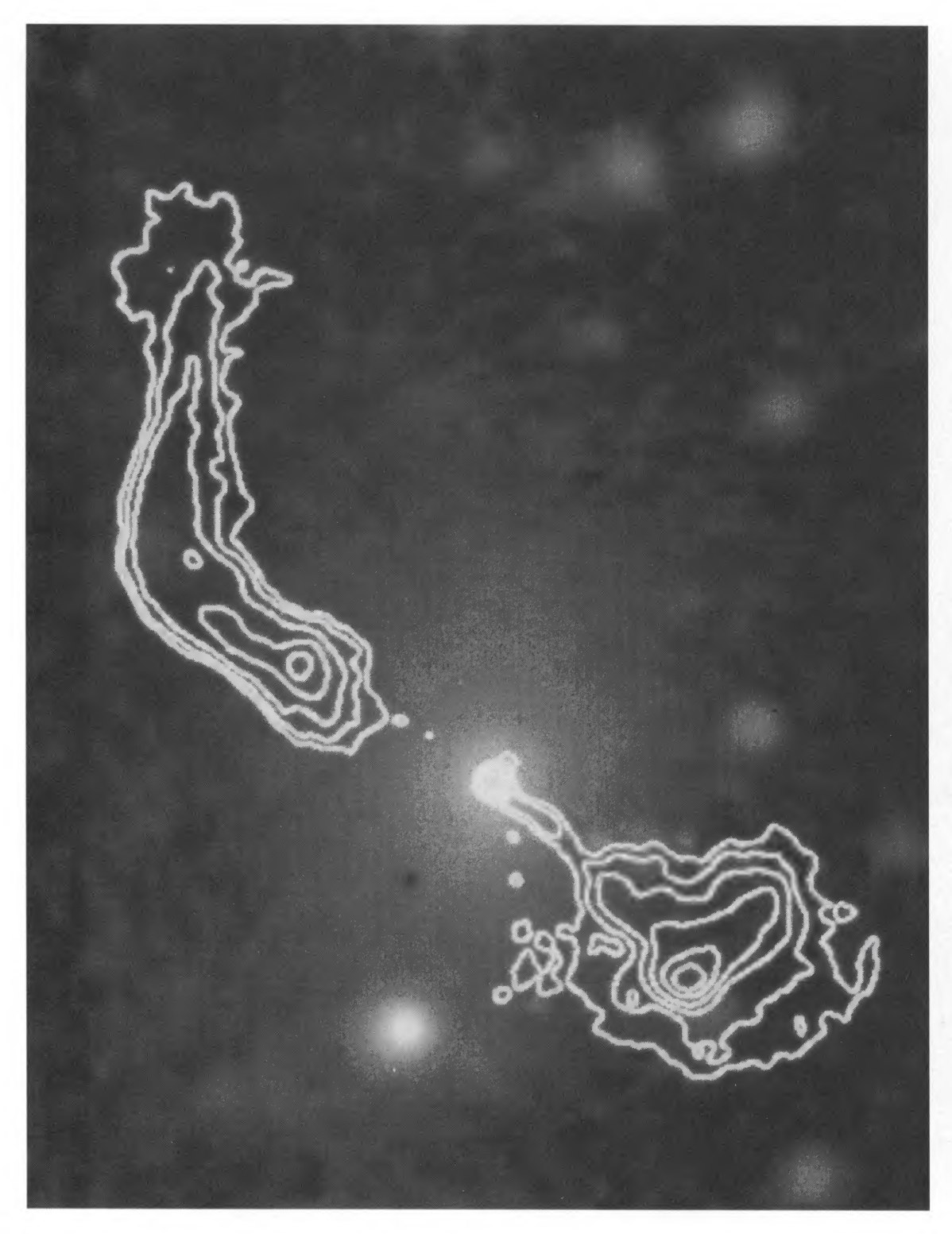


Fig. 49.—20 cm contours of 1433+553 overlaid on the optical galaxy image

O'DONOGHUE, OWEN, AND EILEK (see 72, 113)

Fig. 54.—High-resolution (1") image of 1636+379 at 20 cm

O'DONOGHUE, OWEN, AND EILEK (see 72, 113)

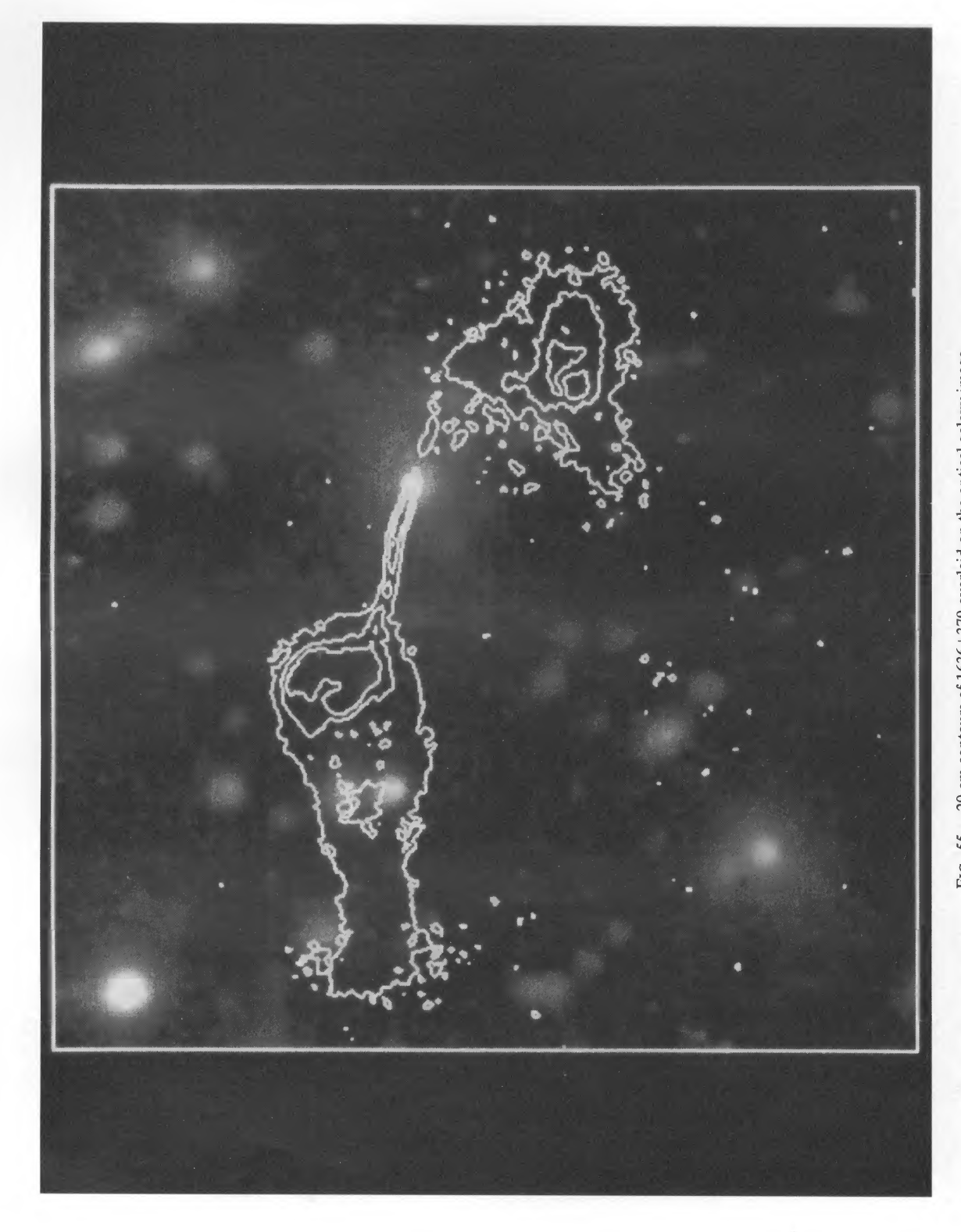


Fig. 55.—20 cm contours of 1636+379 overlaid on the optical galaxy image

O'DONOGHUE, OWEN, AND EILEK (see 72, 113)

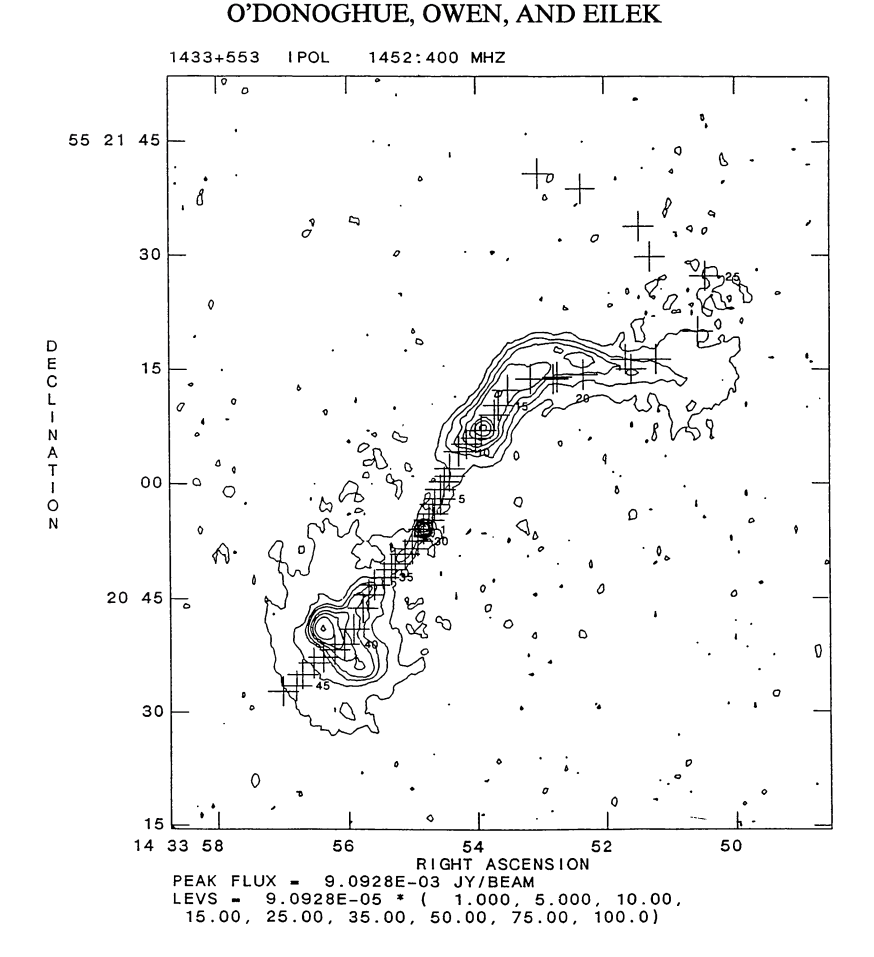


Fig. 51.—Positions of the centers of slices taken perpendicular to the jets and tails of 1433+553, on a low-resolution contour plot. Spectral indices and minimum pressure values for these slices are shown in Figs. 52 and 53.

ii) Polarization

The most outstanding features in polarized flux at 20 cm full resolution are the northern jet inside the lobe, the northern edge of the northern circular lobe and tail, part of the ring structure in the eastern part of the southern lobe, and the edge of the oval centered in the southern part of the lobe surrounding the ring structure. The jet, mostly blanked outside the lobe, is only $\sim 10\%$ polarized, increasing to 30% inside the lobe. The northern edge of the circular hot spot is slightly steeper as is the edge of the tail that goes up to almost 50%. The southern edge of the lobe also has a higher fractional polarization and the narrowest part of the lobe, where the edges meet, has values up to and beyond 50%. The southern jet is almost completely blanked. In the lobe, the inner part of the ring structure is only 10% to 20% polarized, while the polarization of the outer part increases up to 30%. A notable feature supporting the hot spot as the terminus of the jet is that it is much less polarized than the lobe, having values of only 5% to 10%.

At 6 cm, the same features are revealed with only slightly different values. This source is the least depolarized of all the sources. The polarization vectors scaled to the 6 cm fractional polarization are shown in Figure 56.

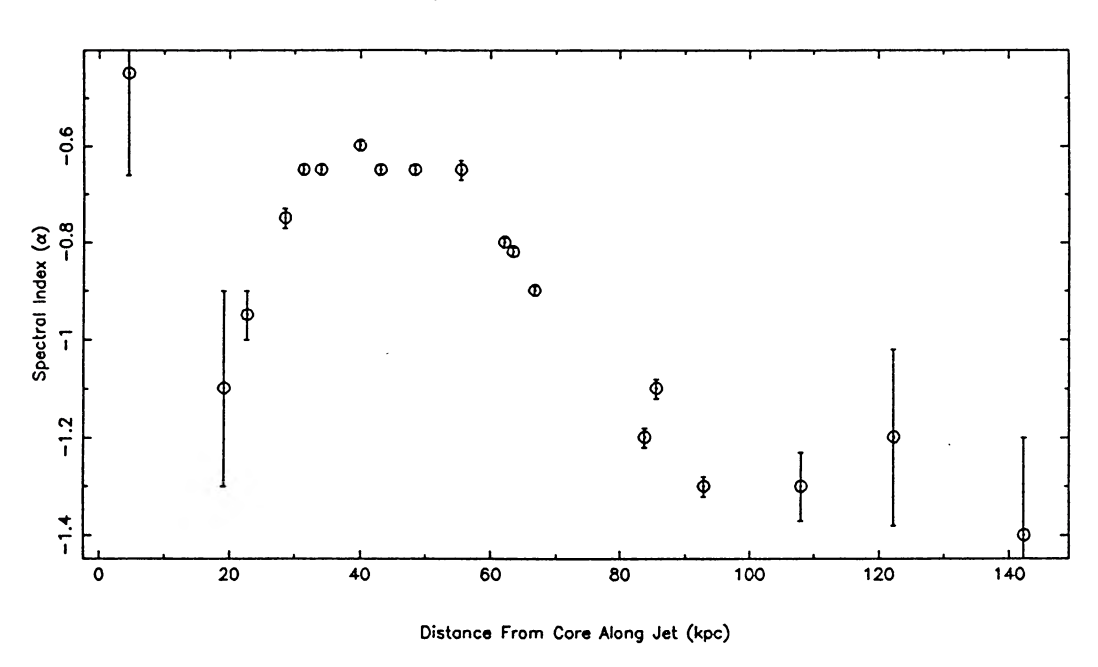
iii) Spectral Index and Minimum Pressure Analysis

For the most part, the spectral index is typical for WATs. The northern jet steepens from -0.5 to -0.6. Too few points in the southern jet survive blanking to evaluate α . The circular northern lobe has values between -0.7 and -0.9, while the extended tail flattens from these values. The edges of the tail range from -0.5 to -0.9, while the inner part is flatter, even to greater than zero. The amount of blanking in the inner part, however, reduces the confidence in these values. The southern lobe is mixed values, slightly steeper at the hot spots.

The positions of the slices used in the spectral and minimum pressure analysis are shown in Figure 57. The results of the minimum pressure analyses are given in Tables 21 and 22 and are shown in Figure 58. The spectral index is shown in Figure 59.

The smallest and faintest of the sources, 1826+747, presents its most interesting features at low resolution and shows almost no details at high resolution. As resolution is increased, a pattern of twists of increasing wavelength away

Spectral Index for the Northern Tail



Spectral Index for the Southern Tail

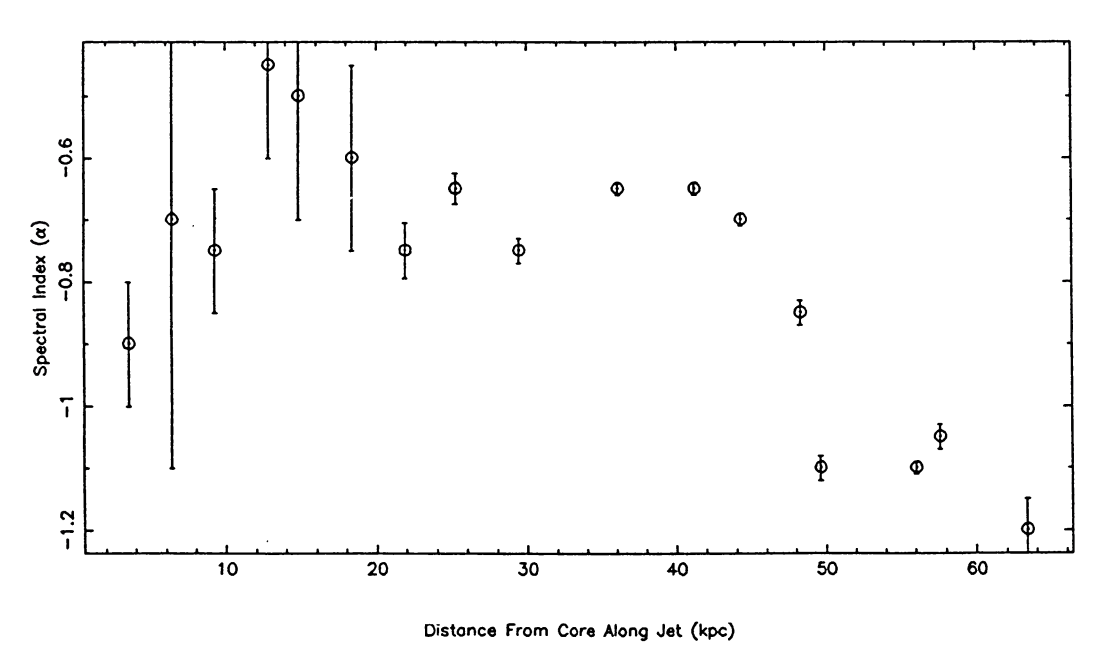


FIG. 52.—Spectral index values between 6 and 20 cm for 1433+553. Values were determined using estimated mean values from slices taken across the total intensity maps, at positions shown in Fig. 51.

TABLE 19 1433+553 Northern Tail Minimum Pressure

O'DONOGHUE, OWEN, AND EILEK

Number	Distance (kpc)	Diameter (kpc)	S per Beam (mJy per beam)	Volume (kpc ³)	Luminosity (10 ⁴¹ ergs s ⁻¹)	H _{min} (G)	$\frac{E_{\min}}{(10^{57} \text{ergs})}$	P_{\min} (dyne cm ⁻²)
2	2.7	2.07	0.21	4.4	1.6×10^{-2}	1.0×10^{-5}	2.7×10^{-3}	2.1×10^{-11}
3	4.4	1.10	0.13	1.2	9.8×10^{-3}	1.3×10^{-5}	1.2×10^{-3}	3.4×10^{-11}
4	7.5	1.11	0.13	1.3	9.7×10^{-3}	1.3×10^{-5}	1.2×10^{-3}	3.3×10^{-11}
5	9.1	0.38	0.03	1.5×10^{-1}	2.3×10^{-3}	1.6×10^{-5}	2.1×10^{-4}	4.9×10^{-11}
6	12.6	1.11	0.17	1.3	1.3×10^{-2}	1.4×10^{-5}	1.4×10^{-3}	3.9×10^{-11}
7	15.1	1.11	0.07	1.3	5.4×10^{-3}	1.1×10^{-5}	8.7×10^{-4}	2.3×10^{-11}
8	17.1	1.11	0.17	1.3	1.3×10^{-2}	1.4×10^{-5}	1.4×10^{-3}	3.9×10^{-11}
9	19.1	7.37	1.62	$9.4 \times 10^{+1}$	1.2×10^{-1}	7.7×10^{-6}	3.3×10^{-2}	1.2×10^{-11}
10	22.6	7.17	5.72	$9.0 \times 10^{+1}$	4.3×10^{-1}	1.1×10^{-5}	6.6×10^{-2}	2.5×10^{-11}
11	28.4	7.40	10.16	$9.5 \times 10^{+1}$	7.7×10^{-1}	1.3×10^{-2}	9.5×10^{-2}	3.4×10^{-11}
12	31.2	7.52	17.45	$9.8 \times 10^{+1}$	1.3	1.5×10^{-5}	1.3×10^{-1}	4.5×10^{-11}
13	33.9	6.46	21.95	$7.3 \times 10^{+1}$	1.7	1.8×10^{-5}	1.3×10^{-1}	6.1×10^{-11}
14	39.9	7.46	15.43	$9.7 \times 10^{+1}$	1.2	1.5×10^{-5}	1.2×10^{-1}	4.3×10^{-11}
15	43.0	7.07	14.41	$8.7 \times 10^{+1}$	1.1	1.5×10^{-5}	1.1×10^{-1}	4.3×10^{-11}
16	48.3	7.91	15.89	$1.1 \times 10^{+2}$	1.2	1.4×10^{-5}	1.3×10^{-1}	4.0×10^{-11}
17	55.4	10.26	17.54	$1.8 \times 10^{+2}$	1.3	1.3×10^{-5}	1.7×10^{-1}	3.2×10^{-11}
18	62.0	10.03	25.56	$3.5 \times 10^{+2}$	1.9	1.2×10^{-5}	2.8×10^{-1}	2.7×10^{-11}
19	63.4	9.94	24.74	$3.4 \times 10^{+2}$	1.9	1.2×10^{-5}	2.7×10^{-1}	2.7×10^{-11}
20	66.7	8.37	19.10	$2.4 \times 10^{+2}$	1.4	1.2×10^{-5}	2.0×10^{-1}	2.8×10^{-11}
22	83.7	11.07	14.62	4.3×10 ⁺²	1.1	9.4×10^{-6}	2.2×10^{-1}	1.8×10^{-11}
21	85.5	12.25	17.41	$5.2 \times 10^{+2}$	1.3	9.4×10^{-6}	2.7×10^{-1}	1.7×10^{-11}
23	92.8	19.50	18.15	$1.3 \times 10^{+3}$	1.4	7.3×10^{-6}	4.1×10^{-1}	1.0×10^{-11}
24	107.9	24.25	12.31	$2.0 \times 10^{+3}$	9.3×10^{-1}	5.7×10^{-6}	3.9×10^{-1}	6.5×10^{-12}
25	122.3	16.99	4.61	$1.0 \times 10^{+3}$	3.5×10^{-1}	5.3×10^{-6}	1.7×10^{-1}	5.6×10^{-12}
26	142.2	28.63	16.72	2.9×10 ⁺³	1.3	5.7×10^{-6}	5.4×10^{-1}	6.4×10^{-12}
27	149.8	25.93	3.75	$4.7 \times 10^{+3}$	2.8×10^{-1}	3.2×10^{-6}	2.8×10^{-1}	2.1×10^{-12}
28	170.4	16.08	1.08	$1.8 \times 10^{+3}$	8.1×10^{-2}	3.0×10^{-6}	9.2×10^{-2}	1.7×10^{-12}

TABLE 20 1433+553 SOUTHERN TAIL MINIMUM PRESSURE

Number	Distance (kpc)	Diameter (kpc)	S per Beam (mJy per beam)	Volume (kpc ³)	Luminosity (10 ⁴¹ ergs s ⁻¹)	H_{\min} (G)	E_{\min} (10 ⁵⁷ ergs)	P_{\min} (dyne cm ⁻²)
30	3.5	0.42	0.20	1.8×10^{-1}	1.4×10 ⁻²	2.5×10 ⁻⁵	6.8×10 ⁻⁴	1.3×10^{-11}
31	6.4	1.51	0.63	2.3	4.6×10^{-2}	1.7×10^{-5}	4.0×10^{-3}	5.8×10^{-11}
32	9.3	1.72	0.73	3.0	5.4×10^{-2}	1.7×10^{-5}	4.9×10^{-3}	5.5×10^{-11}
33	12.8	6.98	0.91	$5.0 \times 10^{+1}$	6.7×10^{-2}	7.9×10^{-6}	1.8×10^{-2}	1.2×10^{-11}
34	14.8	2.47	0.32	6.2	2.4×10^{-2}	1.1×10^{-5}	4.2×10^{-3}	2.3×10^{-11}
35	18.4	4.41	0.85	$2.0 \times 10^{+1}$	6.3×10^{-2}	1.0×10^{-5}	1.2×10^{-2}	2.0×10^{-11}
36	21.9	7.99	6.79	1.1×10 ⁺²	5.0×10^{-1}	1.1×10^{-5}	8.1×10^{-2}	2.5×10^{-11}
37	25.3	8.71	10.28	$1.3 \times 10^{+2}$	7.6×10^{-1}	1.2×10^{-5}	1.1×10^{-1}	2.9×10^{-11}
38	29.5	9.50	13.14	$1.6 \times 10^{+2}$	9.7×10^{-1}	1.2×10^{-5}	1.4×10^{-1}	3.0×10^{-11}
39	36.1	15.14	34.39	$4.0 \times 10^{+2}$	2.5	1.2×10^{-5}	3.6×10^{-1}	3.0×10^{-11}
40	41.2	14.50	65.71	$3.7 \times 10^{+2}$	4.8	1.5×10^{-5}	5.0×10^{-1}	4.6×10^{-11}
41	44.3	14.38	55.89	$3.6 \times 10^{+2}$	4.1	1.5×10^{-5}	4.5×10^{-1}	4.2×10^{-11}
42	48.3	17.26	56.08	$1.0 \times 10^{+3}$	4.1	1.1×10^{-5}	7.1×10^{-1}	2.3×10^{-11}
43	49.6	20.40	35.09	$1.4 \times 10^{+3}$	2.6	8.6×10^{-6}	6.2×10^{-1}	1.5×10^{-11}
44	56.1	23.68	11.11	$2.0 \times 10^{+3}$	8.2	1.1×10^{-5}	1.4	2.4×10^{-11}
45	57.6	24.19	71.19	$2.0 \times 10^{+3}$	5.2	9.5×10^{-6}	1.1	1.8×10^{-11}
46	63.4	21.33	17.03	3.2×10 ⁺³	1.3	5.6×10^{-6}	5.8×10^{-1}	6.2×10^{-12}



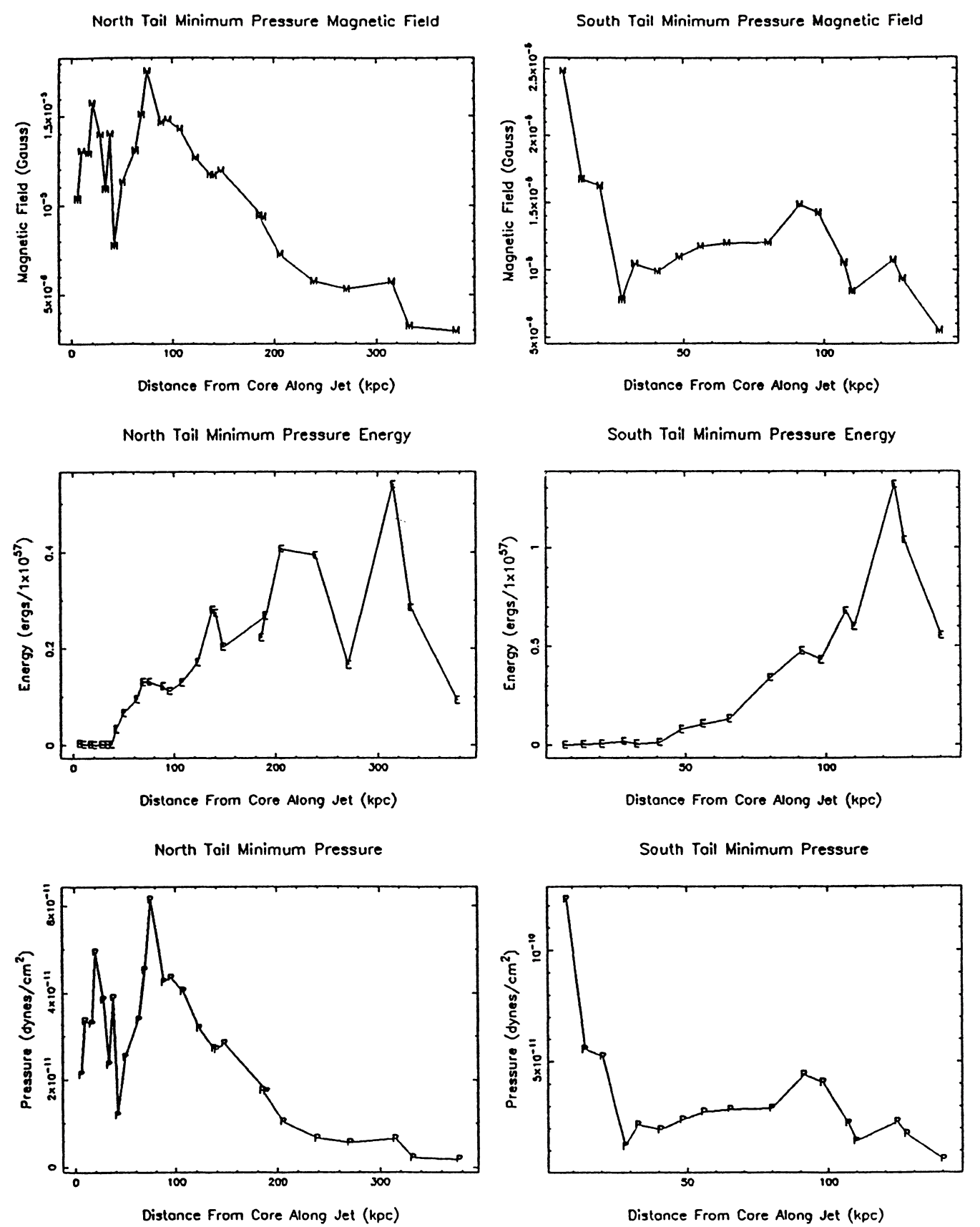


FIG. 53.—Estimates of the magnetic field, total energy (within one slice across the tail), and pressure, derived from minimum-pressure arguments, for the north and south tails of 1433+553. Values are given for slice positions shown in Fig. 51. Data are given in Tables 19 and 20.

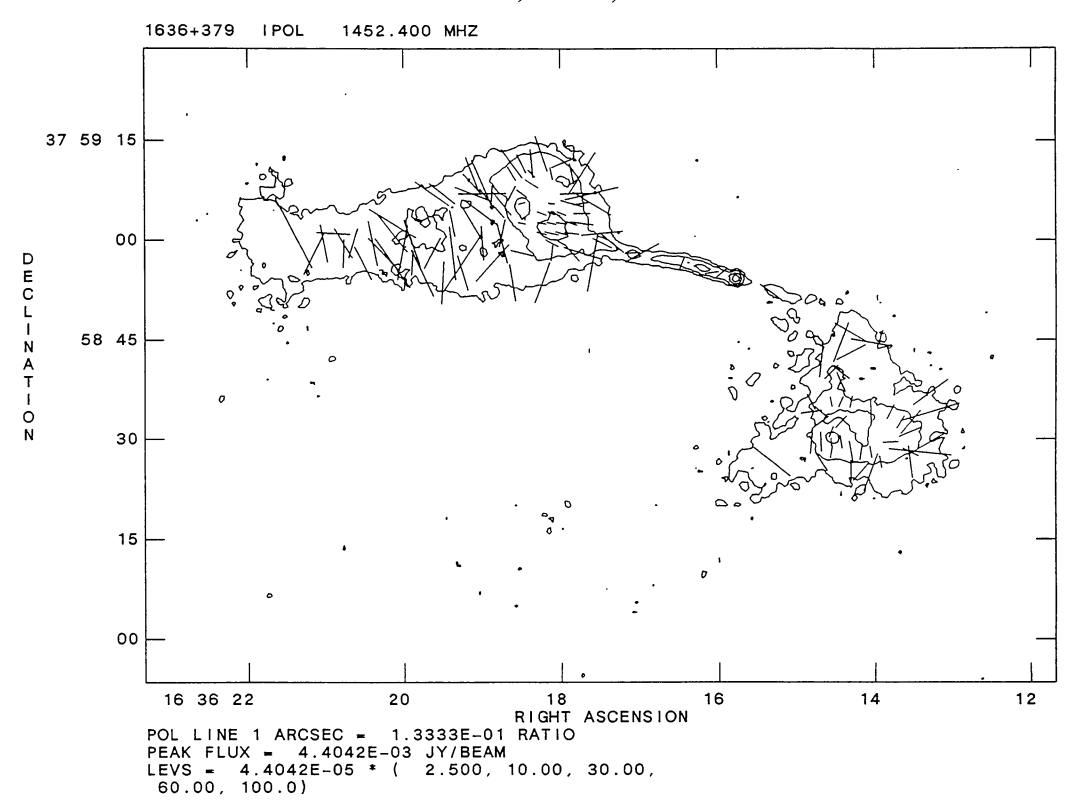


FIG. 56.—Polarization angles for 1636+379, uncorrected for Faraday rotation. Contours are those of the full resolution 20 cm image, and lengths of the vectors are proportional to the fractional polarization at 6 cm.

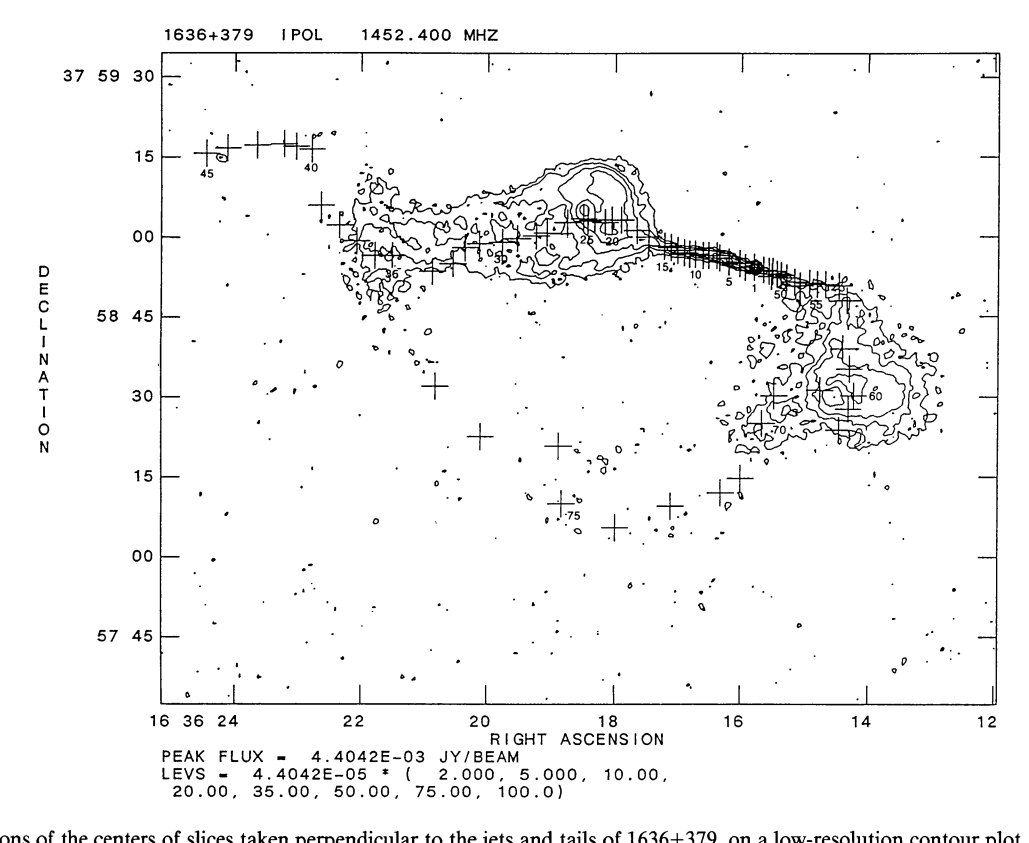


FIG. 57.—Positions of the centers of slices taken perpendicular to the jets and tails of 1636+379, on a low-resolution contour plot. Spectral indices and minimum pressure values for these slices are shown in Fig. 58 and 59.

TABLE 21 1636+379 Northern Tail Minimum Pressure

Number	Distance (kpc)	Diameter (kpc)	S per Beam (mJy per beam)	Volume (kpc³)	Luminosity (10 ⁴¹ ergs s ⁻¹)	H _{min} (G)	E_{\min} (10 ⁵⁷ ergs)	P_{\min} (dyne cm ⁻²)
2	4.7	0.56	0.28	3.5×10^{-1}	2.6×10^{-2}	2.6×10^{-5}	1.4×10^{-3}	1.3×10^{-10}
3	7.0	0.32	0.22	1.2×10^{-1}	2.0×10^{-2}	3.3×10^{-5}	7.5×10^{-4}	2.1×10^{-10}
4	9.7	0.72	0.50	5.9×10^{-1}	4.7×10^{-2}	2.6×10^{-5}	2.4×10^{-3}	1.4×10^{-10}
5	12.4	0.78	0.80	7.0×10^{-1}	7.4×10^{-2}	2.9×10^{-5}	3.4×10^{-3}	1.6×10^{-10}
6	16.9	0.69	0.47	5.4×10^{-1}	4.4×10^{-2}	2.6×10^{-5}	2.2×10^{-3}	1.4×10^{-10}
7	18.4	0.42	0.30	2.1×10^{-1}	2.8×10^{-2}	3.1×10^{-5}	1.1×10^{-3}	1.9×10^{-10}
8	22.1	1.27	0.59	1.8	5.5×10^{-2}	2.0×10^{-5}	4.3×10^{-3}	7.9×10^{-11}
9	24.6	0.98	0.41	1.1	3.8×10^{-2}	2.1×10^{-5}	2.8×10^{-3}	8.6×10^{-11}
10	28.3	1.53	0.53	2.7	4.9×10^{-2}	1.7×10^{-5}	4.7×10^{-3}	6.0×10^{-11}
11	31.1	1.64	0.44	3.1	4.1×10^{-2}	1.6×10^{-5}	4.5×10^{-3}	5.0×10^{-11}
12	33.3	1.04	0.44	2.1	2.7×10^{-2}	1.6×10^{-5}	3.0×10^{-3}	3.0×10 4.9×10^{-11}
13	36.8	1.34	0.29	2.1	2.7×10^{-2} 2.9×10^{-2}	1.6×10^{-5}	3.0×10^{-3} 3.1×10^{-3}	5.1×10^{-11}
14	40.0	1.90	0.73	4.2	6.8×10^{-2}	1.0×10^{-5} 1.7×10^{-5}	6.9×10^{-3}	5.6×10^{-11}
15	43.0	4.57	1.78	$5.1 \times 10^{+1}$	1.7×10^{-1}	1.7×10^{-5} 1.1×10^{-5}	3.3×10^{-2}	2.2×10^{-11}
13	45.0	7.57	1.76	J.1 × 10	1.7 × 10	1.1 \ 10	3.3 \ 10	
16	51.7	12.77	7.91	$4.0 \times 10^{+2}$	7.4×10^{-1}	9.0×10^{-6}	1.9×10^{-1}	1.6×10^{-11}
17	58.4	18.65	14.50	$8.5 \times 10^{+2}$	1.4	8.6×10^{-6}	3.7×10^{-1}	1.5×10^{-11}
19	66.1	24.80	36.01	$1.5 \times 10^{+3}$	3.4	9.5×10^{-6}	7.9×10^{-1}	1.8×10^{-11}
20	70.1	26.39	45.39	$1.7 \times 10^{+3}$	4.2	9.8×10^{-6}	9.5×10^{-1}	1.9×10^{-11}
21	74.3	27.72	46.25	$1.9 \times 10^{+3}$	4.3	9.6×10^{-6}	1.0	1.8×10^{-11}
22	79.0	29.69	41.98	$2.1 \times 10^{+3}$	3.9	9.0×10^{-6}	1.0	1.0×10^{-11}
23	81.7	27.36	39.41	$1.8 \times 10^{+3}$	3.7	9.2×10^{-6}	9.1×10^{-1}	1.7×10^{-11}
24	83.5	25.64	35.78	$1.6 \times 10^{+3}$	3.3	9.3×10^{-6}	8.1×10^{-1}	1.7×10^{-11}
26	92.2	35.63	20.41	$3.1 \times 10^{+3}$	1.9	6.6×10^{-6}	7.8×10^{-1}	8.6×10^{-12}
27	100.9	40.51	17.39	$4.0 \times 10^{+3}$	1.6	5.8×10^{-6}	8.0×10^{-1}	6.8×10^{-12}
28	106.1	37.32	32.44	$6.8 \times 10^{+3}$	3.0	6.0×10^{-6}	1.4	7.2×10^{-12}
29	115.3	35.68	26.79	$6.2 \times 10^{+3}$	2.5	5.8×10^{-6}	1.2	6.7×10^{-12}
30	121.7	33.18	23.96	$5.4 \times 10^{+3}$	2.2	5.9×10^{-6}	1.1	6.9×10^{-12}
31	133.6	26.99	21.75	$3.6 \times 10^{+3}$	2.0	6.4×10^{-6}	8.6×10^{-1}	8.2×10^{-12}
32	140.6	23.52	20.36	$2.7 \times 10^{+3}$	1.9	6.8×10^{-6}	7.4×10^{-1}	9.3×10^{-12}
33	146.1	22.56	20.49	$2.5 \times 10^{+3}$	1.9	7.0×10^{-6}	7.1×10^{-1}	9.8×10^{-12}
34	155.0	26.13	24.08	$3.3 \times 10^{+3}$	2.2	6.7×10^{-6}	8.9×10^{-1}	9.1×10^{-12}
35	173.4	44.29	36.14	$9.6 \times 10^{+3}$	3.4	5.6×10^{-6}	1.8	6.3×10^{-12}
36	181.1	46.76	35.43	$1.1 \times 10^{+4}$	3.3	5.4×10^{-6}	1.8	5.8×10^{-12}
37	190.0	47.89	25.21	$1.1 \times 10^{+4}$	2.3	4.8×10^{-6}	1.5	4.7×10^{-12}
38	200.2	51.05	23.33	2.5×10 ⁺⁴	2.2	3.7×10^{-6}	2.1	2.8×10^{-12}
39	213.4	59.63	10.23	$3.5 \times 10^{+4}$	9.5×10^{-1}	2.7×10^{-6}	1.5	1.5×10^{-12}
40	239.5	30.95	4.66	$9.3 \times 10^{+3}$	4.3×10^{-1}	3.1×10^{-6}	5.4×10^{-1}	2.0×10^{-12}
41	247.4	16.17	1.91	$2.5 \times 10^{+3}$	1.8×10^{-1}	3.1×10^{-6}	1.9×10^{-1}	2.5×10^{-12}
43	265.8	23.07	1.78	$5.2 \times 10^{+3}$	1.7×10^{-1}	2.8×10^{-6}	2.4×10^{-1}	1.6×10^{-12}
42	278.5	16.54	1.61	$2.7 \times 10^{+3}$	1.5×10^{-1}	3.3×10^{-6}	1.7×10^{-1}	2.2×10^{-12}
44	279.5	30.90	2.45	$9.3 \times 10^{+3}$	2.3×10^{-1}	2.6×10^{-6}	3.7×10^{-1}	1.4×10^{-12}
45	289.6	53.23	3.20	$2.8 \times 10^{+4}$	3.0×10^{-1}	2.0×10^{-6} 2.1×10^{-6}	6.9×10^{-1}	8.5×10^{-13}

O'DONOGHUE, OWEN, AND EILEK TABLE 22

1ABLE 22 1636+379 SOUTHERN TAIL MINIMUM PRESSURE

Number	Distance (kpc)	Diameter (kpc)	S per Beam (mJy per beam)	Volume (kpc ³)	Luminosity (10 ⁴¹ ergs s ⁻¹)	H_{\min} (G)	E_{\min} (10 ⁵⁷ ergs)	P_{\min} (dyne cm ⁻²)
59	10.4	9.97	0.87	2.4×10 ⁺²	8.1×10^{-2}	5.5×10 ⁻⁶	4.3×10 ⁻²	6.1×10^{-12}
60	15.6	8.02	1.53	$1.6 \times 10^{+2}$	1.4×10^{-1}	7.4×10^{-6}	5.0×10^{-2}	1.1×10^{-11}
61	24.8	14.77	3.14	5.3×10 ⁺²	2.9×10^{-1}	6.4×10^{-6}	1.3×10^{-1}	8.1×10^{-12}
62	37.5	34.69	7.68	$2.9 \times 10^{+3}$	7.2×10^{-1}	5.0×10^{-6}	4.4×10^{-1}	5.1×10^{-12}
63	61.1	36.85	19.35	$3.3 \times 10^{+3}$	1.8	6.3×10^{-6}	7.8×10^{-1}	8.0×10^{-12}
64	69.1	38.53	30.90	$3.6 \times 10^{+3}$	2.9	7.1×10^{-6}	1.1	1.0×10^{-11}
65	81.7	39.83	42.00	$3.9 \times 10^{+3}$	3.9	7.6×10^{-6}	1.3	1.1×10^{-11}
68	85.9	27.67	44.96	$3.7 \times 10^{+3}$	4.2	7.8×10^{-6}	1.3	1.2×10^{-11}
66	88.4	39.66	35.32	$3.8 \times 10^{+3}$	3.3	7.2×10^{-6}	1.2	1.0×10^{-11}
67	99.4	68.34	18.84	$1.1 \times 10^{+4}$	1.8	4.4×10^{-6}	1.3	3.9×10^{-12}
69	107.8	33.23	21.38	$5.4 \times 10^{+3}$	2.0	5.7×10^{-6}	1.0	6.4×10^{-12}
70	114.3	27.24	13.83	$3.6 \times 10^{+3}$	1.3	5.6×10^{-6}	6.7×10^{-1}	6.3×10^{-12}
71	146.3	86.80	14.42	3.7×10 ⁺⁴	1.3	2.9×10 ⁻⁶	1.9	1.7×10^{-12}
72		76.88	17.08	$5.8 \times 10^{+4}$	1.6	2.7×10^{-6}	2.5	1.5×10^{-12}
73		67.12	14.58	$4.4 \times 10^{+4}$	1.4	2.8×10^{-6}	2.0	1.6×10^{-12}
74		81.88	12.59	$6.5 \times 10^{+4}$	1.2	2.4×10^{-6}	2.2	1.1×10^{-12}
75		50.59	6.26	$2.5 \times 10^{+4}$	5.8×10^{-1}	2.6×10^{-6}	9.7×10^{-1}	1.3×10^{-12}
76	258.1	37.72	3.66	1.4×10 ⁺⁴	3.4×10^{-1}	2.6×10^{-6}	5.6×10^{-1}	1.4×10^{-12}
77		49.79	2.95	$2.4 \times 10^{+4}$	2.7×10^{-1}	2.1×10^{-6}	6.2×10^{-1}	8.8×10^{-13}
78		24.37	2.58	$5.8 \times 10^{+3}$	2.4×10^{-1}	3.0×10^{-6}	3.1×10^{-1}	1.8×10^{-12}

from the core can be observed, but they are of low surface brightness and are thus easily lost to the noise at high resolution.

1826+747 is identified with the cluster A2306 which is classified a Bautz-Morgan type II by Simon (1978). The radio sources near its center were identified on a WSRT map by G. de Bruyn. The WAT is close to the cluster center; the close double to the northwest has no optical identification and thus may be a background source (Harris et al. 1980), and another bright source just to the northwest (not shown on the images here; see Harris, Kapahi, and Ekers 1980 for a contour plot) is close to several galaxies and thus may be identified with the cluster. Radio observations of the WAT and its companions include those by Owen (1974a) (1400 MHz), and Owen (1975b) (2695 MHz), Rudnick and Owen (1977) (2695 MHz and 8085 MHz, 1977), who identify the WAT as an intermediate-angle source, and Harris, Kapahi, and Ekers (1980) (1415 MHz).

i) Source Structure

The total intensity image of the source at 20 cm, including its western companion, is shown in Figure 60 (Plate 68). The optical image of the galaxy is shown in Figure 61 (Plate 69), with the radio contours overlaid.

ii) Polarization

In polarized intensity, only the bright "moustache" close to the core and part of the first twist in the eastern tail are seen at 20 cm, and not even the first twist is seen at 6 cm. Beam depolarization is detected at both frequencies. In fractional polarization the tails are 5%-30% polarized in the centers. This increases to over 40% on the edges. Vectors representing the fractional polarization at 6 cm are shown in Figure 62.

iii) Spectral Index and Minimum Pressure Analysis

Because of low surface brightness, only a patchy part of the first twist is seen along with the moustache, and these are mottled. There does seem to be a slight steepening trend, from values of -0.5 to -0.6 at the beginnings of the tails to -0.7 to -0.8 at in the first twists.

The positions of the slice centers which were used in the spectral index and minimum pressure analyses are shown in Figure 63. The spectral index is shown in Figure 64. The results of the minimum pressure analyses are shown in Figure 65 and are presented in Tables 23 and 24.

Unique in this survey in that one tail bends while the other goes straight, the morphology source is actually quite similar to the previously studied sources, 3C 465 (Eilek et al. 1984) and 1919+379 (Burns 1981), as well as 0836+290. It also displays flattening and edge brightening of the western tail, indicating a boundary. Adjacent to the eastern tail there is low surface brightness material similar to the eastern tail of 1636+379. The most interesting feature of this source, however, is the appearance of a pair of arcs in the bright eastern lobe (just before the bend).

A2462 has been classified a Bautz-Morgan type II by Leir and van den Bergh (1977). Included in the Parkes survey, the

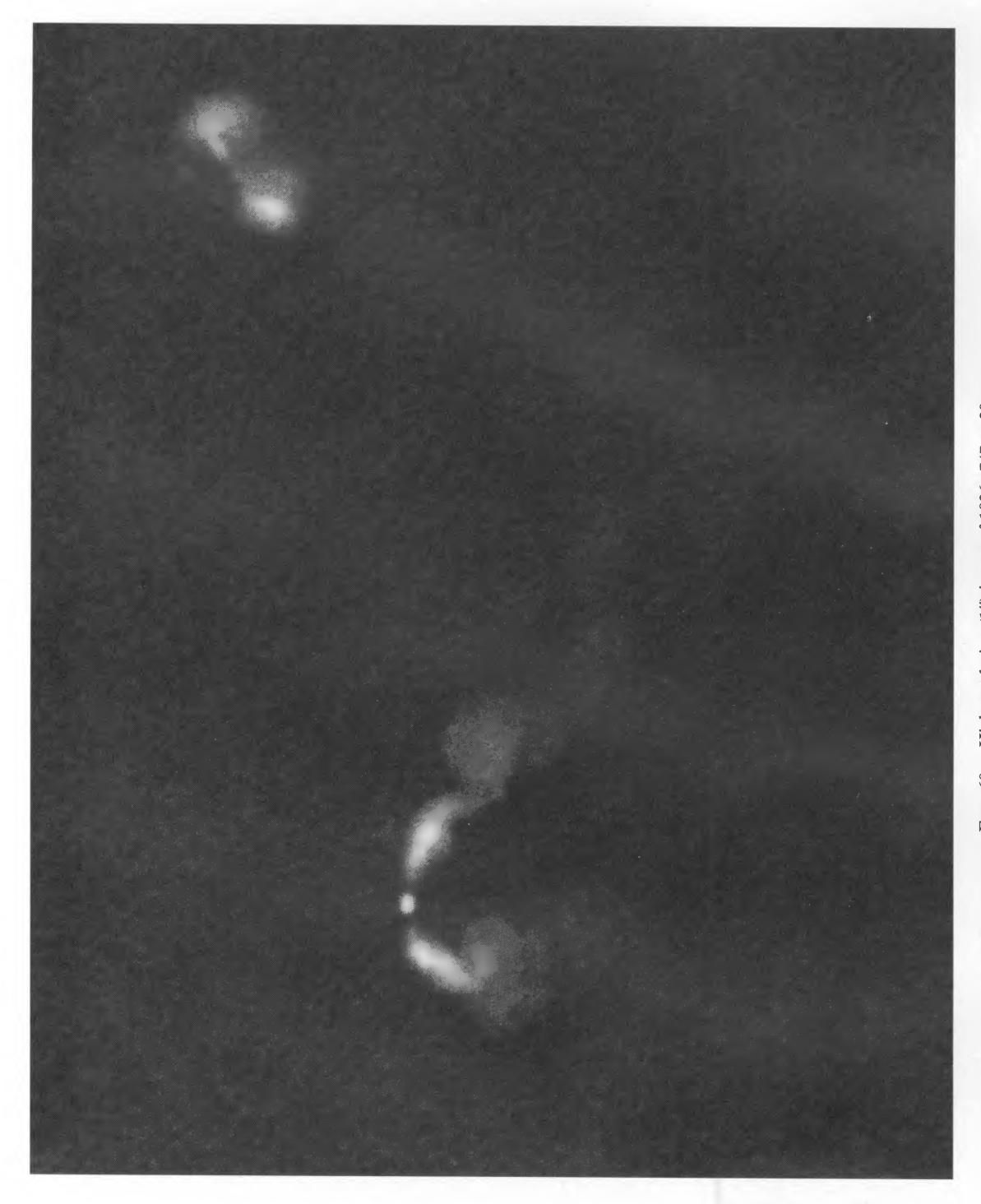


Fig. 60.—High-resolution (1") image of 1826+747 at 20 cm

O'DONOGHUE, OWEN, AND EILEK (see 72, 120)

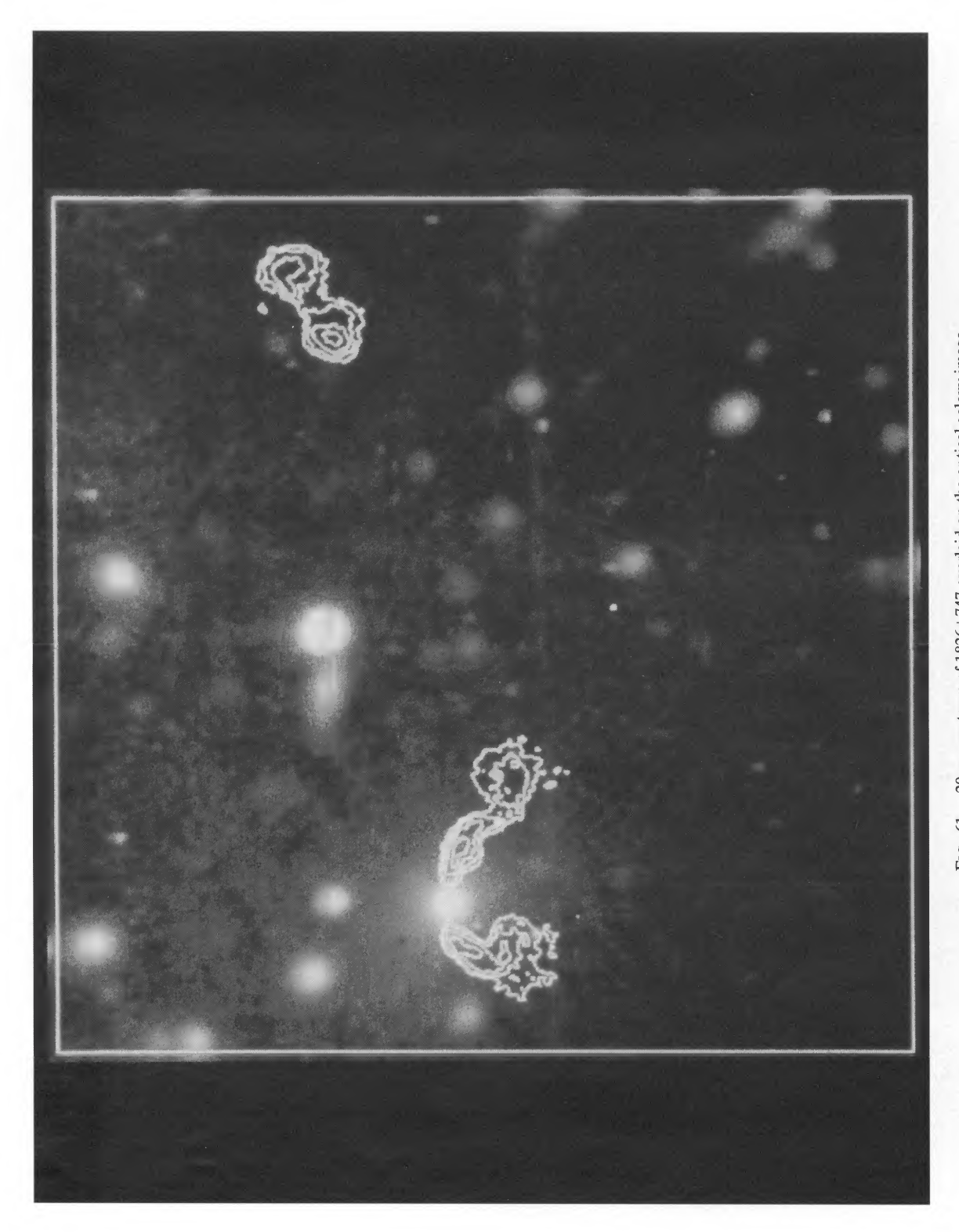
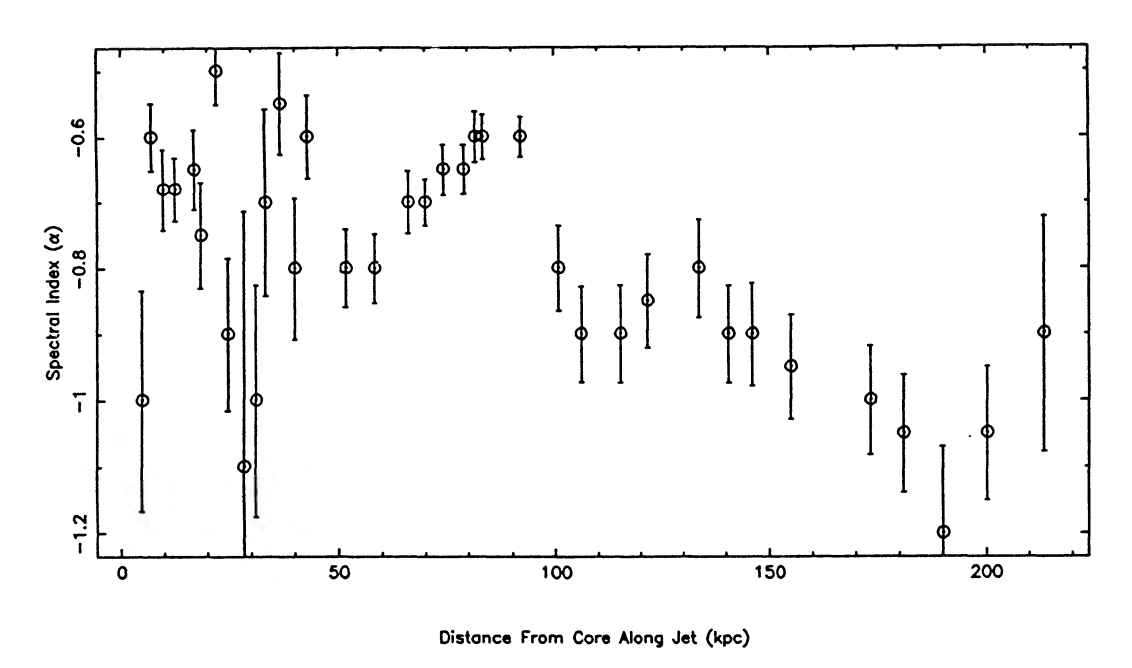
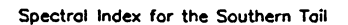


Fig. 61.—20 cm contours of 1826+747 overlaid on the optical galaxy image

O'DONOGHUE, OWEN, AND EILEK (see 72, 120)

Spectral Index for the Northern Tail





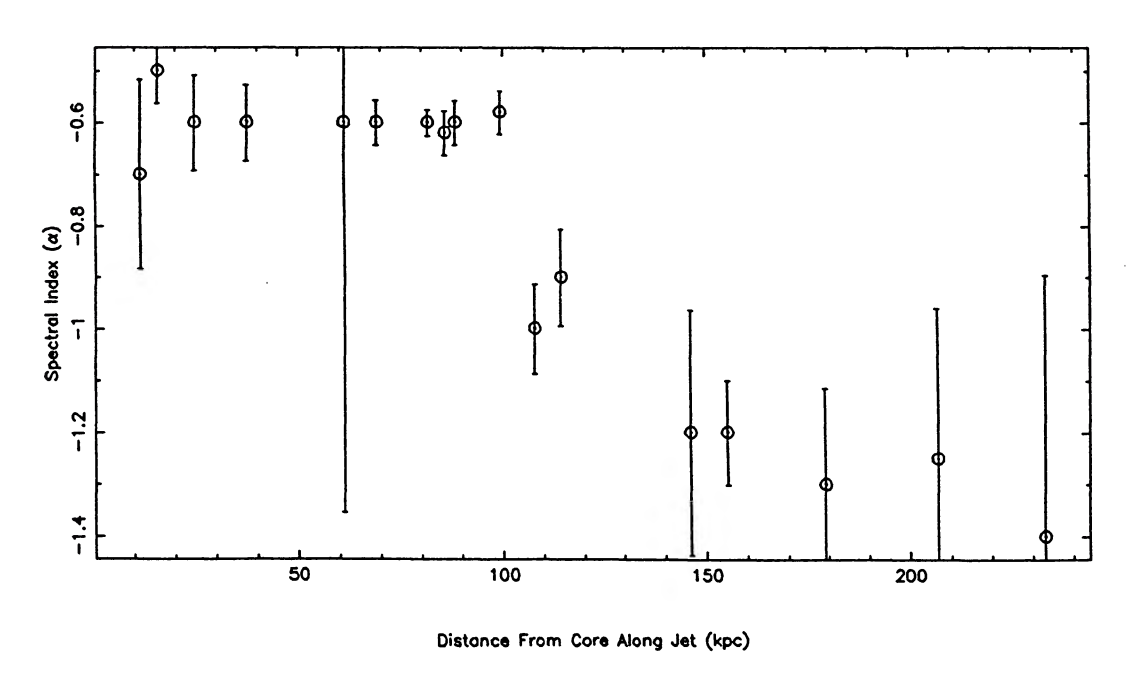


FIG. 58.—Spectral index values between 6 and 20 cm for 1636+379. Values were determined using estimated mean values from slices taken across the total intensity maps, at positions shown in Fig. 57.

1990ApJS...72...750

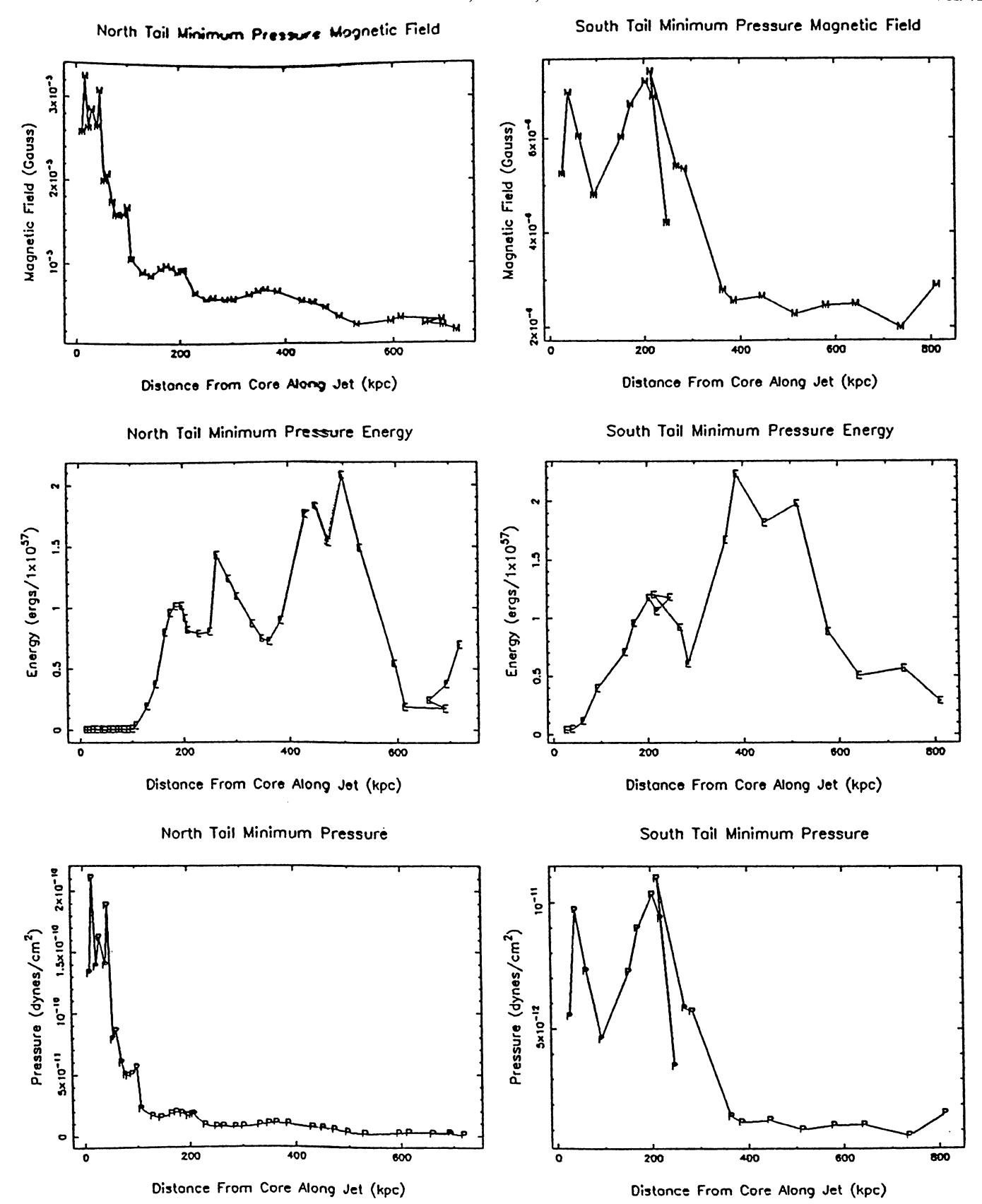


FIG. 59.—Estimates of the magnetic field, total energy (within one slice across the tail) and pressure, derived from minimum pressure arguments, for the north and south tails of 1636+379. Values are given for slice positions shown in Fig. 57. Data are given in Tables 21 and 22.

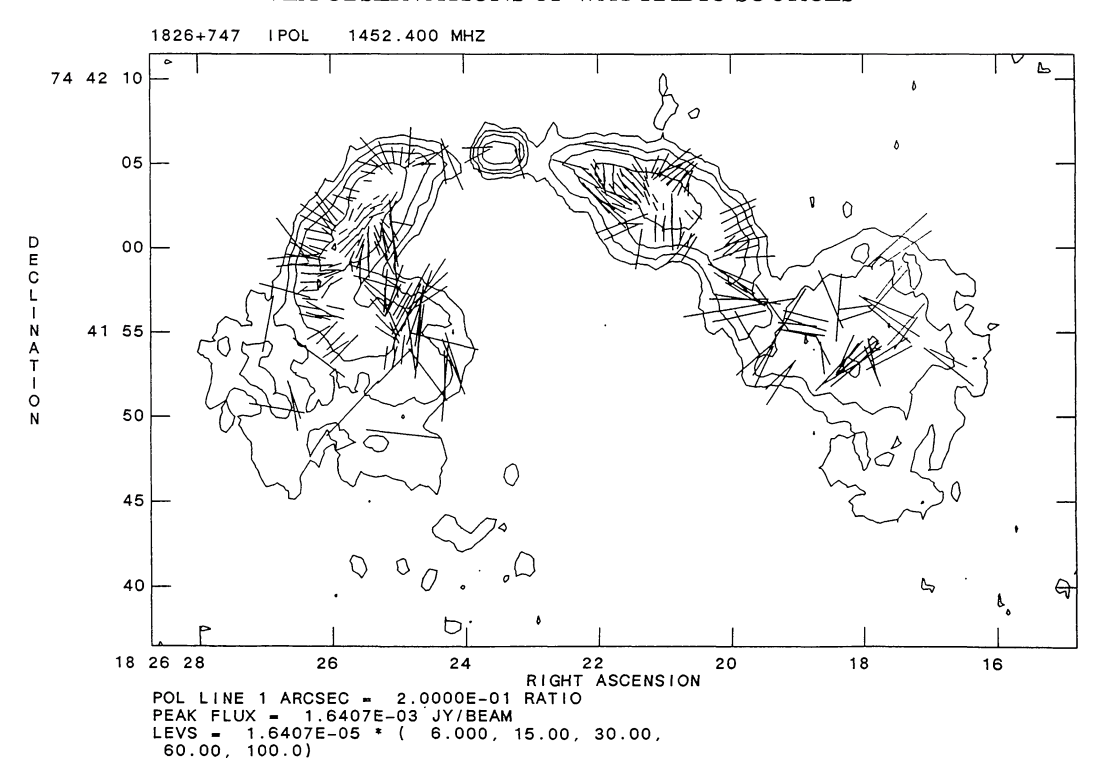


FIG. 62.—Polarization vectors for 1828+747, uncorrected for Faraday rotation. Contours are those of the full resolution 20 cm image, and lengths of the vectors are proportional to the fractional polarization at 6 cm.

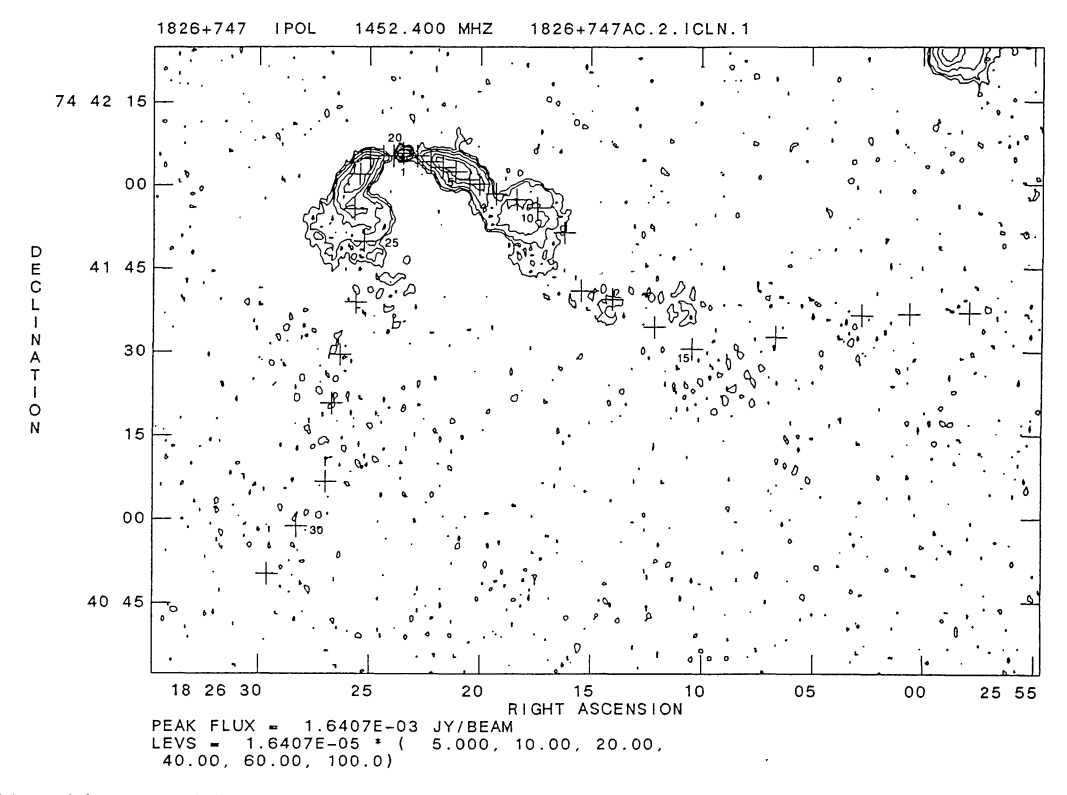
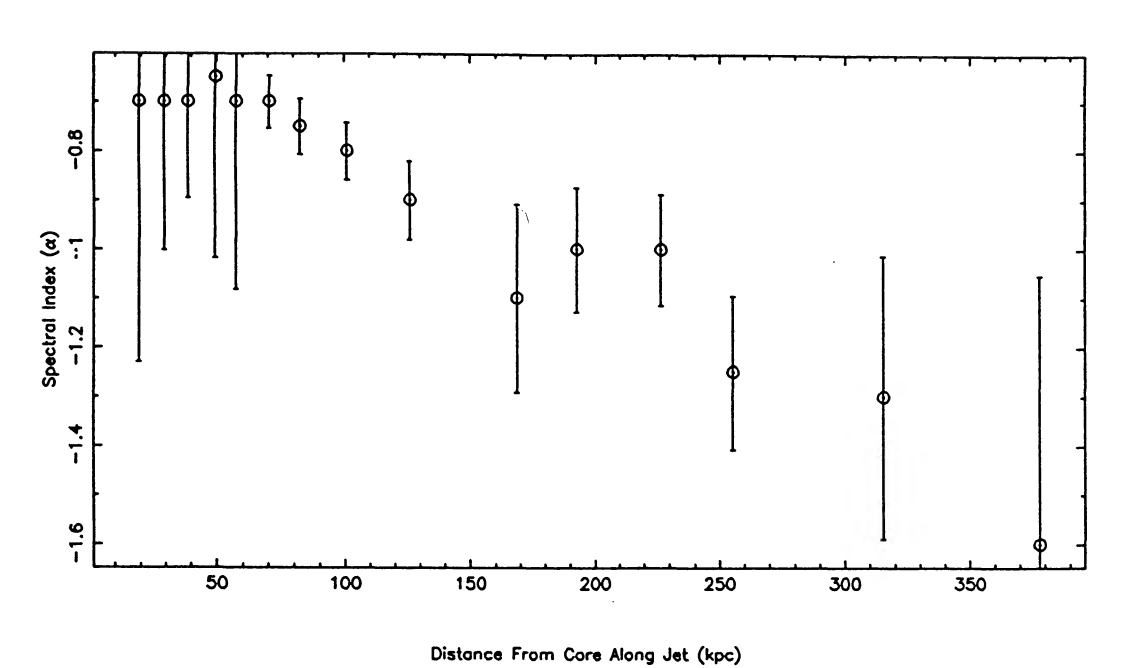


FIG. 63.—Positions of the centers of slices taken perpendicular to the jets and tails of 1826+747, on a low-resolution contour plot. Spectral indices and minimum pressure values for these slices are shown in Figs. 64 and 65.





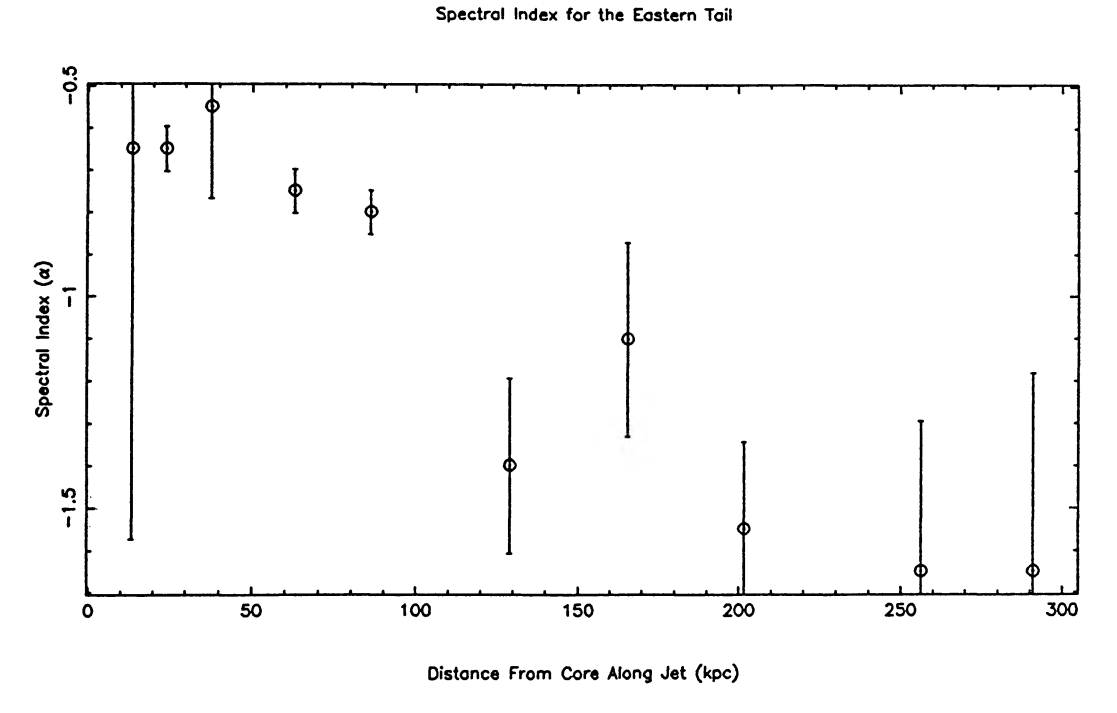


FIG. 64.—Spectral index values between 6 and 20 cm for 1826+747. Values were determined using estimated mean values from slices taken across the total intensity maps, at positions shown in Fig. 63.

1990ApJS...72...750

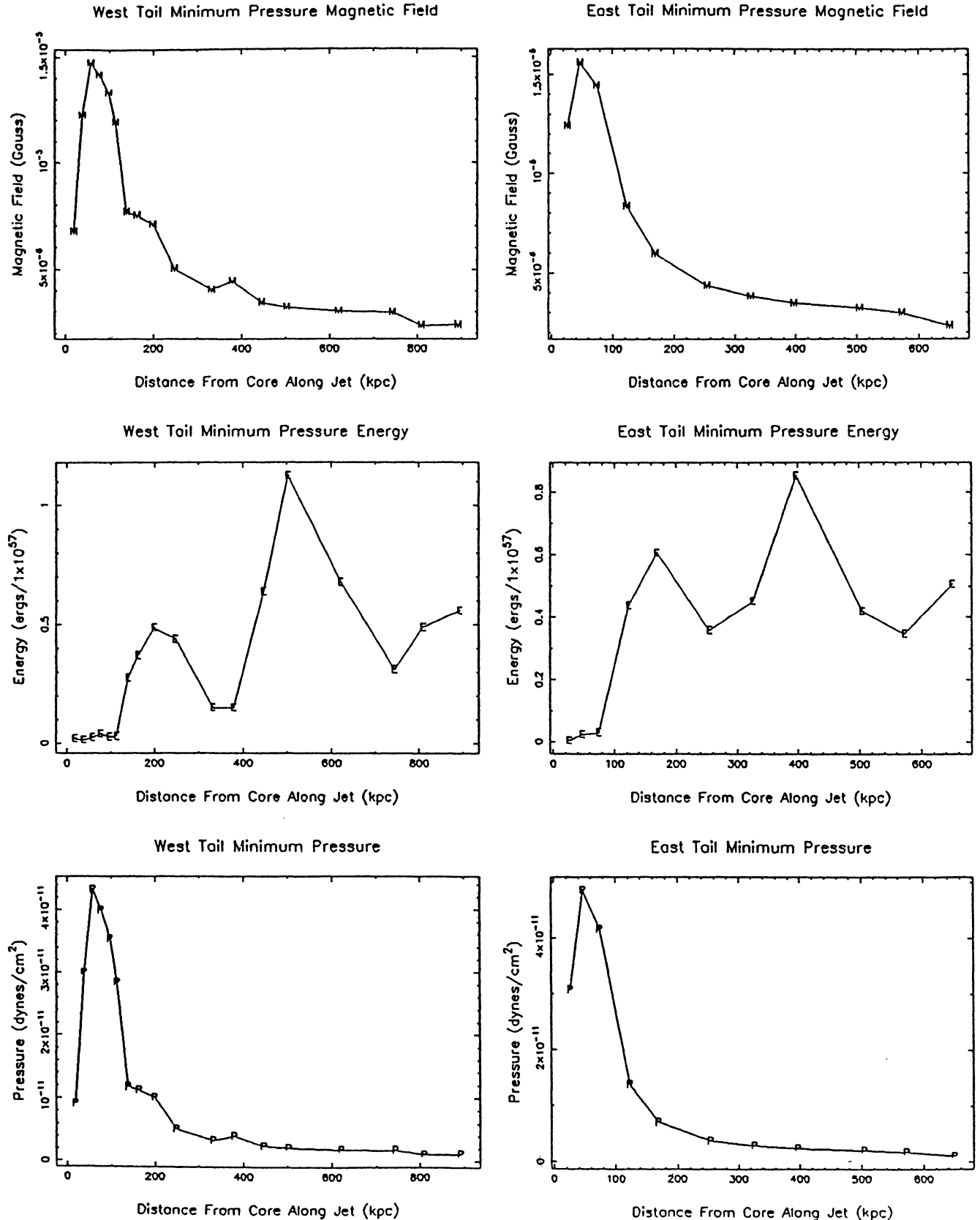


FIG. 65.—Estimates of the magnetic field, total energy (within one slice across the tail), and pressure, derived from minimum pressure arguments, for the west and east tails of 1826+747. Values are given for slice positions shown in Fig. 63. Data are given in Tables 23 and 24.

O'DONOGHUE, OWEN, AND EILEK TABLE 23

1826+747 Eastern Tail Minimum Pressure

Number	Distance (kpc)	Diameter (kpc)	S per Beam (mJy per beam)	Volume (kpc ³)	Luminosity (10 ⁴¹ ergs s ⁻¹)	H _{min} (G)	$\frac{E_{\min}}{(10^{57}\mathrm{ergs})}$	P_{\min} (dyne cm ⁻²)
21	13.4	2.05	0.44	3.8	2.4×10^{-2}	1.2×10 ⁻⁵	3.4×10^{-3}	3.1×10^{-11}
22	24.0	4.23	4.24	$1.6 \times 10^{+1}$	2.3×10^{-1}	1.6×10^{-5}	2.3×10^{-2}	4.9×10^{-11}
23	37.6	5.17	4.81	$2.4 \times 10^{+1}$	2.6×10^{-1}	1.4×10^{-5}	2.9×10^{-2}	4.2×10^{-11}
24	62.6	13.17	31.35	$1.1 \times 10^{+3}$	1.7	8.3×10^{-6}	4.4×10^{-1}	1.4×10^{-11}
25	85.8	21.62	26.49	$2.9 \times 10^{+3}$	1.4	6.0×10^{-6}	6.1×10^{-1}	7.1×10^{-12}
26	129.0	22.74	9.73	3.2×10 ⁺³	5.2×10^{-1}	4.4×10^{-6}	3.6×10^{-1}	3.8×10^{-12}
27	165.6	29.18	10.10	$5.3 \times 10^{+3}$	5.4×10^{-1}	3.8×10^{-6}	4.5×10^{-1}	2.9×10^{-12}
28	201.6	31.26	16.44	$1.2 \times 10^{+4}$	8.8×10^{-1}	3.5×10^{-6}	8.5×10^{-1}	2.4×10^{-12}
29	256.2	23.65	7.19	$6.9 \times 10^{+3}$	3.9×10^{-1}	3.2×10^{-6}	4.2×10^{-1}	2.1×10^{-12}
30	291.0	23.20	5.31	$6.7 \times 10^{+3}$	2.8×10^{-1}	3.0×10^{-6}	3.5×10^{-1}	1.8×10^{-12}
31	330.0	36.04	5.33	1.6×10 ⁺⁴	2.9×10^{-1}	2.3×10^{-6}	5.1×10^{-1}	1.1×10^{-12}

TABLE 24 1826+747 Western Tail Minimum Pressure

Number	Distance (kpc)	Diameter (kpc)	S per Beam (mJy per beam)	Volume (kpc ³)	Luminosity (10 ⁴¹ ergs s ⁻¹)	H_{\min} (G)	$\frac{E_{\min}}{(10^{57}\mathrm{ergs})}$	P_{\min} (dyne cm ⁻²)
2	9.6	8.99	0.97	7.3×10 ⁺¹	5.0×10^{-2}	6.7×10 ⁻⁶	1.9×10^{-2}	9.1×10^{-12}
3	19.3	4.27	1.77	$1.6 \times 10^{+1}$	9.1×10^{-2}	1.2×10^{-5}	1.4×10^{-2}	3.0×10^{-11}
4	29.3	4.65	3.99	$1.9 \times 10^{+1}$	2.0×10^{-1}	1.5×10^{-5}	2.5×10^{-2}	4.3×10^{-11}
5	38.8	6.15	6.08	$3.4 \times 10^{+1}$	3.1×10^{-1}	1.4×10^{-5}	4.0×10^{-2}	4.0×10^{-11}
6	49.4	5.37	3.75	$2.6 \times 10^{+1}$	1.9×10^{-1}	1.3×10^{-5}	2.7×10^{-2}	3.5×10^{-11}
7	57.7	6.31	3.52	$3.6 \times 10^{+1}$	1.8×10^{-1}	1.2×10^{-5}	3.0×10^{-2}	2.8×10^{-11}
8	70.7	11.37	16.67	$8.0 \times 10^{+2}$	8.5×10^{-1}	7.7×10^{-6}	2.7×10^{-1}	1.2×10^{-11}
9	82.9	13.48	21.76	$1.1 \times 10^{+3}$	1.1	7.5×10^{-6}	3.7×10^{-1}	1.1×10^{-11}
10	101.4	16.29	26.15	$1.6 \times 10^{+3}$	1.3	7.1×10^{-6}	4.8×10^{-1}	1.0×10^{-11}
11	126.2	21.84	14.14	$2.9 \times 10^{+3}$	7.2×10^{-1}	5.0×10^{-6}	4.4×10^{-1}	5.1×10^{-12}
12	168.7	15.90	3.47	$1.6 \times 10^{+3}$	1.8×10^{-1}	4.0×10^{-6}	1.5×10^{-1}	3.3×10^{-12}
13	192.6	14.48	3.99	$1.3 \times 10^{+3}$	2.0×10^{-1}	4.4×10^{-6}	1.5×10^{-1}	3.9×10^{-12}
14	226.6	27.36	11.66	$9.3 \times 10^{+3}$	6.0×10^{-1}	3.4×10^{-6}	6.4×10^{-1}	2.4×10^{-12}
15	255.2	38.76	18.55	$1.9 \times 10^{+4}$	9.5×10^{-1}	3.2×10^{-6}	1.1	2.1×10^{-12}
16	315.2	31.98	10.21	1.3×10 ⁺⁴	5.2×10^{-1}	3.0×10^{-6}	6.8×10^{-1}	1.8×10^{-12}
17	377.8	22.03	4.55	$6.0 \times 10^{+3}$	2.3×10^{-1}	3.0×10^{-6}	3.1×10^{-1}	1.8×10^{-12}
18	410.9	34.98	5.00	$1.5 \times 10^{+4}$	2.6×10^{-1}	2.3×10^{-6}	4.9×10^{-1}	1.1×10^{-12}
19	453.2	36.95	5.84	$1.7 \times 10^{+4}$	3.0×10^{-1}	2.4×10^{-6}	5.6×10^{-1}	1.1×10^{-12}

radio source has been studied by Shimmins, Manchester, and Harris (1969). Hunstead (1972) identifies the radio position at 408 MHz, Owen (1974a, 1975a) reports on observations at 1400 MHz, and Tabara and Inuoe (1980) give details at 6, 11.1, and 21.1 cm. The parent galaxy is also included in the discussion of multiple nuclei by Hoessel and Schneider (1985).

i) Source Structure

The 20 cm image is presented in Figure 66 (Plate 70). Two bright crescents are apparent in the eastern lobe. These are only about 20% brighter than the rest of the lobe, but stand out by their repeated morphology. They appear to be a pair of bubbles expanding away from the jet, as though the jet has bursts of material or energy flux. This source is very similar in appearance to the western tail of Her A that Dreher and Feigelson (1984) have examined. They conclude that variations in the central engine are the simplest interpretation. Since it is still debated whether the jets are constant or "flip-flop" (e.g., Rudnick 1984), this source may prove important as a probe of jet consistency. Higher fidelity images may also reveal structures similar to knot A in M 87 (Owen et al. 1989) with shock-like and filamentary structures. The radio contours are shown overlaid on the optical galaxy image in Figure 67 (Plate 71).

ii) Polarization

Interesting features not apparent in the total intensity images are revealed in the polarized intensity at 20 cm. Figure 68 (Plate 72) shows the fractional polarization at 20 cm. In the western tail, there are a pair of arcs in the initial broaden-

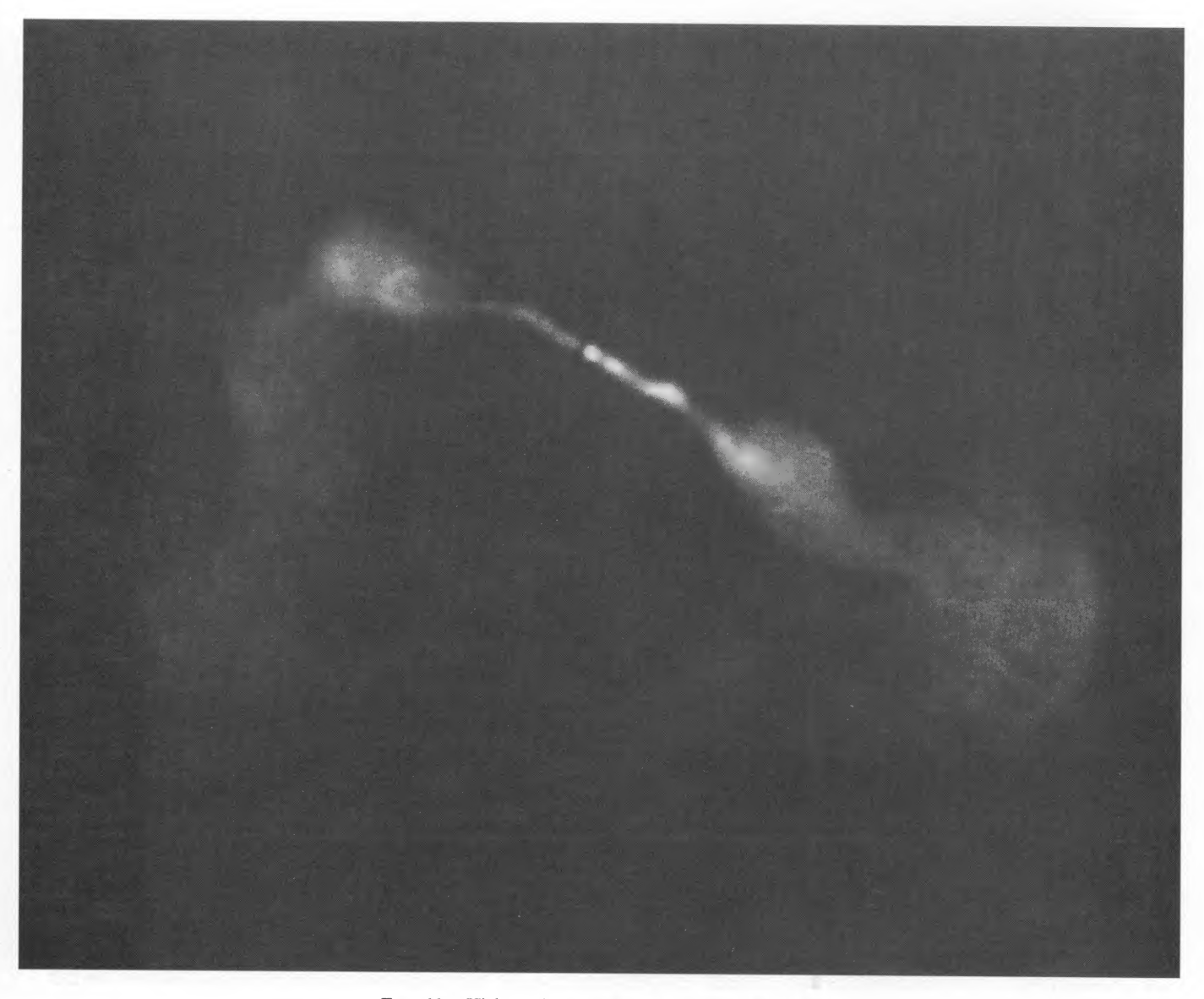


Fig. 66.—High-resolution (1") image of 2236-176 at 20 cm

O'Donoghue, Owen, and Eilek (see 72, 126)

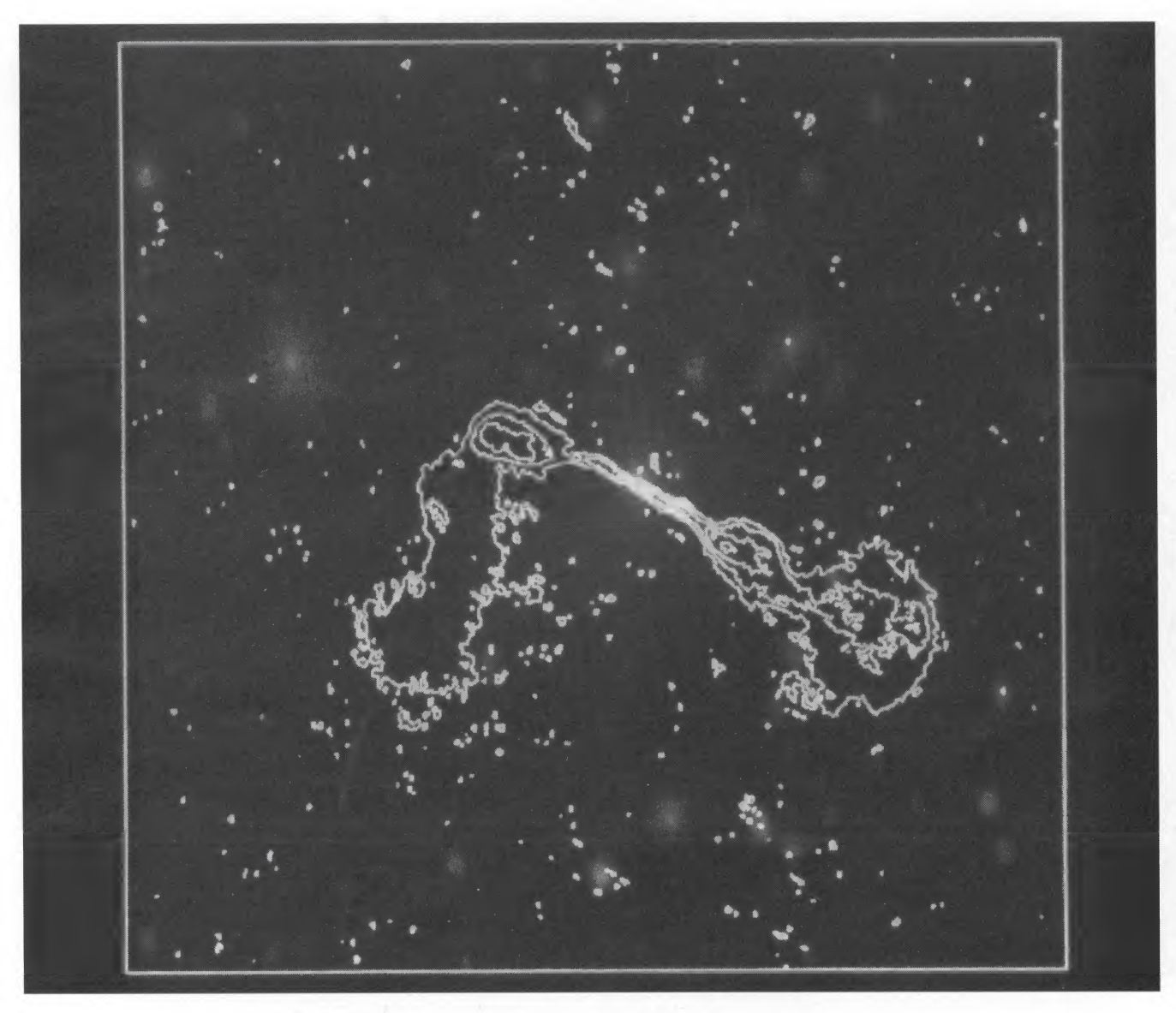


Fig. 67.—20 cm contours of 2236–176 overlaid on the optical galaxy image

O'Donoghue, Owen, and Eilek (see 72, 126)

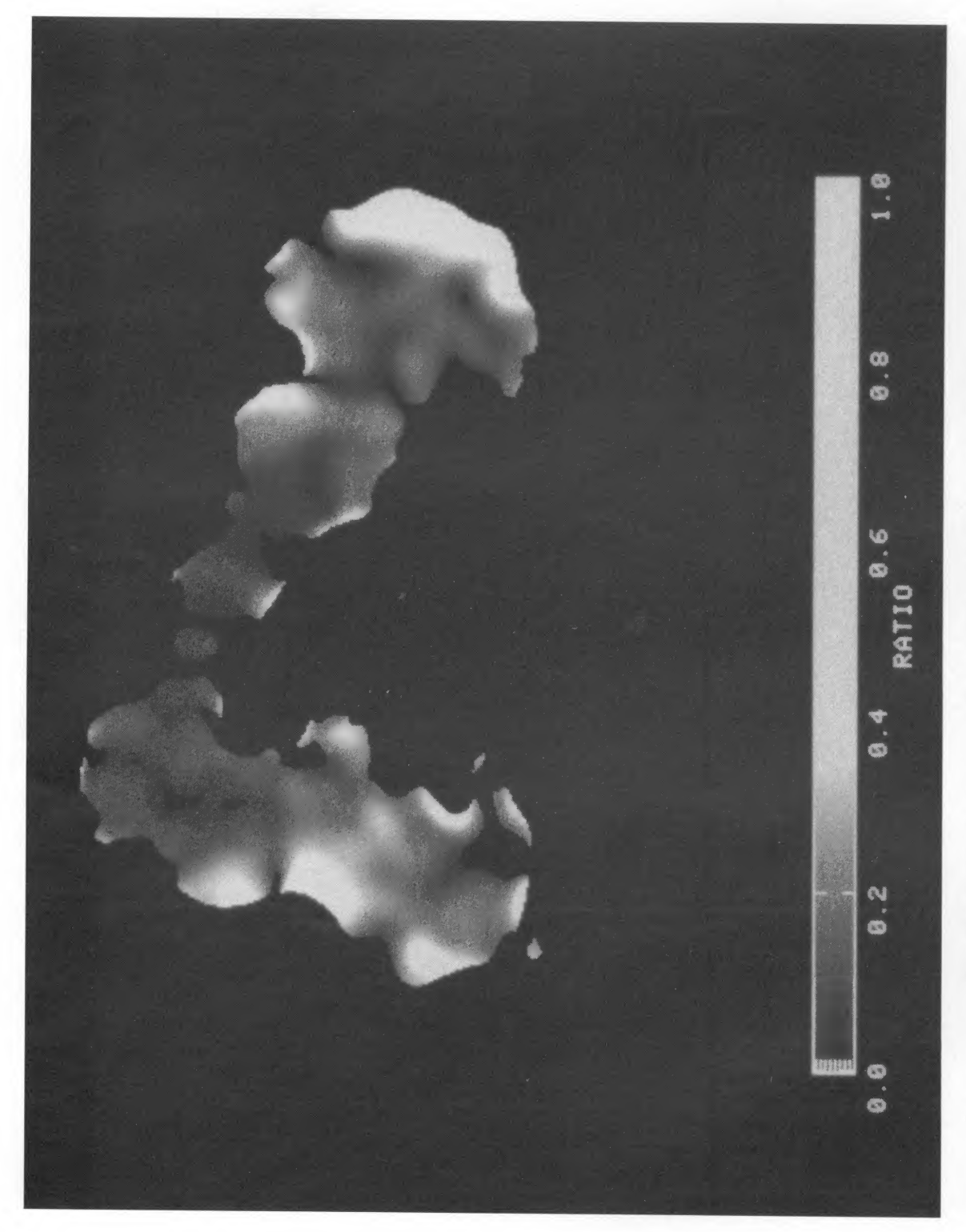


FIG. 68.—Fractional polarization at 20 cm of 2236-176. Note the edge-brightened western lobe

O'DONOGHUE, OWEN, AND ELLEK (see 72, 126)

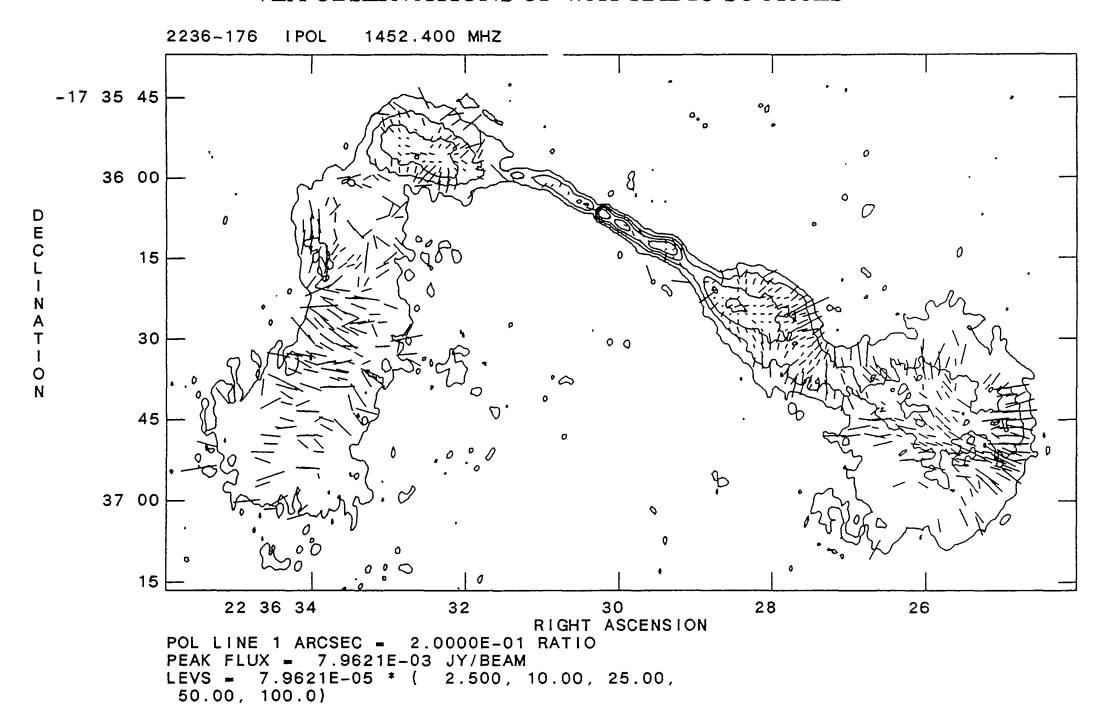


FIG. 69.—Polarization angles for 2236–176, uncorrected for Faraday rotation. Contours are those of the full resolution 20 cm image, and lengths of the vectors are proportional to the fractional polarization at 6 cm.

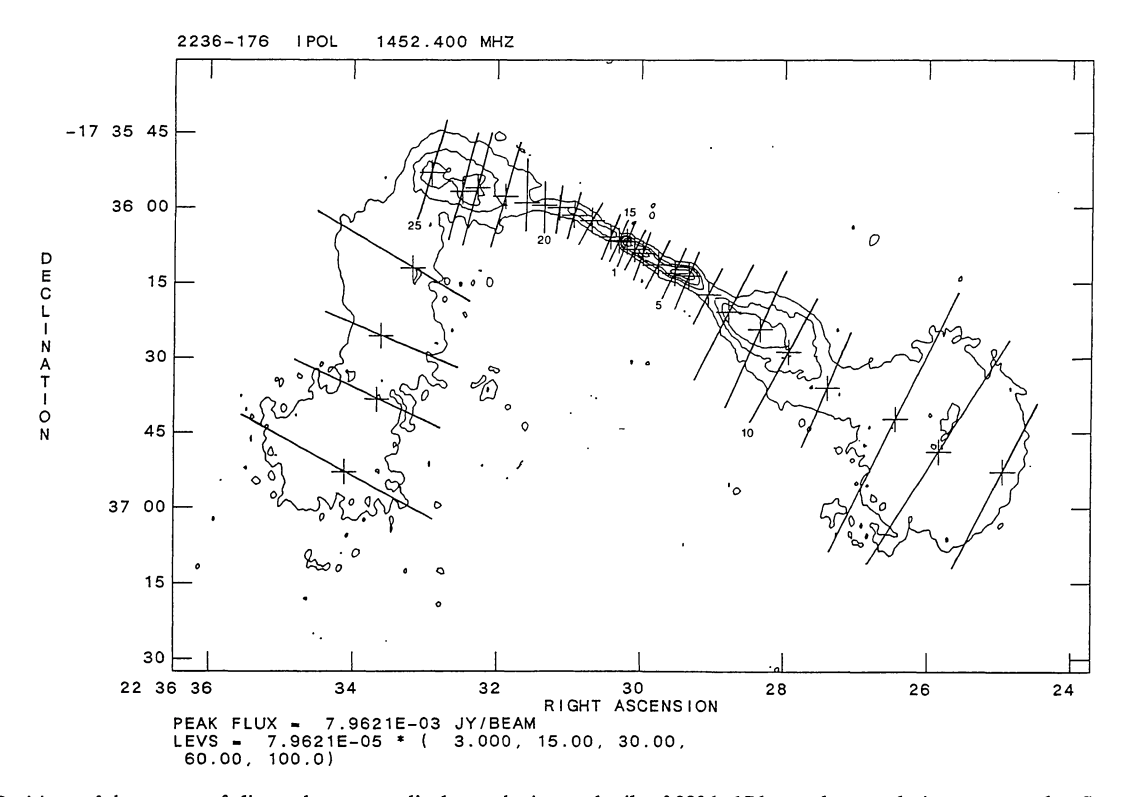
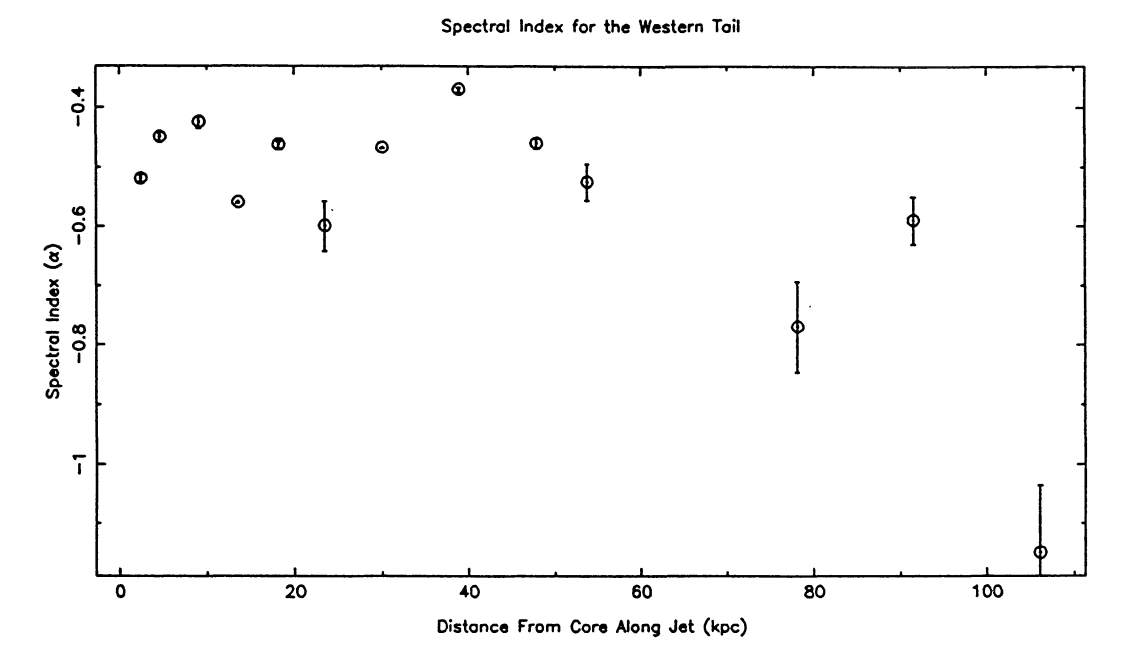


FIG. 70.—Positions of the centers of slices taken perpendicular to the jets and tails of 2236–176, on a low-resolution contour plot. Spectral indices and minimum pressure values for these slices are shown in Figs. 71 and 72.



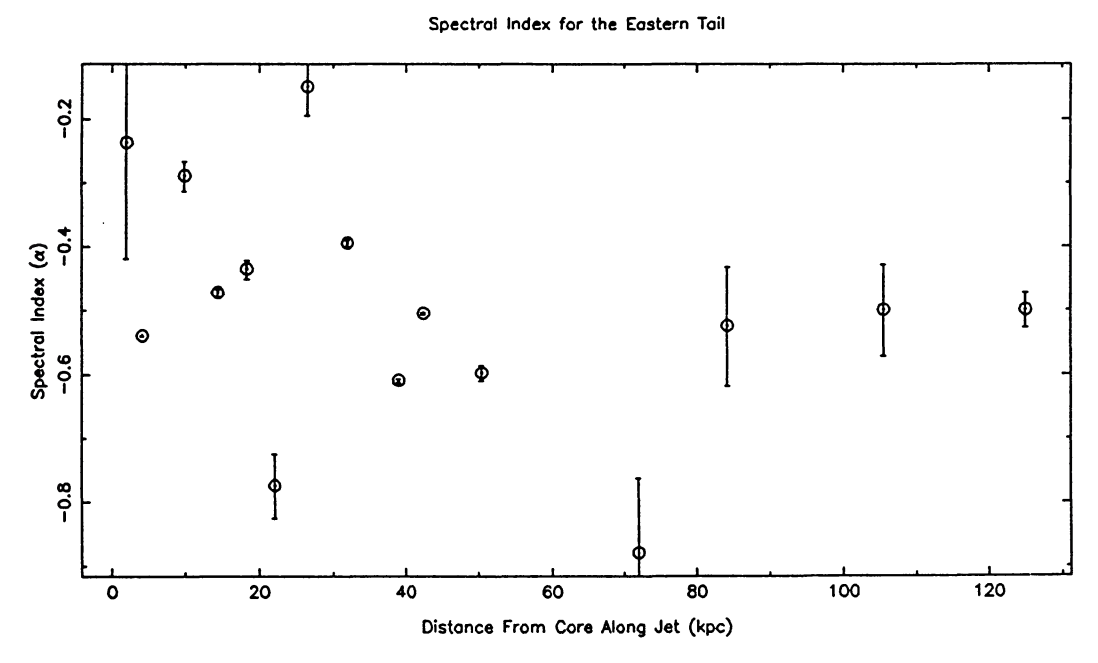


FIG. 71.—Spectral index values between 6 and 20 cm for 2236–176. Values were determined using estimated mean values from slices taken across the total intensity maps, at positions shown in Fig. 70.

ing similar to those in the eastern lobe. These can also be seen in the fractional polarization and have values around 20%-30%. At the end of the western tail the polarized flux increases dramatically, and the fractional polarization increases from the inner lobe values around 20% to $\sim 40\%$. The eastern tail is much less polarized altogether. Only a small patch associated with the first arc is seen above the noise in the polarized intensity, and the fractional polarization is less than 15%.

At 6 cm, the fractional polarization shows less detail in the western tail, but is generally higher in the eastern tail, having values up to 60%. In the polarized intensity, the arcs in the initial broadening of the western tail can be seen, but a much patchier flux density distribution makes them less obvious. They are not apparent in the fractional polarization. The increased polarization at the end of the tail, however, is much more obvious in the fractional polarization where the values soar up to 80%. This high value could indicate a highly

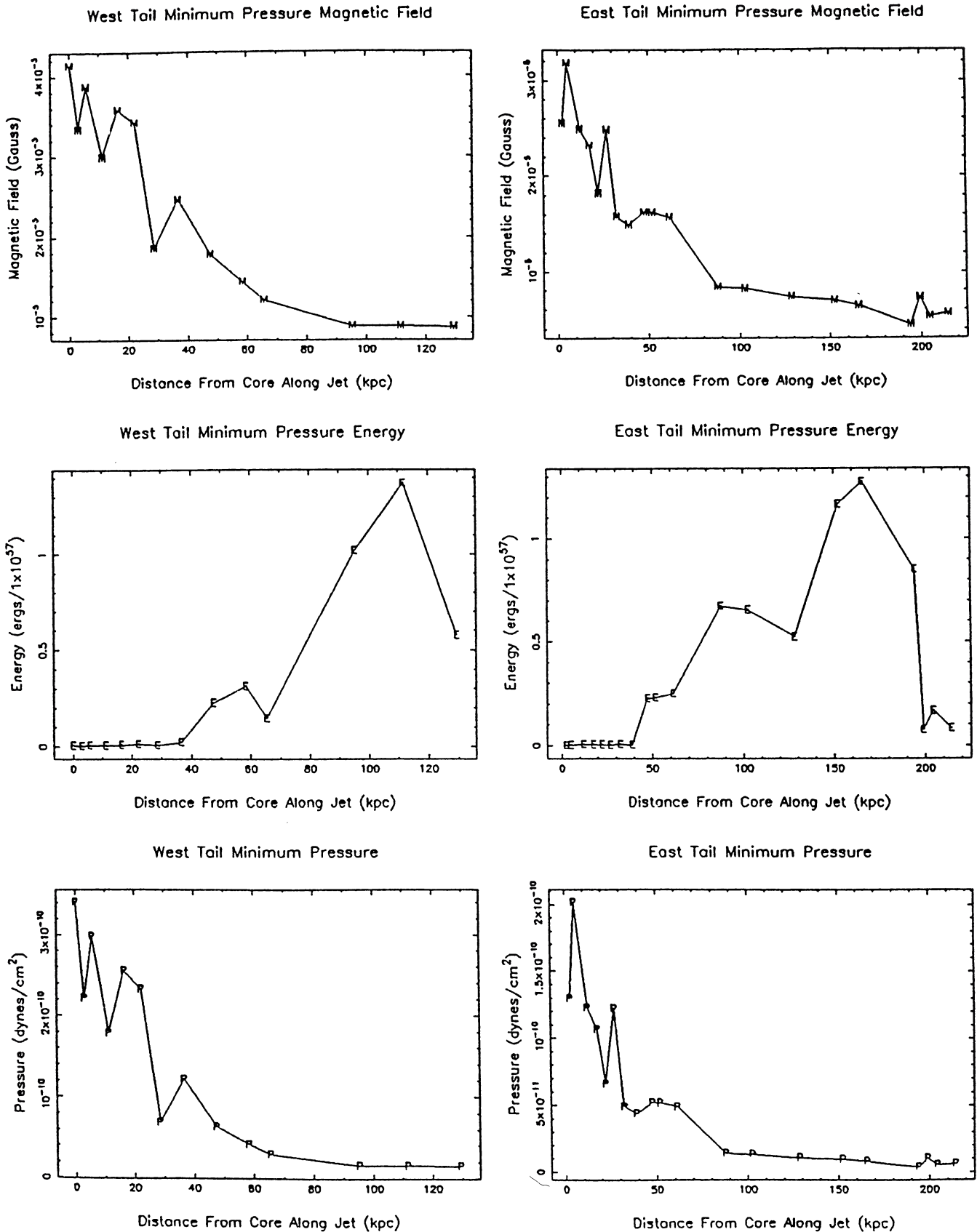


FIG. 72.—Estimates of the magnetic field, total energy (within one slice across the tail), and pressure, derived from minimum pressure arguments, for the north and south tails of 2236–176. Values are given for slice positions shown in Fig. 70. Data are given in Tables 25 and 26.

O'DONOGHUE, OWEN, AND EILEK

TABLE 25 2236-176 Eastern Tail Minimum Pressure

Number	Distance (kpc)	Diameter (kpc)	S per Beam (mJy per beam)	Volume (kpc³)	Luminosity (10 ⁴¹ ergs s ⁻¹)	H _{min} (G)	$\frac{E_{\min}}{(10^{57}\mathrm{ergs})}$	P_{\min} (dyne cm ⁻²)
15	2.0	0.41	0.23	1.0×10^{-1}	5.5×10 ⁻³	2.5×10^{-5}	4.0×10^{-4}	1.3×10^{-10}
16	4.1	0.68	1.43	3.0×10^{-1}	3.4×10^{-2}	3.2×10^{-5}	1.7×10^{-3}	2.0×10^{-10}
17	9.9	1.47	2.77	1.4	6.5×10^{-2}	2.5×10^{-5}	4.9×10^{-3}	1.2×10^{-10}
18	14.4	1.48	2.20	1.4	5.2×10^{-2}	2.3×10^{-5}	4.3×10^{-3}	1.1×10^{-10}
19	18.3	1.74	1.32	1.9	3.1×10^{-2}	1.8×10^{-5}	3.7×10^{-3}	6.6×10^{-11}
20	22.1	0.87	0.96	4.7×10^{-1}	2.3×10^{-2}	2.5×10^{-5}	1.7×10^{-3}	1.2×10^{-10}
21	26.5	2.52	1.66	4.0	3.9×10^{-2}	1.6×10^{-5}	5.8×10^{-3}	4.9×10^{-11}
22	32.0	1.12	0.86	2.5	2.0×10^{-2}	1.5×10^{-5}	3.3×10^{-3}	4.4×10^{-11}
23	39.0	8.54	67.05	$1.5 \times 10^{+2}$	1.6	1.6×10^{-5}	2.2×10^{-1}	5.2×10^{-11}
24	42.5	8.65	68.45	$1.5 \times 10^{+2}$	1.6	1.6×10^{-5}	2.3×10^{-1}	5.2×10^{-11}
25	50.4	9.28	70.76	$1.7 \times 10^{+2}$	1.7	1.6×10^{-5}	2.5×10^{-1}	4.9×10^{-11}
26	72.0	20.63	74.90	$1.6 \times 10^{+3}$	1.8	8.4×10^{-6}	6.7×10^{-1}	1.4×10^{-11}
27		20.90	69.90	$1.7 \times 10^{+3}$	1.7	8.2×10^{-6}	6.5×10^{-1}	1.3×10^{-11}
28	105.5	20.73	47.47	$1.6 \times 10^{+3}$	1.1	7.4×10^{-6}	5.2×10^{-1}	1.1×10^{-11}
29	125.0	32.86	97.50	$4.1 \times 10^{+3}$	2.3	6.9×10^{-6}	1.2	9.6×10^{-12}
35	135.8	26.28	94.56	$5.3 \times 10^{+3}$	2.2	6.4×10^{-6}	1.3	8.2×10^{-12}
36	159.2	31.30	35.86	$7.5 \times 10^{+3}$	8.5×10^{-1}	4.4×10^{-6}	8.5×10^{-1}	3.9×10^{-12}
37		5.64	6.63	$2.4 \times 10^{+2}$	1.6×10^{-1}	7.2×10^{-6}	7.5×10^{-2}	1.0×10^{-11}
38		11.54	9.14	$1.0 \times 10^{+3}$	2.2×10^{-1}	5.3×10^{-6}	1.7×10^{-1}	5.5×10^{-12}
39		7.59	4.96	$4.4 \times 10^{+2}$	1.2×10^{-1}	5.6×10^{-6}	8.1×10^{-2}	6.3×10^{-12}

TABLE 26 2236-176 Western Tail Minimum Pressure

Number	Distance (kpc)	Diameter (kpc)	S per Beam (mJy per beam)	Volume (kpc ³)	Luminosity (10 ⁴¹ ergs s ⁻¹)	H_{\min} (G)	E_{\min} (10 ⁵⁷ ergs)	P_{\min} (dyne cm ⁻²)
2	2.4	0.95	3.28	5.7×10^{-1}	7.8×10^{-2}	3.3×10 ⁻⁵	3.7×10^{-3}	2.2×10^{-10}
3	4.6	1.04	6.57	6.8×10^{-1}	1.6×10^{-1}	3.9×10^{-5}	6.0×10^{-3}	3.0×10^{-10}
4	9.1	1.18	3.46	8.9×10^{-1}	8.2×10^{-2}	3.0×10^{-5}	4.6×10^{-3}	1.8×10^{-10}
5	13.5	1.26	7.30	1.0	1.7×10^{-1}	3.6×10^{-5}	7.5×10^{-3}	2.6×10^{-10}
6	18.2	1.71	11.52	1.8	2.7×10^{-1}	3.4×10^{-5}	1.3×10^{-2}	2.3×10^{-10}
7	23.4	2.26	2.38	3.2	5.6×10^{-2}	1.9×10^{-5}	6.5×10^{-3}	6.9×10^{-11}
8	30.0	3.10	12.11	6.1	2.9×10^{-1}	2.5×10^{-5}	2.2×10^{-2}	1.2×10^{-10}
9	38.9	7.79	77.25	$1.2 \times 10^{+2}$	1.8	1.8×10^{-5}	2.3×10^{-1}	6.3×10^{-11}
10	47.8	11.32	76.86	$2.6 \times 10^{+2}$	1.8	1.4×10^{-5}	3.1×10^{-1}	4.1×10^{-11}
11	53.7	9.18	27.83	$1.7 \times 10^{+2}$	6.6×10^{-1}	1.2×10^{-5}	1.4×10^{-1}	2.9×10^{-11}
12	78.1	24.02	123.00	$2.2 \times 10^{+3}$	2.9	8.9×10^{-6}	1.0	1.6×10^{-11}
13	91.5	27.94	164.92	$3.0 \times 10^{+3}$	3.9	8.9×10^{-6}	1.4	1.6×10^{-11}
14	106.1	18.29	67.81	$1.3 \times 10^{+3}$	1.6	8.7×10^{-6}	5.7×10^{-1}	1.5×10^{-11}

ordered field or some spurious data, but the smoothness argues that the increase in polarization is real. The polarization vectors scaled to the fractional polarization at 6 cm are shown in Figure 69.

iii) Spectral Index and Minimum Pressure Analysis

General trends of steepening can be seen in the spectral indices of both tails, shown in Figure 68. The eastern jet is quite apparent and has values around -0.5 distributed in a slight steepening trend. The western tail shows no trend, but has slightly steeper values than the eastern tail, ranging down to -0.6. There are areas of flat spectral index at both jet/lobe interfaces, but these occur where the total intensity flux density goes down, so it may be spurious.

The eastern lobe steepens from values around -0.5 to -0.7 up to -0.8, but it is quite mixed, reflecting the low surface brightness at 6 cm. The western tail steepens from mixed values in the range of -0.5 to -0.6 in the first lobe to values up to -0.9 in the second. The western edge does not stand out in spectral index.

The positions of the slice centers used in the spectral index and minimum pressure analysis are shown in Figure 70. The spectral index is shown in Figure 71, and the results of the minimum pressure analysis are shown in Figure 72 and Tables 25 and 26.

V. CONCLUSIONS

With the addition of these images, the class of WATs can now be more fully investigated. The distinguishing characteristics of the class are still the rapid decollimation of the jets into lobes and the correlation of the bends with the disruption of the jets. No WAT which bends before decollimation has been observed. The class is also distinguished by reasonably narrow ranges of radio power and the optical magnitudes of the parent galaxies. These sources that are intermediate between classical doubles and NATs in radio luminosity and morphology originate in the most powerful optical sources.

Both classical doubles and NATs emanate from smaller galaxies (Owen and Laing 1989). WATs are found in a unique environment, and the complex interaction of the radio sources and environments motivates further study. Further work examining the flow and bending dynamics of these sources will be reported in a later publication.

The authors wish to thank Jack Burns for helpful suggestions and comments. Also, the staff at the NRAO VLA, particularly Rick Perley, helped greatly with the image processing.

REFERENCES

```
Burns, J. O., Norman, M. L., and Clarke, D. A. 1986, in Proc. NRAO Workshop 16, Radio Continuum Processes in Clusters of Galaxies, ed. C. P. O'Dea and J. M. Uson (Green Bank, WV: NRAO), p. 175. Burns, J. O., Owen, F. N., and Rudnick, L. 1979, A. J., 84, 1683. Colla, G., et al. 1972, Astr. Ap. Suppl., 7, 1. Colla, G., et al. 1973, Astr. Ap. Suppl., 11, 291. Colla, G., et al. Astr. Ap. Suppl., 20, 1. Danese, L., De Zotti, G., and di'Tullio, G. 1980, Astr. Ap., 82, 322. Dickel, J. R., et al. 1971, A.J., 76, 294. Dixon, R. S., and Kraus, J. D. 1968, A.J., 73, 381. Dreher, J. W., and Feigelson, E. D. 1984, Nature, 308, 43. Dressler, A. M. 1976. Ph. D. thesis, University of California at Santa
  Dressler, A. M. 1976, Ph.D. thesis, University of California at Santa
  Eilek, J. A., Burns, J. O., O'Dea, C. P., and Owen, F. N. 1984, Ap. J.,
 Faber, S. M., and Dressler, A. 1977, A.J., 82, 187.
Fantti, C., et al. 1983a, Astr. Ap. Suppl., 51, 179.
Fanti, C., Fanti, R., and Londrillo, P. 1969, Astr. Ap., 2, 477.
Fanti, R., Gioia, I., Lari, C., and Ulrich, M. H. 1978, Astr. Ap. Suppl.,

54, 341.
Fanti, C., 1983b, Astr. Ap. Suppl., 52, 411.
Feretti, L., Giovannini, G., Gregorini, L., Padrielli, L., Roland, J., and Valentijn, E. A. 1985, Astr. Ap., 147, 321.
Fomalont, E. B., and Bridle, A. H. 1978, Ap. J. (Letters), 1978, L9.
Forman, W., Bechtold, J., Blair W., Giacconi, R., van Speybroech, L., and Jones, C. 1981, Ap. J. (Letters), 234, L133.
Ghigo, F. D., and Owen, F. N. 1973, A.J., 78, 848.
Giovannini, G., Feretti, L., and Gregorini, L. 1987, Astr. Ap. Suppl., 69, 171

        171
Greuff, G., and Vigotti, M. 1972, Astr. Ap. Suppl., 6, 1.

Harris, D. E., Kapahi, V. K., and Ekers, R. D. 1980, Astr. Ap. Suppl., 39,
Henry, J. P., Henriksen, M. J., Charles, P. A., and Thornstensen, J. R. 1981, Ap. J. (Letters), 243, L137.
Hines, D. C., Owen, F. N., and Eilek, J. A. 1990, Ap. J., in press.
Hoessel, J. G., and Schneider, D. P. 1985, A.J., 190, 1684. Hunstead, R. W. 1972, M.N.R.A.S., 157, 367. Jaffe, W. J., and Perola, G. C. 1973, Astr. Ap., 26, 423. Leahy, P. 1984, M.N.R.A.S., 208, 323.
Leir, A. A., and van den Bergh, S. 1977, Ap. J. Suppl., 34, 381. McHardy, I. M. 1974, M.N. R.A.S., 169, 527.

______. 1978a, M.N. R.A.S., 184, 783.
______. 1978b, M.N. R.A.S., 185, 927.
```

```
Morganti, R., Fanti, R., Gioia, I. M., Harris, D. E., Parma, P., and de Ruiter, H. 1988, Astr. Ap., 189, 11.

Norman, M. L., Burns, J. O., and Sulkanen, M. 1988, Nature, 335, 146.

O'Dea, C. P., and Owen, F. N. 1985, A.J., 90, 954.

______. 1986, Ap. J., 301, 841.

O'Donoghue, A. A. 1989, Ph.D. thesis, New Mexico Institute of Mining
o'Donoghue, A. A., Eilek, J. A., and Owen, F. N. 1990, in preparation.

Owen, F. N. 1974a, A.J., 79, 427.

_______. 1975a, Ap. J., 195, 593.

______. 1975b, A.J., 80, 263.
Owen, F. N. 1990, in preparation.
Owen, F. N., Hardee, P. E., and Cornwell, T. J. 1989, Ap. J., 340, 648.
Owen, F. N., and Laing, R. A. 1989, M.N.R.A.S., 238, 357.
Owen, F. N., O'Dea, C. P., Inoue, M., and Eilek, J. A. 1985, Ap. J.
      (Letters), 294, L85
Owen, F. N., and Rudnick, L. 1976, Ap. J. (Letters), 205, L1. Owen, F. N., Rudnick, L., and Peterson, B. M. 1977, A.J., 82, 677. Owen, F. N., and White, R. A. 1990, in preparation.

Owen, F. N., White, R. A., Hilldrup, K. C., and Hanisch, R. J. 1982,
       A. J., 87, 1083.
Owen, F. N., White, R. A., and Thronson, H. A. 1988, A.J., 95, 1. Pacholczyk, A. G. 1970, Radio Astrophysics (San Francisco: Freeman). Parma, P., Fanti, C., Fanti, R., Morganti, R., and de Ruiter, H. R. 1987, Astr. Ap., 181, 244.
 Patnaik, A. R., Banhatti, D. C., and Subranhmanya, C. R. 1984, M.N.R.A.S., 211, 775.
 Patnaik, A. R., Malkan, M. A., and Salter, C. J. 1986, M.N.R.A.S., 220,
 Perley, R. A., Bridle, A. H., and Willis, A. G. 1984, Ap. J. Suppl., 54,
291.
Pilkington, J. D. H., and Scott, P. F. 1965, Mem. R.A.S., 69, 183.
Riley, J. M. 1975, M.N.R.A.S., 170, 53.
Robertson, J. G. 1984, Astr. Ap., 138, 41.
Roland, J., Veron, J., Pauliny-Toth, I. I. K., Preuss, E., and Witzel, A. 1975, Astr. Ap., 50, 165.
Rudnick, L. 1984, in Proc. NRAO Workshop 9, Physics of Energy
 Transport in Extragalactic Radio Sources, ed. A. H. Bridle and J. A. Eilek (Green Bank, WV: NRAO), p. 35.
Rudnick, L., and Owen, F. N. 1977, A.J., 82, 1.
 Shimmins, A. J., Manchester, R. N., and Harris, B. J. 1969, Australian J.
Phys., Ap. Suppl., 8, 1.
Simon, A. J. B. 1978, M.N.R.A.S., 184, 537.
Slingo, A. 1974, M.N.R.A.S., 168, 307.
Tabara, H., and Inoue, M. 1980, Astr. Ap. Suppl., 39, 379.
```

JEAN A. EILEK: Physics Department, New Mexico Tech, Socorro, NM 87801

AILEEN A. O'DONOGHUE: Physics Department, St. Lawrence University, Canton, NY 13617

FRAZER N. OWEN: NRAO, P.O. Box O, Socorro, NM 87801